MCGILL UNIVERSITY

Entanglement and disorder in gapped and gapless topological states

Jan Borchmann

Department of Physics

August 2016

McGill University, Montreal, Quebec

A thesis submitted to McGill University in partial fulfillment of the requirements of the degree of Doctor of Philosophy

Abstract

In this thesis we investigate gapped and gapless topological states, their connection to entanglement and their response to perturbations such as disorder and external magnetic fields. We start out by analyzing numerically and analytically the entanglement entropy of a spin-orbit coupled topological superconductor and its signature of the topological phase transition. We find that the entanglement entropy obeys the area law and that it displays a second order phase transition at the phase transition point. Subsequently, we investigate the effect of a random disorder potential on the topology of the system by using a real space Chern number and comparing it with the results obtained by looking at the disorder averaged entanglement entropy.

In the last part, we investigate the Landau level spectrum of a gapless Weyl semimetal slab when exposed to an external magnetic field. Due to the Fermi arcs in the surface Brillouin zone it is possible to form magnetic orbits involving states on both surfaces with characteristic thickness dependence. Using an effective surface theory for a Weyl semimetal, we are able to calculate the surface density of states and determine the phase offset.

Résumé

Dans cette thèse, nous étudions les états topologiques gaps et gapless, leur connexion à l'enchevêtrement et leur réponse aux perturbations telles que le désordre et les champs magnétiques externes. Nous commençons par analyser numériquement et analytiquement l'entropie d'enchevêtrement d'un spin-orbite couplé supraconductrice topologique et sa signature de la transition de phase topologique. Nous constatons que l'entropie d'enchevêtrement obéit à la loi de la zone et qu'il affiche une transition du deuxième ordre au point de transition de phase. Par la suite, nous étudions l'effet d'un potentiel de désordre aléatoire sur la topologie du système en utilisant un numéro de Chern de espace réel et en le comparant avec les résultats obtenus en regardant l'entropie d'enchevêtrement.

Dans la dernière partie, nous étudions le spectre de niveau de Landau d'un gapless Weyl semi-métal lorsqu'il est exposé à un champ magnétique externe. En raison des arcs de Fermi dans la zone de Brillouin de la surface, il est possible de former des orbites magnétiques faisant intervenir des états sur les deux surfaces ayant une dépendance à l'épaisseur caractéristique. L'utilisation d'une théorie efficace de la surface pour un métalloïde Weyl, nous sommes en mesure de calculer la densité de surface d'états et de déterminer le décalage de phase.

Acknowledgments

First and foremost I would like to express my gratitude to my family, specifically my parents and my girlfriend Ana, on whose support I was able to rely throughout the last three years and who gave me the motivation and energy to finish such a longterm project.

Second, I want to thank my supervisor, Tami Pereg-Barnea, without whom the whole PhD would not have been possible. She provided the guidance for me to successfully start in a new field and immediately be productive as well as the support and input for new and exciting projects that culminated in this thesis.

Third, I would like to thank all the members of office 228 for making it such a great place to work in, despite the lack of sunlight and the ironically freezing temperatures in the summer months. Specifically, but not exhaustingly, I would like to thank Aaron who helped me a lot during the beginning by being always available for questions and discussions, Rosa who gave the office a beautiful prehistoric atmosphere, Grace for always volunteering for helping to solve hard integrals and creating seasonal German pigs, Yony for the endless discussions on Chinese online retailers, great deals on the internet and credit cards and, last but not least, Kunal for always providing the last news in hockey and knowing the right pizza places to go to.

Contributions of authors

This dissertation is formatted as a manuscript based thesis with all the papers (Chapters 2, 3, 4, and 5) having been published, submitted for publication or planned to be submitted during my candidature. I am the principal author of each chapter and considered as the sole author of the thesis and fully responsible for everything contained in it. The contributions of the other authors to each of the four manuscripts are listed below.

Entanglement Spectrum as a Probe for the Topology of a Spin-Orbit Coupled Superconductor

Jan Borchmann:

Performed the main analytical and numerical analyses of the problem. Co-compiled and interpreted the results of these calculations and shared editing responsibilities during the preparation of the manuscript.

Aaron Farrell:

Performed additional analytical and numerical analyses of the problem. Co-compiled and interpreted the results of these calculations and shared editing responsibilities during the preparation of the manuscript.

Shunji Matsuura:

Provided critical evaluation, advice and shared the responsibilities of editing the manuscript.

T. Pereg-Barnea:

Originally proposed the idea for the work and supervised its development. Provided critical evaluation, advice, and interpretation of results as the work progressed and shared the responsibilities of editing the manuscript.

Analytic Expression for the Entanglement Entropy of a 2D Topological Superconductor

Jan Borchmann:

Co-proposed the idea for the work and performed the analytical and numerical analyses of the problem. Compiled and interpreted the results of these calculations and shared editing responsibilities during the preparation of the manuscript.

T. Pereg-Barnea:

Co-proposed the idea for the work and supervised its development. Provided critical evaluation, advice, and interpretation of results as the work progressed and shared in the the responsibilities of editing the manuscript.

Anderson Topological Superconductor

Jan Borchmann:

Performed the main analytical and numerical analyses of the problem. Compiled and interpreted the results of these calculations, and shared in the editing responsibilities during the preparation of the manuscript.

Aaron Farrell:

Performed additional analytical and numerical analyses of the problem. Shared in the editing responsibilities during the preparation of the manuscript.

T. Pereg-Barnea:

Originally proposed the idea for the work and supervised its development. Provided critical evaluation, advice, and interpretation of results as the work progressed and shared in the the responsibilities of editing the manuscript.

Quantum oscillations in Weyl semimetals via an effective surface theory

Jan Borchmann:

Performed the analytical and numerical analyses of the problem. Compiled and interpreted the results of these calculations and shared in the editing responsibilities during the preparation of the manuscript.

T. Pereg-Barnea:

Originally proposed the idea for the work and supervised its development. Provided critical evaluation, advice, and interpretation of results as the work progressed and shared in the the responsibilities of editing the manuscript.

Contents

List of Figures

1

Introduction

1.1 Symmetry protected topological states

Recently the field of topological states of matter[1–9] has attracted a vast amount of interest and research activity by physicists. Up until its discovery the general principle of distinguishing different phases was connected to spontaneous symmetry breaking and local order parameters. When a system would change from one phase to another, generally, it would break one or more of its symmetries. Thus, the discovery of topological states of matter represented a paradigm shift due to the fact that the ground states of different phases would not be distinguishable by the absence or presence of any symmetries and connected order parameters. This necessitated that concepts from topology were introduced in order to describe the new states of matter.

Mathematically, two topological spaces are equivalent if there exists a homeomorphism between them, meaning a continuous mapping with a continuous inverse that preserves all topological properties of the space. These maps can be imagined to be deformations of the space such as stretching or bending. Thus, a circle and a square are homeomorphic as they can be deformed into each other, whereas a circle and a ring

are not. The number of holes is usually called the genus and is one of the most simple topological invariants.

How does this translate to physical systems and quantum states? In order to understand the connection we will consider a local quantum system that is described by a family of Hamiltonians $H(s)$, where s is a continuous parameter and $|\phi(s)\rangle$ is its ground state with an excitation gap to its excited states. We say two states $|\psi(0)\rangle$ and $|\psi(1)\rangle$ are in the same phase if we can vary the parameter s smoothly from 0 to 1 without closing the gap. This is the equivalent of having a homeomorphism between two topological spaces. Conversely, if there is a phase transition somewhere in the interval $[0, 1]$ there will be a gap closure and it is not possible to smoothly deform $|\psi(0)\rangle$ into $|\psi(1)\rangle$. Thus, it defines an equivalence class of ground states that can be smoothly transformed into each other. In physical terms this is the universality class that defines the phase in which the two connected states are in.

So far, we have disregarded any possible symmetries of the system in this discussion, as we have found that systems can undergo a quantum phase transition without changing its symmetries, leading to conceptually new quantum states. Physical realizations of this are quantum spin liquids[10, 11] and fractional quantum hall states[12–14]. Moreover, there are even finer distinctions of the universality classes when we do take into account symmetries of the system. If we restrict the deformations to only those that respect a certain symmetry, we can realize so-called symmetry protected topological states. In the stricter sense developed above these states are trivial as they can be deformed to the trivial state by using deformations that violate the specific symmetry of the system. However, if the deformations preserve the symmetry, it is not possible to reach a trivial state without closing the gap of the system. Thus, these states are distinct from trivial states and exhibit characteristic properties such as gapless edge states and unconventional electromagnetic responses.

Generally, there is no order parameter, given by the expectation value of a local operator, connected to a topological phase transition that would be comparable to the situation of the Landau symmetry breaking phases. Consequently, one has to rely on other quantities in order to determine if one is in a topological phase or not. Generally, these are called topological invariants and most commonly are either integer or binary indicators of the topology of a system. This raises the question of how one can characterize a system and determine which topological phases are possible. There has been a lot of work[15–18] to classify the different possible symmetry protected states that can be realized in condensed matter systems in order to answer this exact question. An important topological invariant in systems with broken time reversal symmetry that will be used throughout this work is the Chern number that is obtained by integrating the Berry curvature over the Brillouin zone. This is done by constructing a so-called fibre bundle $\mathcal{L}$, where the Brillouin zone B is the base space and the filled Bloch states are the fibre F. Locally this looks like the product space $B \times F$, whereas globally the fibre bundle can have a different topological structure. The Berry connection $\mathbf{A}(k) = \sum_n i\langle\psi_n(k)|\nabla|\psi_n(k)\rangle$ then enables one to describe how a Bloch state changes when we move from one point k_0 to another point k_1 in the Brillouin zone. Further, one can calculate the Chern number by integrating the Berry curvature $\Omega = \nabla \times \mathbf{A}$.

The systematic approach to classify symmetry protected topological states is based on the possible generic symmetries of the Hamiltonian H, time reversal symmetry $\mathcal{T}$, particle-hole symmetry $\mathcal{P}$ as well as chiral symmetry $\mathcal{C}$. The latter is sometimes also called sublattice symmetry (and denoted with a letter S) in condensed matter physics due to the fact that a natural realization is often the fact that a system has two sublattices and the Hamiltonian solely couples sites in different sublattices. The restriction to these three symmetries is due to the fact that, in general, unitary symmetries enable the Hamiltonian to be brought into a block-diagonal form with a number of irreducible blocks that can

Cartan	$\mathcal{T}$	$\mathcal{P}$	$\mathcal{C}$	Dimension d				
				0	1	2	3	4
A				$\mathbb{Z}$	0	$\mathbb{Z}$	0	$\mathbb{Z}$
AIII			✓	0	$\mathbb{Z}$	0	$\mathbb{Z}$	0
AI	1			$\mathbb{Z}$	0	0	0	$2\mathbb{Z}$
BDI	1	1	✓	$\mathbb{Z}_2$	$\mathbb{Z}$	0	0	0
D		1		$\mathbb{Z}_2$	$\mathbb{Z}_2$	$\mathbb{Z}$	0	0
DIII	-1	1	✓	0	$\mathbb{Z}_2$	$\mathbb{Z}_2$	$\mathbb{Z}$	0
AII	-1			$2\mathbb{Z}$	0	$\mathbb{Z}_2$	$\mathbb{Z}_2$	$\mathbb{Z}$
CII	-1	-1	✓	0	$2\mathbb{Z}$	0	$\mathbb{Z}_2$	$\mathbb{Z}_2$
C		-1		0	0	$2\mathbb{Z}$	0	$\mathbb{Z}_2$
CI	1	-1	✓	0	0	0	$2\mathbb{Z}$	0

Table 1.1: Classification of symmetry protected topological states by spatial dimension d and symmetry class, denoted by its Cartan label. Here, $\mathbb{Z}$ ($\mathbb{Z}_2$) means that the possible phases are described by an integer (binary) invariant. The existing symmetries of the system are indicated by checkmarks ($\mathcal{C}$) or the square of the symmetry operator, i.e., $\mathcal{T}^2 = \pm 1$ and $\mathcal{P}^2 = \pm 1$.

subsequently be analyzed independently. However, the aforementioned symmetries act differently by constraining the irreducible parts of the Hamiltonian. Time reversal as well as particle-hole symmetry are anti-unitary and thus involve complex conjugation. Chiral symmetry is unitary but anti-commutes with the Hamiltonian, which can easily be seen by using the fact that the presence of both anti-unitary symmetries implies chiral symmetry, $\mathcal{C} = \mathcal{P} \cdot \mathcal{T}$. Due to their anti-unitarity, both $\mathcal{P}$ and $\mathcal{T}$ can either square to $+1$ or -1. Counting all possible combinations, there are 10 distinct cases, all distinguished by their respective symmetry properties. Depending on the dimension d of the system, one can derive the possible phases and their topological invariants through very general arguments. The result is summarized in table 1.1[19]. This classification is in no way exhaustive and it is possible to further extend it and take into account, for example, crystal symmetries and thus realize so-called crystalline topological insulators[20–23].

Some of the most important consequences of topologically non-trivial states are the properties of the boundary. When a topological system encounters another system at its edge (in real applications this will most likely be the vacuum or another trivial

system), the topology changes abruptly from a topologically non-trivial to a trivial state. Due to this fact, the energy gap needs to close at the boundary, leading to gapless excitations on the boundary of the topological system. This fact is called the edge boundary correspondence. Caused by their topological nature, these zero-energy states are robust against small deformations as long as the topological properties of the system are not changed. As a consequence, weak disorder or applied fields do not destroy the topological nature as long as the gap is not closed due to the perturbations.

A class of symmetry protected topological states that has attracted a lot of attention and research activity in recent years are topological superconductors. In these systems the edge states, caused by the topological nature of the phase, are so-called Majorana modes. Historically, Majorana fermions were discovered[24] as the real solutions to the Dirac equation, the relativistic equation describing electrons while taking into account their spin-$\frac{1}{2}$ structure. These particles are their own anti-particles and thus behave fundamentally different from electrons. Throughout the twentieth century, particle physicists have searched for a realization of Majorana fermions as a fundamental particle, but so far none have been found. A popular theory to explain the neutrino oscillation[25–27] assumes that both left- and right-handed neutrinos are Majorana fermions and would explain the small neutrino masses through the seesaw mechanism. However, to date no experimental evidence that would support this theory has been found. On the other hand, topological superconductors present the first opportunity to investigate Majorana physics directly in experiment.

However, it is important to distinguish between the condensed-matter realization[28] of a Majorana mode γ and the particle proposed as the solution to the neutrino problem. Whereas the latter would be a fundamental particle obeying Fermi statistics, the Majorana modes in topological superconductors are emergent excitations and are so-called non-abelian anyons. These types of (quasi-) particles have non-trivial exchange statistics and,

as the name suggests, permutations of two or more Majorana modes are non-commutative. Due to this fact, Majorana modes are promising candidates for realizing topologically protected qubits as a step towards quantum computing[29].

At first glance, superconductors present a natural choice for realizing Majorana modes as the excitations are composed of both electrons and holes and one could easily construct self-adjoint operators that can act on the ground state. Unfortunately, due to the singlet spin structure of the the Bogoliubov operators in BCS superconductors with s-wave pairing, this easy construction does not work. In order to resolve this, one can look at systems with unconventional triplet pairing, so called $p_x + ip_y$-pairing. However, these are rare and so far have not conclusively been observed in experiment. The layered superconductor Sr_2RuO_4 is believed to possess this type of triplet pairing but the available indirect evidence remains inconclusive[30–33].

The emergence of Majorana modes can be seen when considering a one-dimensional toy model, often called the Kitaev model[28]. It is a spinless lattice model with p-wave order parameter Δ, hopping amplitude t and chemical potential μ,

$$H_{KM} = -\sum_{i=1}^{N-1} \left(t c_i^\dagger c_{i+1} + t c_{i+1}^\dagger c_i + \Delta c_i^\dagger c_{i+1}^\dagger + \Delta^* c_{i+1} c_i \right) - \mu \sum_{i=1}^{N} c_i^\dagger c_i. \tag{1.1.1}$$

Assuming periodic boundary conditions it is straightforward by using the Fourier transformation $c_j = \frac{1}{\sqrt{N}} \sum_k e^{-ikx_j} c_k$ to write down the Bogoliubov-de-Gennes Hamiltonian,

$$H_{BGD} = \begin{pmatrix} \epsilon_k & 0 & 0 & \Delta \sin k \\ 0 & \epsilon_{-k} & -\Delta \sin k & 0 \\ 0 & \Delta^* \sin k & -\epsilon_k & 0 \\ \Delta^* \sin k & 0 & 0 & -\epsilon_{-k} \end{pmatrix}. \tag{1.1.2}$$

By diagonalizing this matrix, we can derive the eigenvalues of the Hamiltonian as

$$E_k = \sqrt{(-2t\cos k - \mu)^2 + |\Delta|^2 \sin^2 k}. \tag{1.1.3}$$

From this we can immediately see that the quasiparticle spectrum has a finite gap except when $|\mu| = 2t$. At these points the quasiparticle gap closes and the system can undergo a topological phase transition. There exists a simple way to calculate the topological invariant connected to the phase transition at the gap closure. This is the so-called ground state parity $\mathcal{Q}$[10]. It is defined as

$$\mathcal{Q} = \frac{\text{Pf}(H_{BDG}\, i\tau_x)}{\sqrt{\det(H_{BDG}\, i\tau_x)}}, \tag{1.1.4}$$

where τ_x acts on the particle-hole space and Pf is the Pfaffian, defined through

$$\text{Pf}(A) = \frac{1}{2^n n!} \sum_{\sigma \in S_{2n}} \text{sgn}(\sigma) \prod_{i=1}^{n} a_{\sigma(2i-1),\sigma(2i)}. \tag{1.1.5}$$

Here, S_{2n} is the symmetric group of dimension $(2n)!$. The Pfaffian is generally defined for any anti-symmetric matrix A and has the property $\text{Pf}^2(A) = \det(A)$. Due to this fact the Pfaffian possesses an additional sign degree of freedom that is not present in the determinant. This is exactly what is extracted when calculating $\mathcal{Q}$. Accordingly, the parity $\mathcal{Q}$ can only change its value when the Pfaffian changes its sign and vanishes. From the above stated connection one can see that this in turn implies that the determinant has to vanish as well. Moreover, it implies that the Hamiltonian has a zero-energy eigenvalue, thus closing the energy gap. Hence, deformations of the Hamiltonian that leave the excitation gap unchanged cannot change the parity $\mathcal{Q}$, making it a topological invariant.

Applying (1.1.4) to the Kitaev model, we find

$$\mathcal{Q} = \text{sgn}(\epsilon_0 \epsilon_\pi) = \text{sgn}(\mu^2 - 4t^2), \tag{1.1.6}$$

which shows that $\mathcal{Q} = 1$ for the strong-pairing phase $|\mu| > 2t$ and $\mathcal{Q} = -1$ for the weak-pairing phase $|\mu| < 2t$. Thus, we see that for a given pairing Δ the model exhibits two distinct phases, a trivial one which is topologically equivalent to the vacuum with even parity $\mathcal{Q} = 1$ and a topological phase with odd parity $\mathcal{Q} = -1$.

In order to understand the appearance of Majorana modes, we will now consider a finite Kitaev chain with an even number of lattice sites N and for simplicity choose the superconducting phase ϕ to be zero. As discussed above, when introducing a boundary or a defect into a topological system, we would expect to have gapless edge modes appear there. We now write the Hamiltonian (1.1.1) in terms of Majorana modes,

$$\begin{aligned} c_i &= \frac{1}{2}\left(\gamma_{i,1} + i\gamma_{i,2}\right), \\ c_i^\dagger &= \frac{1}{2}\left(\gamma_{i,1} - i\gamma_{i,2}\right), \end{aligned} \tag{1.1.7}$$

which at this point is merely a mathematical transformation. We have split the fermionic operator from each site into its real and imaginary part. The easiest point in parameter space to analyze the Hamiltonian is $\mu = 0$ and $\Delta = t$. With this, the Hamiltonian reads,

$$H_{KM} = -it \sum_{i=1}^{N-1} \gamma_{i,2}\gamma_{i+1,1}. \tag{1.1.8}$$

However, if we now combine Majorana modes from neighbouring sites into new fermionic operators,

$$\tilde{c}_i = \frac{1}{2}\left(\gamma_{i+1,1} + i\gamma_{i,2}\right), \tag{1.1.9}$$

the Hamiltonian for the Kitaev chain is,

$$H_{KM} = 2t \sum_{i=1}^{N-1} \tilde{c}_i^\dagger \tilde{c}_i. \tag{1.1.10}$$

In this Hamiltonian, we see that the Nth fermionic operator $\tilde{c}_N = \frac{1}{2}(\gamma_{N,2} + i\gamma_{1,1})$ does not appear anymore. This highly non-local state thus has zero energy and the ground state is consequently degenerate. This also explains why the topological invariant $\mathcal{Q}$ is called the ground state parity. The ground-state in the topological phase can either have an even number of electrons which are paired up as Cooper pairs or an odd number of electrons where the zero-energy state is occupied. Further, even though we have shown the emergence of localized Majorana modes on the boundary of the chain only for the special values $\mu = 0$ and $\Delta = t$, the calculation of the topological invariant has shown that we would expect the argument to hold even for general values as long as $|\mu| < 2t$. Additionally, in two dimensions, one can show that there appear Majorana modes in vortices in the superconducting pairing amplitude[34, 35].

The Kitaev model is very simple, and due to the lack of spin, unrealistic. Nonetheless, there have been multiple proposals[36] in order to realize topological superconductivity with more readily available ingredients that effectively realize the Kitaev model or a two dimensional generalization of it. One of the first proposals by Fu and Kane[37] introduced the idea to use heterostructures consisting of a 3D topological insulator in contact with an ordinary s-wave superconductor in order to realize a $p_x + ip_y$-superconductor at the interface. This sparked a flurry of further proposals such as a trilayer device where a semiconducting quantum well would be brought into contact with an s-wave superconductor and a ferromagnetic insulator[38] or a bilayer device consisting of a quantum well with both Rashba and Dresselhaus spin-orbit coupling and an s-wave superconductor with an applied magnetic field[39]. In addition, multiple proposals have

been brought forward that set out to realize spinless p-wave pairing in one-dimensional systems[40, 41]. Despite the very different nature of these proposals, the main ingredients stay the same in both one as well as two dimensions. One has to break the degeneracy of the electrons caused by their spin in order for the system to be effectively spinless. Further, one has to give the electrons a non-trivial spin structure that allows the system to enter a topological phase. In the last couple of years there have been multiple experimental groups that have reported evidence for Majorana modes in various different hybrid systems[42, 43] observing zero bias peaks in conductivity measurements. However, a direct proof of Majorana modes still remains elusive as not all alternative causes for the zero bias peak have been ruled out[44–46].

1.2 Entanglement entropy

It has been realized that there exists a deep connection between topological states of matter and entanglement[47–51]. This connection is intriguing and lends itself to further investigation. In fact, this is one of the objectives of this work. In order to achieve this task, we need to introduce some of the concepts that are used to analyze entanglement in condensed matter systems.

Entanglement has a rich and long history[52–54] and is a purely quantum phenomenon without a classical analogue. But given a quantum ground state $|\psi\rangle$, how can we extract information about its entanglement? This is generally done by dividing the system into two or more subsystems with respect to some degree of freedom and then analyzing the entanglement of each subsystem with the complement. For example, one can divide the system into two parts of different shape in real space, in momentum space or even with respect to internal degrees of freedom such as spin.

There is a general way for how one can explicitly show the correlation between

two subsystems in $|\psi\rangle$ and it is called the Schmidt decomposition[55]. When dividing the system into subsystems, one divides the Hilbert space into two separate parts with orthonormal bases $|\psi_m^1\rangle$ and $|\psi_n^2\rangle$ and can write the ground state as

$$|\psi\rangle = \sum_{m,n} A_{mn} |\psi_m^1\rangle |\psi_n^2\rangle. \tag{1.2.1}$$

Generally, the dimensions of the two subsystems are not equal and thus A_{mn} will not be a square matrix. However one can diagonalize this construction by using the singular-value decomposition $A = UDV$, where U is a unitary square matrix, D is diagonal and V is a rectangular matrix with orthonormal vectors as rows. With this, the ground state reads

$$|\psi\rangle = \sum_{m,n,o} U_{mn} D_{nn} V_{no} |\psi_m^1\rangle |\psi_o^2\rangle \tag{1.2.2}$$

Defining $|\Phi_m^1\rangle = U|\psi_m^1\rangle$ as well as $|\Phi_n^2\rangle = V|\psi_n^2\rangle$ and one arrives at the Schmidt decomposition,

$$|\psi\rangle = \sum_{n} D_{nn} |\Phi_n^1\rangle |\Phi_n^2\rangle \tag{1.2.3}$$

Now, both $|\Phi_n^i\rangle$ are orthonormal in both Hilbert spaces where the number of elements is limited by the dimension of the smaller Hilbert space. From this construction one can immediately read off the information about the entanglement between the two subsystems. For this purpose it is instructive to look at the two extremal examples. On the one hand, if only one element of D is finite, the ground state is a product state and consequently no entanglement is present. On the other hand, if all elements of D are equal, one has a maximally entangled state.

More generally, the entanglement is most often described[56] via the reduced density matrix of the bipartition. It is calculated from the full density matrix of the system,

$\rho = |\psi\rangle\langle\psi|$ by tracing over the degrees of freedom of one of the subsystems, i.e.,

$$\rho_1 = \text{tr}_2(|\psi\rangle\langle\psi|). \tag{1.2.4}$$

Using the Schmidt decomposition, we can see the connection to the entanglement of the ground state,

$$\rho_1 = \sum_n |D_{nn}|^2 |\Phi_n^1\rangle\langle\Phi_n^1| = \sum_n \lambda_n |\Phi_n^1\rangle\langle\Phi_n^1|. \tag{1.2.5}$$

Here, we have chosen to trace out the degrees of freedom of subsystem two, but the result would hold equally for the opposite case. One can show[56] that the finite eigenvalues for both cases are identical and hence the reduced density matrix is a well-defined measure of the entanglement between subsystems. The set of eigenvalues is often called the entanglement spectrum and contains the full information about the entanglement of the two subsystems. Since the reduced density matrix is hermitian, one can define

$$\rho_i = \frac{1}{\mathcal{Z}} e^{-H_i}, \tag{1.2.6}$$

where $\mathcal{Z} = \text{Tr}(\rho_i)$. The matrix H_i,called the entanglement Hamiltonian, is defined through (1.2.6). In a free electron model, one can show[56] that the entanglement Hamiltonian is quadratic as well.

It is possible to define the von Neumann entropy with respect to the reduced density matrix, generally called the entanglement entropy,

$$S_i = -\text{tr}(\rho_i \ln(\rho_i)) = -\sum_n \lambda_n \ln(\lambda_n). \tag{1.2.7}$$

As was discussed above, the finite eigenvalues of the reduced density matrices of each

subsystem are equal and consequently this is true for the entanglement entropies of the different subsystems as well. In addition, for a product state, the entropy vanishes. Hence, the entanglement entropy is commonly used as a measure for the entanglement as it is easily computed and can be interpreted as the logarithm of the number of effective states of the Schmidt decomposition.

It has been shown[49, 50] that the entanglement entropy contains information about the topology of the system in the form of a universal constant, called the topological entanglement entropy, that depends on the topological properties of the system. However, as we have seen above, symmetry protected topological states are not topological in the strict sense and thus, the topological entanglement entropy vanishes. Nonetheless, there can be some signature of a topological phase transition in a topological superconductor, as will be shown in this thesis.

1.3 Weyl semimetals

Up to this point we have solely talked about gapped topological phases, but recently it was discovered that having a gap is not a requirement for topologically protected states. Topological semimetals[57–60] have sparked an intense research activity in recent years and most prominently Weyl as well as Dirac[61–65] semimetals have been discovered experimentally. In these three dimensional materials the band gap is closed at a certain number of points in the Brillouin zone which has severe consequences for their response functions as well as edge states. In Weyl semimetals, the Hamiltonian can be approximated around these band touching points, also called Weyl nodes, as

$$H(\mathbf{k}) = \chi v_F \left(\sigma_x k_x + \sigma_y k_y + \sigma_z k_z\right), \tag{1.3.1}$$

where one can think of σ_i denoting the spin of the electron and any possible anisotropy has been absorbed into the definition of the momentum $\mathbf{k}$. Here, $\chi = \pm 1$ denotes the chirality of the node.

In two-dimensional systems, for example the topological superconductors discussed above, one could apply a magnetic field $\mathbf{B}$ to gap out the system. However, in the semimetal case, the application of the magnetic field will have the effect of shifting the momentum vector $\mathbf{k} \to \mathbf{k} + \mathbf{B}/v_F$, but not inducing a gap, implying some sort of topological protection that prohibits a gap from opening.

In order to understand the cause of the protection, we need to look at the Berry connection $\mathbf{A}(k) = \sum_n i\langle\psi_n(k)|\nabla|\psi_n(k)\rangle$, where the sum is over the occupied bands, from which the Berry curvature $\mathbf{\Omega} = \nabla \times \mathbf{A}$ can be derived. The band-touching points $k_\pm$ are sources and drains of the Berry curvature and at these points the Berry curvature takes the form $\mathbf{\Omega} = \pm\delta^3(k - k_\pm)$ and consequently can only be annihilated when two points of opposite chirality merge. Thus, the existence of the band touching points is protected by the separation of the Weyl nodes in momentum space.

This topological nature has direct consequences on the surface excitations of a Weyl semimetal. If we consider a model with only two Weyl nodes separated in the z-direction in momentum space, each perpendicular two-dimensional slice is a gapped Chern insulator. As we have seen above, each node is the source (or drain) or Berry flux and thus when we sweep along z, the Chern number must change at the Weyl node. Thus, between the two Weyl nodes of opposite chirality the two-dimensional subsystem will be non-trivial with Chern number $C = 1$ and outside it will be be trivial. Introducing a slab geometry, for example by introducing surfaces parallel to the $y - z$-surface, will add a surface to each two-dimensional Chern insulator. Consequently, when looking at a non-trivial slice between the two Weyl nodes, there must be a zero-energy mode somewhere along the boundary. This must be true for each surface spanning the range

from one node to the other. Only when going from a slice with $C = 1$ to the regime with $C = 0$ does the zero mode vanish. Hence, the zero-energy states for each slice form an arc spanning from the projection of one Weyl node to the other, a so-called Fermi arc.

A second consequence, as mentioned above, is the response to applied electromagnetic fields due to the fact that a Weyl node is the source for the Berry Curvature and possesses a chiral anomaly. Looking only at a single node, charge conservation is violated and this leads to the continuity equation,

$$\partial_\mu j^\mu = -\chi \frac{e^2}{4\pi^2 \hbar^2 c} \mathbf{E} \cdot \mathbf{B}, \tag{1.3.2}$$

where χ again denotes the chirality of the node. Consequently, nodes always appear in pairs of opposite chirality in real systems, restoring charge conservation. This is the physical interpretation of the Nielsen-Ninomiya theorem[66, 67]. This somewhat subtle response leads to directly measurable phenomena such as the chiral magnetic or the anomalous Hall effect.

It is important to stress that the aforementioned effects require for the Weyl nodes to be separated in momentum space. This assumes, first of all, that either time reversal or inversion symmetry is broken as otherwise the bands would be degenerate and would combine two nodes of opposite chirality at one point in the Brillouin zone. Second of all, the distinction between two different points in the Brillouin zone assumes that crystal momentum is well-defined and translational symmetry is intact. This implies that when translation invariance is lost, for example by the introduction of disorder, the clear separation of the Weyl nodes is also lost as impurities could introduce non-zero amplitudes to scatter between two distinct nodes, thus introducing a finite energy gap. However, in applications disorder is normally not strong enough to completely destroy the topological nature of the Weyl nodes and the band structure should retain its

characteristic features.

1.4 Outline of this Thesis

The remainder of this thesis is organized as follows. Chapter two starts off with the numerical calculation of the entanglement entropy for a spin-orbit coupled two-dimensional superconductor that experiences a topological phase transition. The focus of this chapter is to establish whether or not the entanglement entropy is sensitive to the phase transition and what effect the different possible partitions can have on the result. In chapter three this analysis is augmented by an analytical calculation for the large-Zeeman-coupling limit and a specific shape of partition. Again, the topological phase transition is examined and its signature in the entanglement entropy is derived. Subsequently, chapter four takes a step towards realistic quantum systems and introduces a random disorder potential to the system of chapter two. Through the application of a real-space Chern number, the entanglement entropy and a perturbative approach, the effect of the disorder on the topological phase transition occurring in the clean system is analyzed. Chapter five extends the scope of the thesis to gapless topological phases and analyzes the effect of an applied magnetic field on a Weyl semimetal. Chapter six then completes the work with a conclusion.

Before moving on to the first manuscript, a few remarks are in order. All four chapters following the introduction were written to be self-contained with their own introduction and bibliography. In order to maintain a coherent structure of the thesis, each chapter has a preface that places the manuscript in the context of the thesis as a whole and provides a connection to the preceding and following chapters.

References

[1]X.-L. Qi and S.-C. Zhang, Rev. Mod. Phys. **83**, 1057–1110 (2011).

[2]M. Z. Hasan and C. L. Kane, Rev. Mod. Phys. **82**, 3045–3067 (2010).

[3]C. L. Kane and E. J. Mele, Phys. Rev. Lett. **95**, 146802 (2005).

[4]C. L. Kane and E. J. Mele, Phys. Rev. Lett. **95**, 226801 (2005).

[5]B. A. Bernevig, T. L. Hughes, and S.-C. Zhang, Science **314**, 1757–1761 (2006).

[6]J. E. Moore and L. Balents, Phys. Rev. B **75**, 121306 (2007).

[7]L. Fu, C. L. Kane, and E. J. Mele, Phys. Rev. Lett. **98**, 106803 (2007).

[8]M. König, S. Wiedmann, C. Brüne, A. Roth, H. Buhmann, L. W. Molenkamp, X.-L. Qi, and S.-C. Zhang, Science **318**, 766–770 (2007).

[9]Y. Xia, D. Qian, D. Hsieh, L. Wray, A. Pal, H. Lin, A. Bansil, D. Grauer, Y. S. Hor, R. J. Cava, and M. Z. Hasan, Nat Phys **5**, 398–402 (2009).

[10]A. Kitaev, Annals of Physics **321**, 2–111 (2006).

[11]L. Balents, Nature **464**, 199–208 (2010).

[12]D. C. Tsui, H. L. Stormer, and A. C. Gossard, Phys. Rev. Lett. **48**, 1559–1562 (1982).

[13]R. B. Laughlin, Phys. Rev. Lett. **50**, 1395–1398 (1983).

[14]D. J. E. Callaway, Phys. Rev. B **43**, 8641–8643 (1991).

[15]A. Kitaev, AIP Conference Proceedings **1134**, 22–30 (2009).

[16]A. P. Schnyder, S. Ryu, A. Furusaki, and A. W. W. Ludwig, AIP Conference Proceedings **1134**, 10–21 (2009).

[17]S. Ryu, A. P. Schnyder, A. Furusaki, and A. W. W. Ludwig, New Journal of Physics **12**, 065010 (2010).

[18]A. P. Schnyder, S. Ryu, A. Furusaki, and A. W. W. Ludwig, Phys. Rev. B **78**, 195125 (2008).

[19]A. Altland and M. R. Zirnbauer, Phys. Rev. B **55**, 1142–1161 (1997).

[20]J. C. Y. Teo, L. Fu, and C. L. Kane, Phys. Rev. B **78**, 045426 (2008).

[21]L. Fu, Phys. Rev. Lett. **106**, 106802 (2011).

[22]C.-K. Chiu, H. Yao, and S. Ryu, Phys. Rev. B **88**, 075142 (2013).

[23]T. Morimoto and A. Furusaki, Phys. Rev. B **88**, 125129 (2013).

[24]E. Majorana, Nuovo Cimento **5**, 171 (1937).

[25]P. Minkowski, Physics Letters B **67**, 421–428 (1977).

[26]R. N. Mohapatra and G. Senjanovi ć, Phys. Rev. Lett. **44**, 912–915 (1980).

[27]J. Schechter and J. W. F. Valle, Phys. Rev. D **22**, 2227–2235 (1980).

[28]A. Y. Kitaev, Physics-Uspekhi **44**, 131 (2001).

[29]D. Aasen, M. Hell, R. V. Mishmash, A. Higginbotham, J. Danon, M. Leijnse, T. S. Jespersen, J. A. Folk, C. M. Marcus, K. Flensberg, and J. Alicea, Phys. Rev. X **6**, 031016 (2016).

[30]P. G. Kealey, T. M. Riseman, E. M. Forgan, L. M. Galvin, A. P. Mackenzie, S. L. Lee, D. M. Paul, R. Cubitt, D. F. Agterberg, R. Heeb, Z. Q. Mao, and Y. Maeno, Phys. Rev. Lett. **84**, 6094–6097 (2000).

[31]G. M. Luke, Y. Fudamoto, K. M. Kojima, M. I. Larkin, J. Merrin, B. Nachumi, Y. J. Uemura, Y. Maeno, Z. Q. Mao, Y. Mori, H. Nakamura, and M. Sigrist, Nature **394**, 558–561 (1998).

[32]A. P. Mackenzie and Y. Maeno, Rev. Mod. Phys. **75**, 657–712 (2003).

[33]J. Jang, D. G. Ferguson, V. Vakaryuk, R. Budakian, S. B. Chung, P. M. Goldbart, and Y. Maeno, Science **331**, 186–188 (2011).

[34]N. Read and D. Green, Phys. Rev. B **61**, 10267 (2000).

[35]D. A. Ivanov, Phys. Rev. Lett. **86**, 268–271 (2001).

[36]J. Alicea, Reports on Progress in Physics **75**, 076501 (2012).

[37]L. Fu and C. L. Kane, Phys. Rev. Lett. **100**, 096407 (2008).

[38]J. D. Sau, R. M. Lutchyn, S. Tewari, and S. Das Sarma, Phys. Rev. Lett. **104**, 040502 (2010).

[39]J. Alicea, Phys. Rev. B **81**, 125318 (2010).

[40]R. M. Lutchyn, J. D. Sau, and S. Das Sarma, Phys. Rev. Lett. **105**, 077001 (2010).

[41]Y. Oreg, G. Refael, and F. von Oppen, Phys. Rev. Lett. **105**, 177002 (2010).

[42]V. Mourik, K. Zuo, S. M. Frolov, S. R. Plissard, E. P. A. M. Bakkers, and L. P. Kouwenhoven, Science **336**, 1003–1007 (2012).

[43]S. Nadj-Perge, I. K. Drozdov, J. Li, H. Chen, S. Jeon, J. Seo, A. H. MacDonald, B. A. Bernevig, and A. Yazdani, Science **346**, 602–607 (2014).

[44]J. Liu, A. C. Potter, K. T. Law, and P. A. Lee, Phys. Rev. Lett. **109**, 267002 (2012).

[45]G. Kells, D. Meidan, and P. W. Brouwer, Phys. Rev. B **86**, 100503 (2012).

[46]D. I. Pikulin, J. P. Dahlhaus, M. Wimmer, H. Schomerus, and C. W. J. Beenakker, New Journal of Physics **14**, 125011 (2012).

[47]X. Chen, Z.-C. Gu, and X.-G. Wen, Phys. Rev. B **82**, 155138 (2010).

[48]H.-C. Jiang, Z. Wang, and L. Balents, Nat Phys **8**, 902–905 (2012).

[49]A. Kitaev and J. Preskill, Phys. Rev. Lett. **96**, 110404 (2006).

[50]M. Levin and X.-G. Wen, Phys. Rev. Lett. **96**, 110405 (2006).

[51]S. V. Isakov, M. B. Hastings, and R. G. Melko, Nat Phys **7**, 772–775 (2011).

[52]A. Einstein, B. Podolsky, and N. Rosen, Phys. Rev. **47**, 777–780 (1935).

[53]E. Schrödinger, Mathematical Proceedings of the Cambridge Philosophical Society **31**, 555–563 (1935).

[54]E. Schrödinger, Mathematical Proceedings of the Cambridge Philosophical Society **32**, 446–452 (1936).

[55]E. Schmidt, Mathematische Annalen **63**, 433–476 (1907).

[56]I. Peschel, Brazilian Journal of Physics **42**, 267–291 (2012).

[57]X. Wan, A. M. Turner, A. Vishwanath, and S. Y. Savrasov, Phys. Rev. B **83**, 205101 (2011).

[58]K.-Y. Yang, Y.-M. Lu, and Y. Ran, Phys. Rev. B **84**, 075129 (2011).

[59]A. A. Burkov and L. Balents, Phys. Rev. Lett. **107**, 127205 (2011).

[60]G. Xu, H. Weng, Z. Wang, X. Dai, and Z. Fang, Phys. Rev. Lett. **107**, 186806 (2011).

[61]Z. Wang, Y. Sun, X.-Q. Chen, C. Franchini, G. Xu, H. Weng, X. Dai, and Z. Fang, Phys. Rev. B **85**, 195320 (2012).

[62]Z. Wang, H. Weng, Q. Wu, X. Dai, and Z. Fang, Phys. Rev. B **88**, 125427 (2013).

[63]S. Borisenko, Q. Gibson, D. Evtushinsky, V. Zabolotnyy, B. Büchner, and R. J. Cava, Phys. Rev. Lett. **113**, 027603 (2014).

[64]Z. K. Liu, B. Zhou, Y. Zhang, Z. J. Wang, H. M. Weng, D. Prabhakaran, S.-K. Mo, Z. X. Shen, Z. Fang, X. Dai, Z. Hussain, and Y. L. Chen, Science **343**, 864–867 (2014).

[65]M. Neupane, S.-Y. Xu, R. Sankar, N. Alidoust, G. Bian, C. Liu, I. Belopolski, T.-R. Chang, H.-T. Jeng, H. Lin, A. Bansil, F. Chou, and M. Z. Hasan, Nat Commun **5** (2014).

[66]H. Nielsen and M. Ninomiya, Physics Letters B **105**, 219–223 (1981).

[67]D. Friedan, Communications in Mathematical Physics **85**, 481–490 (1982).

Preface to Chapter 2

In this first manuscript we introduce the entanglement entropy for a topological superconductor and establish its ability to indicate the phase transition when moving from the trivial to the topological phase. We show how the use of different partitions of a system enables one to extract various different properties of the topological superconductor.

2

Entanglement Spectrum as a Probe for the Topology of a Spin-Orbit Coupled Superconductor

Jan Borchmann[1] and Aaron Farrell[1] and Shunji Matsuura[1] and T. Pereg-Barnea[1]

[1]Department of Physics and the Centre for Physics of Materials, McGill University, Montreal, Quebec, Canada H3A 2T8

This chapter has been published in Physical Review B. Journal Reference: Physical Review B 90, 235150 (2014)

Abstract

The classification of electron systems according to their topology has been at the forefront of condensed matter research in recent years. It has been found that systems of the same symmetry, previously thought of as equivalent, may in fact be distinguished by their topological properties. Moreover, the non-trivial topology found in some insulators and superconductors has profound physical implications that can be observed experimentally and can potentially be used for applications. However, characterizing a system's topology is not always a simple task, even for a theoretical model. When translation and other symmetries are present in a quadratic model the topological invariants are readily defined and easily calculated in a variety of symmetry classes. However, once interactions or disorder come into play the task becomes difficult, and in many cases prohibitively so. The goal of this paper is to test whether the entanglement entropy and entanglement spectrum bare signatures of the system's topology. Using quadratic models of superconductors we demonstrate that these entanglement properties are sensitive to changes in topology.

2.1 Introduction

Over the past several years the study of topology in condensed matter systems has become a topic of great interest. The topological properties of quantum Hall systems were studied since the 80's[1], topological systems with time-reversal symmetry were only predicted[2, 3] and realized[4] recently. The introduction of topology into the discussion of solid-state phenomena has revolutionized the classification of materials. For instance, two insulating states in the same dimension and symmetry class, formerly thought of as being equivalent, could have a different topology and are not the same state of matter. This classification is also supported by the direct physical implications of non-trivial topology, namely localized modes on system boundaries[5–7]. These modes are current carrying states on sample surfaces and Majorana fermions in vortex cores of topological superconductors.

In light of the above, it is desirable to assign a label which carries the information about the topology to any system of interest. This is easy to do in a non-interacting system with translation invariance as it is described by a periodic, quadratic Hamiltonian. This label is the 'topological invariant', which is an integer number, related to Berry curvature in the Brillouin zone. Loosely speaking, the invariant measures the phase winding of single-particle states as the momentum is scanned in the Brillouin zone. For example, in a two-dimensional superconductor with broken time reversal symmetry, such as the model in the following discussion, the topological invariant is a Chern number, the integral of the Berry curvature over the Brillouin zone. Calculating the Chern number requires knowing the single particle wave function at any point in the Brillouin zone and the presence of additional symmetries (like mirror or particle-hole) simplify the procedure greatly.

The ease with which one can evaluate the topological invariants in a non-interacting,

clean system, unfortunately, does not carry over to dirty and/or interacting systems. While breaking of translation invariance by disorder prevents the use of lattice momentum, interactions invalidate the notion of a single particle wave function altogether. K-theory classification[8–10] itself is valid in non-interacting dirty systems and there are formal ways of evaluating the topological invariants for interacting systems. This could be based on flux insertion, similar to Laughlin's argument for quantum Hall systems[3] or using Green's functions[11, 12]. However, these methods are not easy to implement, especially in situations where the ground state (only) is found numerically and given as a superposition of many configurations. It is therefore desired to devise an alternative way of distinguishing a topological state from a trivial one in the presence of disorder and interactions and in a way that utilizes the ground state only, without requiring the full spectrum (or Green's function). For this reason we turn to study the entanglement entropy (EE) and entanglement spectrum (ES). We follow several authors who considered clean and non-interacting systems [13–15] and extend the study to other models of topological superconductors. Like previous authors we find that the topology is manifested in the entanglement properties in various ways. We extend the previous studies and point to universal behaviour that can be potentially used in more complicated cases[16].

The entanglement entropy and spectrum will be defined in the next section. Before presenting the formal definitions, let us simply note that these include dividing the system into subsystems A and B and tracing out degrees of freedom associated with subsystem B. Early applications of the entanglement entropy were concerned with how the entanglement entropy depends on the length of the boundary between the two subsystems. It was shown that, in two dimensions, if one considers a system with vanishing correlation length that the leading term in the entanglement entropy is linear[17, 18], a property referred to as the *area law*. Interestingly, in certain cases, the subleading length dependence of the entanglement entropy is directly related to topology. This

subleading term, $-\gamma$ is called the 'topological entanglement entropy'. The cases for which γ is non-zero are gapless topologically ordered states[19, 20] to be distinguished from the systems discussed in this work.

Although related to the topological ordering discussed above, topological insulators and topological superconductors are a different class. A topological superconductor (or insulator) is a 'symmetry protected topological state' (see for example Ref. [21] for the distinction), meanwhile the topological order discussed above (where γ is nonzero) is defined through long-range entanglement[22]. The bulk of a symmetry protected topological state is trivial from the point of view of topological order and therefore posses no topological entanglement entropy, i.e., $\gamma = 0$. [1]

For the reason discussed above we cannot rely on γ to distinguish between a topological and a trivial superconductor (or insulator). It is therefore natural to ask if the entanglement entropy contains any other signature that can be used to distinguish between a topological and a trivial phase in a symmetry protected topological state. Several proposals have been made over the past couple of years and we will outline the ones relevant to the current work. First, it has been shown that as one tunes model parameters across a topological phase transition a peak in the derivative of the entanglement entropy can be seen[13]. This singularity occurs despite a lack of a rapidly changing γ, signalling the sensitivity of other terms in the entanglement entropy to the (symmetry protected) topology change. Second, one may also look for other subleading terms that contain potential information on the topology of the system. For example, there are logarithmic terms in the presence of corners and long range order[25].

Signatures of the topology of symmetry protected states can also be found in the

[1] The charged topological entanglement entropy [23], which is a universal sub-leading term of the charged entanglement entropy[24], distinguishes symmetry protected topological phases from trivial phases. On the other hand, as we show below, the leading term is sensitive to the topology, as might be expected, since the entanglement entropy is closely related to correlations.

entanglement spectrum. Again, the entanglement spectrum will be defined in the next section. It is the spectrum of an auxiliary hamiltonian associated with the entanglement entropy. The entanglement spectrum is sensitive to the type of partition applied. For a partition whose boundary prevails throughout the whole sample, it has been shown that the low-lying entanglement spectrum mimics the excitation spectrum near a physical boundary, although the system may be fully periodic[26, 27]. Moreover, Hsieh and Fu[28] showed that for an extensive partitioning the topological spectrum is related to bulk properties. In this case, discussed below, a topological phase transition in the form of a gap closure can be seen in the entanglement spectrum by varying the partition only, even when the system parameters are unchanged.

The goal of this paper is to apply the tools outlined above to models of topological superconductors relevant for the search for Majorana fermions. In particular, the two models we consider describe spin-orbit coupled superconductors with various order parameters. We consider a superconductor with $d + id$-wave order parameter symmetry. This model is the mean field limit of an interaction driven superconductor with spin orbit coupling which has been studied previously by two of us[29–31]. We also consider an s-wave order parameter, motivated by recent proposals to realize topological superconductivity in heterostructures[32, 33]. In these proposals superconductivity is achieved by proximity to an s-wave superconductor. It should be noted that in both the above models the pairing term is in the singlet s- or d-wave channel. However, the presence of spin-orbit coupling forces the projection of this order parameter on to the spin-orbit coupled band. In each band the projected order parameter acquires additional phase winding which alters the order parameter symmetry. When there's only one relevant band the superconductor is topological with effective p- or f- symmetry.

The main findings of our study are as follows. (i) When varying model parameters such that the system changes its topology, the derivatives of the entanglement entropy

with respect to model parameters are sharply peaked at the transition. This extends a previous observation by Oliveira[13] to an additional system. This result holds even for very small subsystem sizes and could therefore find potential use in a more complicated system. (ii) Any effort to find subleading terms to the area law in our models using a 'finite' partition to A and B subsystems were overwhelmed by finite size effects. This is in contrast to previous studies[13, 14] where no such problems were reported. Owing to this, studies based on subleading terms of more complicated systems may be of limited scope. However, by adopting a corner-less partition we were able to simulate large systems. We establish that any possible subleading terms in the EE have to be due to corners[34], as all sub-leading contributions are negligible in the corner-less partition. Moreover, this shows that the slope in the area law is sensitive to the topology of the system and discontinuous at the phase boundary. Plotting this coefficient in parameter space is then a useful method for searching for a topological phase boundary. (iii) The entanglement spectrum of the corner-less partition provides a nice illustration of the connection between the low energy states in the entanglement spectrum of a partition with a prevailing edge and the low energy states of a physical system[26, 27] with an edge for this model. (iv) In our model of a topological superconductor, a topological phase transition can be seen in the entanglement spectrum by varying the partition. This result extends the work of Hsieh and Fu[28] on topological insulators to the case of topological superconductors and supports their general arguments.

The rest of this Paper is organized as follows: In the next section we introduce the entanglement spectrum, entanglement entropy, and our model framework. In Section 2.3 we present and discuss our results of the entanglement entropy in parameter space while in Section 2.4 we study the entanglement entropy as a function of system size. Section 2.6 contains our partition tuning study and concluding remarks are presented in Section 2.7.

2.2 Model and Methods

2.2.1 The Reduced Density Matrix, Entanglement Spectrum and Entanglement Entropy

We start by defining the reduced density matrix, the entanglement spectrum, and the entanglement entropy. We also discuss how they are obtained relatively simply in a non-interacting system. Starting from a ground state $|\psi\rangle$ one defines the reduced density matrix by dividing the system into two parts, A and B. The reduced density matrix[26] of subsystem A is given by

$$\rho_A = \mathrm{Tr}_B \left(|\psi\rangle\langle\psi| \right) \equiv \frac{e^{-H_A}}{Z_A}, \tag{2.2.1}$$

where the trace is over all configurations of subsystem B and the above equation serves as the definition of H_A, the entanglement Hamiltonian. The entanglement spectrum is defined as the set of eigenvalues $\{E_i\}$ of the entanglement Hamiltonian, H_A. $Z_A = \mathrm{Tr}_A(e^{-H_A})$ is the partition function. The entanglement entropy (EE) we choose to work with is the von-Neuman entropy, defined by:

$$S_A = -\mathrm{Tr} \left(\rho_A \log \rho_A \right) \tag{2.2.2}$$

We now specialize our discussion to the system at hand: a quadratic system with superconductivity. In order to calculate the ES we appeal to the fact that the entanglement spectrum of a quadratic system is completely determined by its correlations. To show this we generalize a method proposed in Refs. [35, 36]. We briefly review the main steps of the method here, adjusted to the case of a superconductor. Consider a state $|\psi\rangle$ which is the ground state of some quadratic Hamiltonian. $|\psi\rangle$ is a Slater determinant of

single particle states and therefore obeys Wick's theorem. Now let us consider averages $C_{i,j} = \langle c_i^\dagger c_j \rangle$ where i, j are both in subsystem A. This average must be completely determined by the reduced density matrix ρ_A. Moreover, since $|\psi\rangle$ is a determinant all averages must obey Wick's theorem. Therefore for any local operator $\mathcal{O}_A$ in subsystem A, $\langle \mathcal{O}_A \rangle = \text{Tr}\,(\rho_A \mathcal{O}_A)$ and the trace must obey Wick's theorem. It follows that ρ_A is an exponent of a quadratic entanglement Hamiltonian. Further, if $|\psi\rangle$ is a ground state with some pairing (*i.e.* a BCS like wave function) then the anomalous averages $\langle c_i^\dagger c_j^\dagger \rangle$ must be non-zero. From this it follows that H_A must also contain pairing.

The considerations above lead us to write a general form for H_A as follows

$$H_A = \sum_{i,j \in A} \left(c_i^\dagger h_{i,j} c_j + \frac{1}{2} \left(c_i^\dagger \Delta_{i,j} c_j^\dagger + \text{h.c.} \right) \right) \tag{2.2.3}$$

where i, j label both site and spin in subsystem A. The above Hamiltonian can be written as $H_A = \psi^\dagger \mathcal{H} \psi$ where $\psi = (c_1 ... c_N, c_1^\dagger .. c_N^\dagger)^T$. The matrix $\mathcal{H}$ obeys particle-hole symmetry and thus it can be diagonalized as $\mathcal{H} = W D W^\dagger$ where $D = \text{diag}(E, -E)$ where $E = \text{diag}(E_1 .... E_N)$ with $E_i > 0 \; \forall i$ and

$$W = \begin{pmatrix} u & v^* \\ v & u^* \end{pmatrix}, \tag{2.2.4}$$

where u and v are matrices in position and spin space. If we now define the correlation matrix

$$G = \begin{pmatrix} \langle c_i c_j^\dagger \rangle & \langle c_i c_j \rangle \\ \langle c_i^\dagger c_j^\dagger \rangle & \langle c_i^\dagger c_j \rangle \end{pmatrix} \tag{2.2.5}$$

and calculate the averages in terms of traces over ρ_A, one can show that G can be represented as $G = W \tilde{G} W^\dagger$ where $\tilde{G} = \text{diag}(I - f, f)$ with $f = \text{diag}(n_f(E_1) .... n_f(E_N))$ with $n_f(x) = 1/(1 + e^x)$. We now make the observation that G and $\mathcal{H}$ are diagonalized

by the same transformation. Therefore if we define the first N eigenvalues of G as $\zeta_i = 1 - f(E_i)$ then the entanglement spectrum is given by $E_i = \ln\left(\frac{\zeta_i}{1-\zeta_i}\right)$. Thus the entanglement spectrum is obtained via the following program. Using a ground state $|\psi\rangle$ we calculate $G_{i,j}$ for i, j in subsystem A, diagonalize the matrix G and then use its eigenvalues to obtain the entanglement spectrum.

Using the relation between the entanglement entropy and the entanglement Hamiltonian in Eq. (2.2.2) and $\zeta_i = 1 - f(E_i)$, we find

$$S_A = -\sum_i (\zeta_i \ln \zeta_i + (1-\zeta_i)\ln(1-\zeta_i)), \tag{2.2.6}$$

which is just the entropy of a free fermionic gas with energies E_i. For a vanishing correlation length, as expected for an insulator, the entropy has the form

$$S_A = \alpha L - \gamma + \mathcal{O}(1/L), \tag{2.2.7}$$

where L is the length of the partition between the two sub-systems. The first term, proportional to L is referred to as the area law and the sub-leading term γ is called the 'topological entanglement entropy'[17, 18]. This term only depends on the topology of the ground state and is thus universal. Since the entanglement Hamiltonian of a 2+1d topological system is related to the Hamiltonian of (1+1)d conformal field theory[17], one could obtain the above expression by taking the large L limit of the CFT partition function.

For our bulk model we expect γ to be zero[13, 14] since our topological state is a symmetry protected one. The assumption of a vanishing correlation length ξ is justified, as long as the characteristic length of each subsystem is large compared to ξ. However, this assumption is violated due to the presence of corners, where the size of the partition

necessarily becomes comparable to the correlation length. Thus, one gets,

$$\alpha \to \alpha(\xi), \quad -\gamma \to -\gamma(L, \xi). \tag{2.2.8}$$

This can then lead to sub-leading terms in the entanglement entropy. In the following sections we show that in our systems any such term is associated with partition corners.

2.2.2 Quadratic Hamiltonian with Pairing

In our model we look at quadratic states with p-wave or f-wave pairing. These pairing states are the result of adding momentum-spin locking (via spin-orbit coupling) to systems which otherwise tend to pair in the singlet s- or d-wave channel[29–31]. These systems have translational invariance and can thus be diagonalized in momentum space and therefore their Chern number (the relevant topological invariant) can be calculated exactly. This means, conveniently, that the topological phase diagram is known. We can therefore use this to analyze the results given by the entanglement spectrum and entanglement entropy.

The model we consider is as follows

$$H = T + H_{SO} + H_{SC}, \tag{2.2.9}$$

where,

$$T = -\sum_{\langle i,j\rangle,\sigma} c^{\dagger}_{i,\sigma} t_{i,j} c_{i,\sigma} \tag{2.2.10}$$

is the tight binding kinetic energy where $t_{i,j}$ are the hopping amplitudes. Here we take $t_{i,j} = t_{i-j}$ and define its Fourier transform as $\epsilon_{\mathbf{k}}$. For nearest neighbour hopping on the

square lattice $\epsilon_{\mathbf{k}} = -2t(\cos k_x + \cos k_y)$. Next,

$$H_{SC} = \sum_{\mathbf{k}} \left(c_{\mathbf{k},\uparrow} \Delta_{\mathbf{k}} c_{-\mathbf{k},\downarrow} + \text{h.c.} \right), \tag{2.2.11}$$

where $\Delta_{\mathbf{k}}$ is the superconducting order parameter. In what follows when we refer to the s-wave model we mean an order parameter of the form $\Delta_{\mathbf{k}} = \Delta_0$ while $d + id$-wave symmetry means we have used $\Delta_{\mathbf{k}} = \Delta_1(\cos(k_x) - \cos(k_y)) + i\Delta_2 \sin(k_x)\sin(k_y)$. These electron pairing functions in the singlet channel transform into p- or f-wave functions when written in the spin-orbit coupled band basis. This alone does not guarantee topological superconductivity as there is usually two bands with opposite chirality. Therefore the condition for topological superconductivity is that only one relevant band participates in the pairing [33]. The spin-orbit coupling term takes the form

$$H_{SO} = \sum_{\mathbf{k}} \Psi_{\mathbf{k}}^{\dagger} \mathcal{H}_{\mathbf{k}} \Psi_{\mathbf{k}}, \tag{2.2.12}$$

where $\Psi_{\mathbf{k}} = (c_{\mathbf{k},\uparrow}, c_{\mathbf{k},\downarrow})^T$, $\mathcal{H}_{\mathbf{k}} = \mathbf{d}_{\mathbf{k}} \cdot \vec{\sigma}$ (with $\vec{\sigma}$ a vector of Pauli matrices acting on the spin). $\mathbf{d}_{\mathbf{k}}$ could in principle take any form which is convenient to describe spin-orbit coupling. Here we choose $\mathbf{d}_{\mathbf{k}} = (A \sin k_x, A \sin k_y, 2B(\cos k_x + \cos k_y - 2) + M)$ (A, B and M are material parameters which describe the various spin-orbit coupling and Zeeman strengths). This choice resembles the spin-orbit coupling term used by Bernevig, Hughes and Zhang[37] in the description of 2d topological insulators.

The hamiltonian (2.2.9) satisfies

$$U_C H^*(-k) U_C^{-1} = -H(k), \tag{2.2.13}$$

where U_C is a unitary operator $\sigma_y \otimes \mathbb{I}_2$ in the basis of $(\psi_{\mathbf{k}}, \psi_{-\mathbf{k}}^{\dagger})$. Since $U_C^* U_C = -\mathbb{I}_4$, this topological superconductor belongs to Class C[8–10].

One can block diagonalize this hamiltonian by a unitary transformation and the topological number is given by a doubled Chern number. Defining $\xi_{\mathbf{k}} = \epsilon_{\mathbf{k}} - \mu$ the Chern number is given by[12, 29, 30]

$$C_1 = \frac{1}{i\pi} \log \left[\frac{Q(0,0)Q(\pi,\pi)}{Q(\pi,0)Q(0,\pi)} \right], \tag{2.2.14}$$

where $Q(\mathbf{k}) = \text{sgn}(|\Delta_{\mathbf{k}}|^2 + \xi_{\mathbf{k}}^2 - \mathbf{d}_{\mathbf{k}}^2)$. For our particular model we have $Q(0,\pi) = Q(\pi,0)$, regardless of parameters. We are therefore left with

$$C_1 = \frac{1}{i\pi} \log \left(\text{sgn} \left[(|\Delta_0|^2 + \xi_0^2 - \mathbf{d}_0^2)(|\Delta_{\mathbf{Q}}|^2 + \xi_{\mathbf{Q}}^2 - \mathbf{d}_{\mathbf{Q}}^2) \right] \right), \tag{2.2.15}$$

where $\mathbf{Q} = (\pi, \pi)$. Using the above formulation we can map the topological phase diagram of the superconductor described by the Hamiltonian H.

2.3 Topological Phase Boundary and Entanglement Entropy

When plotting the entanglement entropy and its derivatives with respect to the model's spin-orbit coupling parameters we see the following intriguing property. The topological phase boundaries of our model coincide with “kinks" in the entanglement entropy. That is, there's a change in behavior of the entanglement entropy at the transition from a trivial superconductor to a topological superconductor. These kinks are seen as a strong peak in the derivative of the entanglement entropy with respect to material parameters. To make a rather loose analogy with standard thermodynamic variables, the transition appears to be a second order phase transition. A similar property was found in a spin-orbit coupled triplet superconductor in Ref. [13].

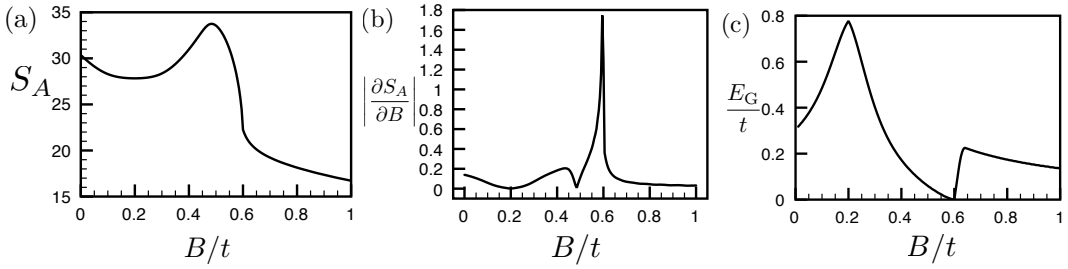

Figure 2.1: Plot of the entanglement entropy across the phase boundary for the d-wave system. Figure (a) shows the entanglement entropy S_A for subregion A a square of side length 12, figure (b) gives $\frac{\partial S_A}{\partial B}$ for the same geometry and figure (c) plots the bulk energy gap as a function of B. In the figure we have fixed $\mu = 0, A = 0.25t, M = 0.8t, \Delta_1 = 0.8t$ and $\Delta_2 = 0.4t$. $B/t = 0.6$ is the critical point and $B/t < 0.6$ $(B/t > 0.6)$ corresponds to the trivial (topological) phase. Notice that the entanglement entropy takes larger values in the trivial phases. This result is different than that of the s-wave topological superconductor shown in Fig.2.3.

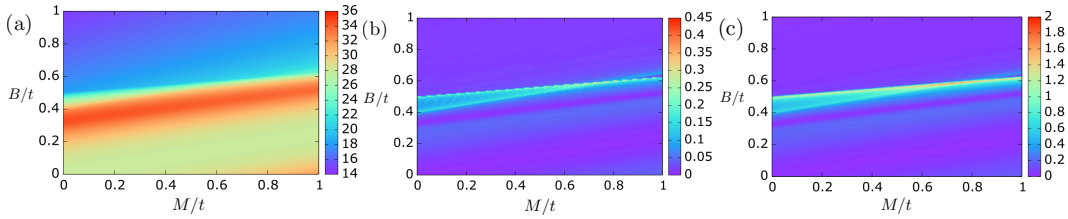

Figure 2.2: Plot of the entanglement entropy for the d-wave system and its derivatives in MB space. We have (a) the entropy, S_A, (b) its derivative $\left|\frac{\partial S_A}{\partial M}\right|$, and (c) the derivative $\left|\frac{\partial S_A}{\partial B}\right|$. In all figures we have picked a subregion A a square of side length 20 and fixed $\mu = 0, A = 0.25t, \Delta_1 = 0.8t$ and $\Delta_2 = 0.4t$. The critical line is $B/t = (M/8t + 0.5)$ and $B/t < (M/8t + 0.5)$ $(B/t > (M/8t + 0.5))$ corresponds to the trivial (topological) phase.

In general, phase transitions between states of different topology but the same symmetry are not characterized by an order parameter. The entanglement entropy in this case serves as a substitute to a thermodynamic potential and exhibits a kink at the transition. One may expect that exactly at the transition the bulk gap should close, giving rise to that kink.

In Fig. 2.1 we present a cut through the phase diagram, where only the spin-orbit coupling parameter B is changed. In panel (a) we see that the behavior of the entanglement entropy changes abruptly at $B = 0.6t$. This change is more apparent in the derivative

of S_A in panel (b). Checking with the Chern number calculated above, we expect a topological phase transition for this choice of parameters at $B = 0.6t$; precisely where this peak occurs. $B < 0.6t$ and $B > 0.6t$ correspond to the trivial and the topological phases respectively. One might expect that a trivial phase has a smaller value of the entanglement entropy than that of a topological phase because of the absence of the mid-gap entangled states. However, the entanglement entropy of the d-wave superconductor shows the opposite result; the trivial phase has a larger value of the entanglement entropy. This suggests that in general the leading term of the entanglement entropy cannot be used alone to distinguish trivial phases from topological phases. However, it does change abruptly at the transition. In Fig. 2.1c we have plotted the bulk gap of our *full* (unpartitioned) system. The most noticeable feature of the gap is that it closes at $B = 0.6t$, as is necessary for a topological phase transition. One may also note that the maximum value of S_A occurs around $B = 0.48t$. While we are presently not certain about the origin of this maximum, we may speculate that it is related to some correlation length increase which approaches the system size at $B = 0.48t$, before the true transition at $B = 0.6t$.

To further explore this behavior we plot S_A and its relevant partial derivatives in parameter space and compare its behavior to the expected phase boundaries. First we explore this for a d-wave superconductor. We fix $\mu = 0, A = 0.25t, \Delta_1 = 0.8t$ and $\Delta_2 = 0.4t$ and explore $M - B$ space. For this specific choice of parameters and focusing on positive values of B, we expect a topological phase boundary along the line $B/t = M/8t + 0.5$. We have generated data for S_A , $\frac{\partial S_A}{\partial M}$, and $\frac{\partial S_A}{\partial B}$ for this particular choice of parameters, these are presented in Fig. 2.2.

Studying Fig. 2.2a, we see a fundamental change in the behavior of the entanglement entropy across the phase boundary line $B/t = M/8t + 0.5$. The entropy is large in the trivial phase $(B/t < (M/8t + 0.5))$ and then decreases to a lower and much slower

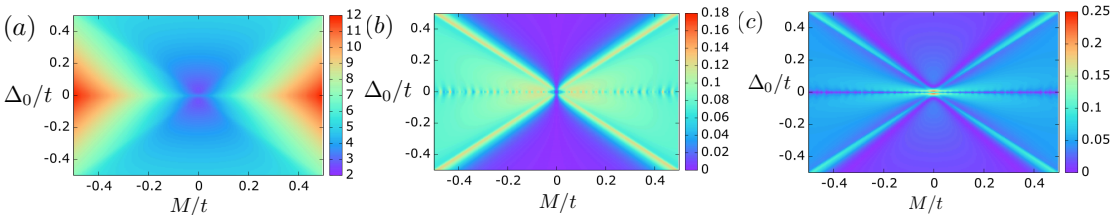

Figure 2.3: Plot of the entanglement entropy and its derivatives in $M - \Delta_0$-space for an s-wave system. From left to right we have the entropy, (a) S_A, (b) $\left|\frac{\partial S_A}{\partial M}\right|$, and (c) $\left|\frac{\partial S_A}{\partial \Delta_0}\right|$. In all figures we have picked a subregion A a square of side length 20 and fixed $\mu = -4t, A = 0.25t$ and $B = 0$. $|\Delta_0| = |M|$ is the phase transition line and $|\Delta_0| > |M|$ ($|\Delta_0| < |M|$) corresponds to the trivial (topological) phase. Notice that the entanglement entropy takes on larger values in the topological phase, which is opposite to the d-wave case.

changing value across the phase boundary line. This sudden change is more transparent in the derivatives of the entanglement entropy as panels 2.2b and 2.2c. We see in both of these figures that the derivatives are comparatively small away from the phase boundary lines and increase substantially as these critical points are approached. The exact position of the peak in the derivatives is better seen in the B derivative, as the phase boundary is rather shallow along lines of fixed B which limits our resolution in the M derivative data. Focusing on the plot of $\frac{\partial S_A}{\partial B}$, one can see a line that is formed by looking for the maximum value of $\frac{\partial S_A}{\partial B}$ for a given value of M. Fitting this line gives, to 3 decimal places, a slope of 0.125 and an intercept of $0.500t$, providing a rather convincing case that $\frac{\partial S_A}{\partial B}$ is peaked along the line $B/t = M/8t + 0.5$.

To further study these peaks and also to provide evidence that this behaviour isn't unique to the d-wave system, we have also studied the parameter space dependence of S_A in a system with s-wave superconductivity. Here we have chosen parameters such that we make as close a connection as possible with the model of Sau *et al* in Ref. [32]. We therefore set $B = 0$ and define $\tilde{\mu} = \mu + 4t$. In this case our model reduces to that of Ref. [32] when the continuum limit is taken.

Using $B = 0$, $\tilde{\mu} = \mu + 4t$, Eq. (2.2.15) and assuming $64t^2 > -\Delta_0^2 + M^2 - \tilde{\mu}^2 + 16t\tilde{\mu}$,

the Chern number is simplified to

$$C_{1,s} = \frac{\log(\text{sgn}\,[\Delta_0^2 + \tilde{\mu}^2 - M^2])}{i\pi}, \tag{2.3.1}$$

where the subscript s denotes s-wave. It then follows that if $\Delta_0^2 + \tilde{\mu}^2 - M^2 < 0$ the system is topological. Thus the topological phase boundary is defined by the equation $\Delta_0^2 + \tilde{\mu}^2 = M^2$.

We choose to fix $\tilde{\mu} = 0$ and study the resulting behavior in the M-Δ_0 plane. According to the Chern number we should see phase boundaries at $\Delta_0 = \pm|M|$. Indeed, we see strong indications of a phase boundary along this line. This behavior isn't overtly obvious in the entanglement entropy in Fig. 2.3a, however upon taking derivatives of the data with respect to M and Δ_0 it becomes more apparent. This can be seen in Figs. 2.3b and 2.3c, where strong peaks appear along the lines $\Delta_0 = M$ and $\Delta_0 = -M$. Thus we have a second clear indiction that S_A changes its behaviour across a topological phase transition. Comparing to Fig. 2.2, this demonstration has come from not only a different order parameter symmetry but also from varying a different parameter.

2.4 Functional dependence of the entanglement entropy

The study of the functional dependence of the entanglement entropy S_A on the 'surface area' of a partition A enables one to make conclusions about the ground state of the system. Deviations from the area law have been studied extensively for a variety of different models in different dimensions (see [38] for a review) and depend on the particular model and ground state under investigation. An example of this in d-dimensional models can be found in Ref. [25]. This work shows that in models with a spontaneously broken

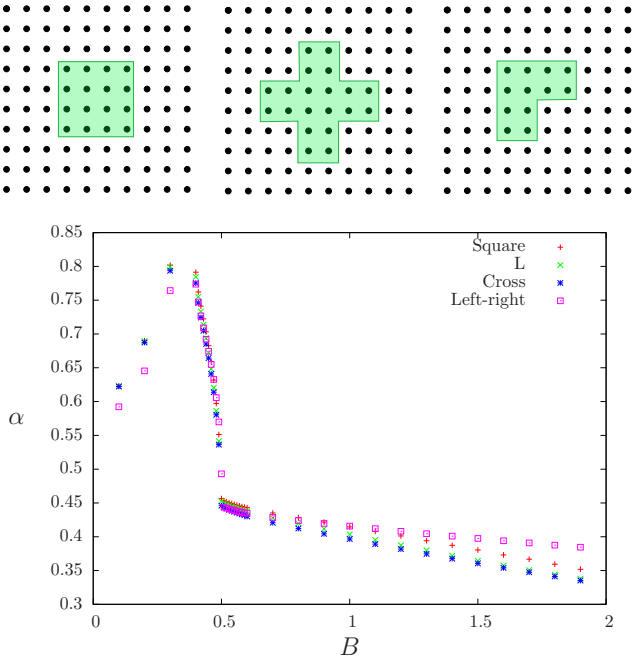

Figure 2.4: Upper panel: Schematic plot of the different shapes used for the partition of the system. From left to right: square, cross and (reflected) L-shape. Lower panel: Plot of the linear coefficient in the entanglement entropy for d-wave coupling for $M = 0$, $\mu = 0$, $\Delta_1 = 0.8t$, $\Delta_2 = 0.4t$, and $A = 0.25t$ by varying B for a square (red plus), an L-shaped (green cross), a cross shaped partition (blue star) as well as the left right partition (pink square). For this M-value the critical point is at $B = 0.5$.

continuous symmetry, the Goldstone mode causes the entanglement entropy to have a sub-leading corner correction proportional to $\ln L$, where L is the circumference of the partition. Additionally, for two-dimensional critical fermionic models, one also expects a logarithmic term, not associated with corners[39].

One difficulty in analyzing the area law is that the circumference of the partition in a lattice model is not uniquely defined. In our calculations we chose the boundary as the line that divides the distance between the outer layer of the partition and the first layer of the complement into half. This is a natural definition as every single lattice point in a line will contribute evenly to the circumference. Other definitions are possible, however, the particular choice should not affect the qualitative behavior of the area law slope, α.

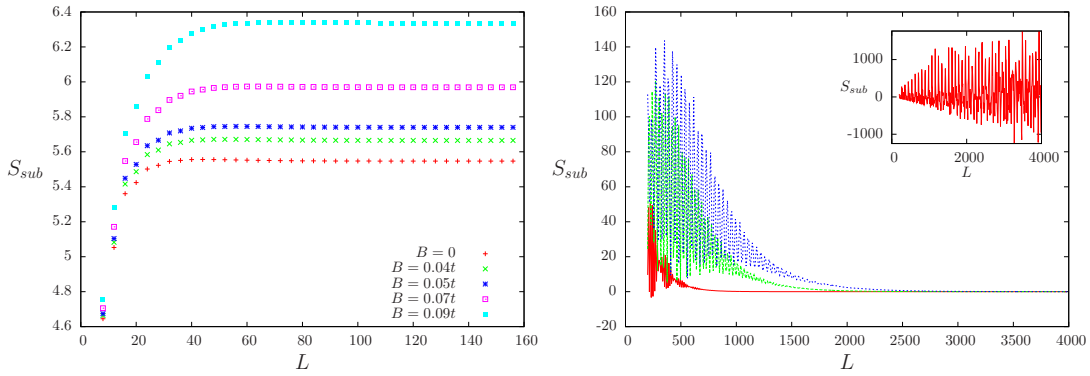

(a) (b)

Figure 2.5: Subleading dependence of a d-wave superconductor on partition size. (a) S_{sub} of a square partition as a function of L in the trivial phase for different B-values: $B = 0$ (red plus), $B = 0.04t$ (green cross), $B = 0.05t$ (blue star), $B = 0.07t$ (pink square) and $B = 0.09t$ (cyan diamond). (b) S_{sub} of a left/right partition in the topological phase in a for varying B-values: $B = 0.7t$ (red solid line), $B = 1.2t$ (green dashed line), $B = 1.4t$ (blue dashed line). The inset shows S_{sub} at the critical point $B = 0.5t$. The remaining parameters are fixed at $A = 0.25t$, $\mu = 0$, $\Delta_1 = 0.8t$, $\Delta_2 = 0.4t$, and $M = 0$.

For all cases studied in this paper, the leading behavior of the entanglement entropy is linear. The coefficient of the linear term is a non-universal constant denoted by α and dependent on the parameters of the Hamiltonian. In Fig. 2.4 we plot α for d-wave coupling for several B-values and different shapes of the partition. Directly at the critical point, the value of α jumps whereas in the topological phase, the change is rather small. Thus, we find that the very distinct signature of the phase transition described in the preceding section is due to the change in α. In addition, the dependence of α on the partition shape is rather small and does not change the qualitative behavior. Only for very large B-values, a slight difference can be seen.

As the sub-leading nature of these corrections makes it very hard to see them directly in the entanglement entropy, we look at the quantity[14].

$$S_{\text{sub}}(L) = LS_{L+1} - (L+1)S_L, \tag{2.4.1}$$

in which the leading linear term is eliminated. In the case of only a constant sub-leading term and in the limit of large L, $S_{\text{sub}} \propto$ const. For a logarithmic term, the behavior is $S_{\text{sub}} \propto \ln L$, whereas for a power law we have $S_{\text{sub}} \propto L^{\eta}$ for some exponent η. We will also study the dependence of the entanglement entropy on the geometry of the partition. To this end, we will look at a square partition, a cross shaped partition and an L-shaped partition (see the upper panel of Fig. 2.4).

In Fig. 2.5(a) we show results for S_{sub} of a square partition in the trivial phase for the d-wave case. It can clearly be seen that in the large L limit, S_{sub} converges to a constant value, which indicates a constant negative correction to the entanglement entropy. The constant (independent of L) it changes with the model parameters. In order to further understand the constant sub-leading term we study differently shaped partitions, such as a cross or an L-shaped partition (*c.f.* Fig 2.4). As suggested earlier[34], this constant is an effect of the corners, where the dimensions of the partition are of the order of the correlation length. Thus, we would expect to find a constant ratio of the constant of a cross (L-shaped) partition with the constant of a square partition to be 3 (1.5). And indeed, throughout the trivial phase (far away from the critical point), we find the ratios of the constants to be $c_{\text{cross}}/c_{\text{square}} \approx 3$, and $c_{\text{cross}}/c_{\text{L}} \approx 1.5$, as expected for a system with zero topological entanglement entropy, γ. The topological phase, unfortunately, is not reachable in this approach due to finite size effects.

Near a topological phase boundary one must exercise caution when analyzing the functional dependence of S_A on the system boundary size L. As the system nears the phase boundary the correlation length grows and so finite size effects become very large. For partitions such as those in Fig. 2.4, these finite size effects become important as we are technically limited to modest sized subsystems by the computational time and memory required to diagonalize the matrix G in subsystem A. Using a reasonable amount of memory limits our system size to a side length of $50 - 60$. Thus, when the correlation

length is large we do not have the ability to make our subsystem large enough to see the finite size effects subside. If one is not careful one could misinterpret the finite size effects in this region as some sort of non-trivial subleading contribution to S_A, such as $\log L$ or L^η.

To further illustrate our observation that any subleading terms to S_A for our system originate from corners and at the same time show just how important finite size effects become with an increased correlation length, we use a 'corner-less' partition, where subsystem A is a ring on our torus. If the torus dimensions are $L \times L_l$ where L_l is the longer dimension wrapped around the doughnut hole then our ring dimensions are $L \times l$ and we take $l = L/4$. The boundary of A is then varied by varying the entire system size. Besides having no corners this partition has the advantage that translation symmetry along the ring's azimuthal direction is conserved.

Our results for this type of subsystem are illustrated in Fig. 2.5(b). The first striking feature is that S_{sub} converges to zero for large L for all parameter choices. This leads to the conclusion that any subleading terms we have seen above must be a result of corners and subsequently that all subleading behavior beyond the area law for S_A is zero. This is consistent with the observation that the topological entanglement entropy for this system should always be zero.

The second purpose of Fig. 2.5(b) is to illustrate the importance of finite size effects when looking at area laws for spin-singlet superconductors. As the spin-orbit parameter B is increased S_{sub} acquires a damped oscillatory behavior as a function of L. For larger B the amplitude and decay length of these oscillations increase. The way in which L is changed for this partition requires changing both the boundary length of subsystem A *and* the total system size. Thus inherent in S_{sub} are both finite size effects from the fact that S_A depends on the total system size (for smaller lattice sizes, before the thermodynamic limit is reached) and finite size effects from non-area law behavior in S_A. The system

size required to overcome these effects increases with B. We see that even for $B = 0.7t$ a very large system size is required before finite size effects vanish. This system size is unreachable using partitions with corners, such as those in Fig. 2.4.

Another indication for finite size effects can be seen in the inset of Fig. 2.5(b), where we show the subleading correction to the entanglement entropy right at the critical point. It displays oscillatory behavior with a very large amplitude which increases with L. At this point, the correlation length diverges.

In summary, the current model shows that evaluating the exact subleading dependence of the entanglement entropy on L proves to be far from trivial. This is in contrast to previous work[13, 14] where such problems did not arise. Therefore, using such subleading terms as a way to evaluate the topology of a specific system (whether they exist or not) may be a prohibitively difficult task. That being said, analyzing the functional dependence on L is not a complete loss in this respect. Looking at the linear coefficient, α the above results suggest that it exhibits a discontinuity at the topological phase boundary. In Sect. 2.3 we found that the entanglement entropy is singular at the phase boundary, this could in principle come from a discontinuity in *any* term in S_A, regardless of the L dependence. The plot in Fig. 2.4 shows that this singularity is in fact coming from α. For a finite system with corners we essentially do not know the subleading dependence, whereas in the corner-less partition we find no subleading term at all. Regardless of these two differences we see the same pathological dependence of α on B at the phase boundary.

2.5 Edge States in the Entanglement Spectrum

Let us discuss another interesting characteristic of the corner-less partition introduced above. This partition introduces an artificial boundary into the system and therefore

we are able to probe boundary physics in a bulk model by looking at the entanglement spectrum of subsystem A[26, 27]. First let us think about a simple s-wave model (whose topological phase is a p-wave superconductor). If we were to introduce a boundary we would expect to see a zero energy edge mode when the Chern number is 1 and no edge mode when the Chern number is zero[12]. We can see this same physics in the *bulk* model by looking at the entanglement spectrum of the A subsystem. To illustrate this we have plotted the spectrum in the trivial phase and in the topological phase by properly changing parameters. Our results are presented in Fig. 2.6. We see quite unmistakably the development of a zero mode upon crossing into the topological region. This zero mode is localized on the boundary of subsystem A, as is shown in the inset of Fig. 2.6.

Finally we explore the edge physics of the *bulk* d-wave model (whose topological phase is a p- or f-wave superconductor). The solution of a d-wave system with an edge results in a spectrum which is slightly more complicated than the one above for the s-wave case[40]. From a topological standpoint one expects to see an even number (odd number) of zero energy states when the topology of the system is trivial (non-trivial). We have compared the low-lying states in our corner-less partition entanglement spectrum to those of a physical system with a boundary found, for example, in Reference [40]. We find consistency between the two with respect to the number of zero energy states, their position in k space as well as their low energy dispersion. A representative example of our results is shown in Fig. 2.7a. Our choice of parameters is such that the low lying states of this plot should be compared with those of Fig. 5II of Ref. [40].

Another interesting feature of the data in Figs. 2.6 and 2.7a is the nature of the eigenstate itself, both at and away from zero energy. At lower energies the wave functions are very localized on the edges of the system, with localization length increasing with energy. This state, however, does not become truly delocalized at any energy.

A second interesting feature of the eigenstates comes from studying the $E = 0$ states

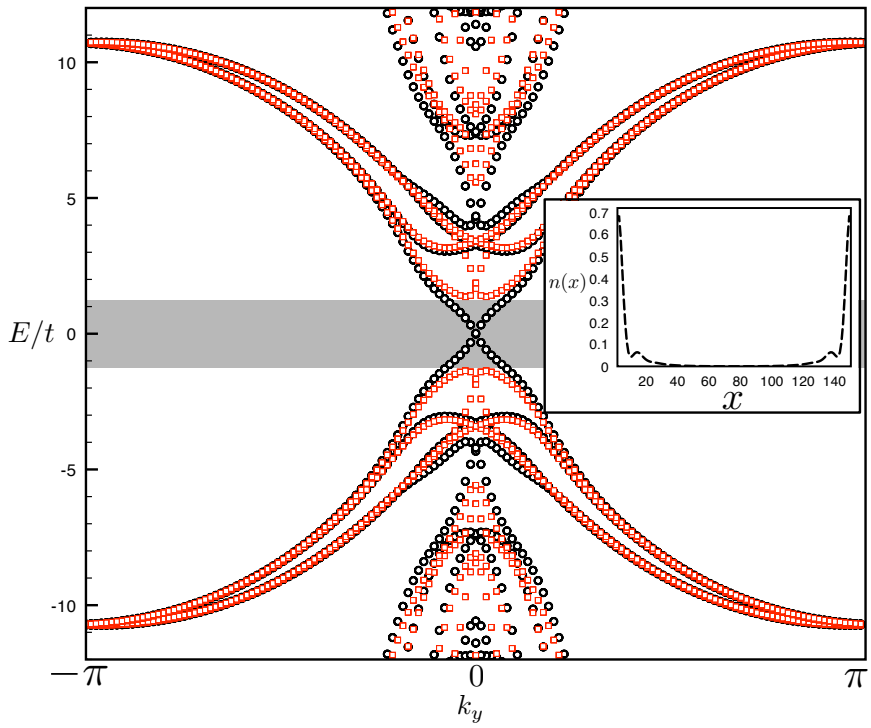

Figure 2.6: Entanglement spectrum of an s-wave superconductor. Both sets of data are for $\Delta_0 = 0.3t$, $A = 0.25t$, $\mu = -4t$. The red squares are for a system with a $M = 0.29t$ (trivial state) while the black circles are from a run with $M = 0.31t$ (topological state). The inset shows the density of the zero energy state in the $M = 0.31t$ system as a function of position. The boundaries of subsystem A are at $x = 0$ and $x = 150$ in this inset figure. The gap in the trivial spectrum is shaded to showcase the in-gap states of the topological spectrum.

and, in particular, looking for Majorana modes. We note that it is futile to look for a single Majorana state, as these modes must come in pairs in a finite system. We therefore look for pairs of Majorana states that are spatially separated and reside on opposite sides of the partition.

We notice that the entanglement spectrum exhibits particle hole symmetry, therefore if $|\psi\rangle$ is an eigenstate with energy E then $(\Lambda|\psi\rangle)^*$ is an eigenstate with energy $-E$, where $\Lambda = I \otimes \sigma_x$ with σ_x acting on Nambu space and I is the identity on a space of lattice sites and spin. This leads to the observation that at $E = 0$, $|\psi\rangle$ and $(\Lambda|\psi\rangle)^*$ are degenerate eigen states. All eigenstates at $E = 0$ are highly localized on the boundary of the system, an example of this is the state plotted in the inset of Fig. 2.6. Looking for Majorana zero energy states then becomes a task of looking for linear combinations of $|\psi\rangle$ and $(\Lambda|\psi\rangle)^*$ that give states localized at opposite ends of the system and obey the following condition: given two generic linear combinations

$$|\phi_{M,i}\rangle = \alpha_{1,i}|\psi\rangle + \alpha_{2,i}(\Lambda|\psi\rangle)^* = (u_i, v_i)^T, \tag{2.5.1}$$

where u_i and v_i are themselves vectors (each with dimension of one half the dimension of subsystem A) we require $u_i = v_i^*$.

As an example we have studied the gap closure in the d-wave spectrum in Fig. 2.7a at $k_y = 0$ in detail. Our numerical results give two states with very small energy (approximately $\pm 10^{-12}t$). Treating these two states as degenerate it is possible to form two linear combinations of them which we denote $|M_1\rangle$ and $|M_2\rangle$. We have plotted the density of these states in Figs. 2.7b and 2.7c. The average local electron density in these states per lattice site n is defined as

$$n_i(n) = |u_i^{\uparrow}(n)|^2 + |u_i^{\downarrow}(n)|^2 + |v_i^{\uparrow}(n)|^2 + |v_i^{\downarrow}(n)|^2, \tag{2.5.2}$$

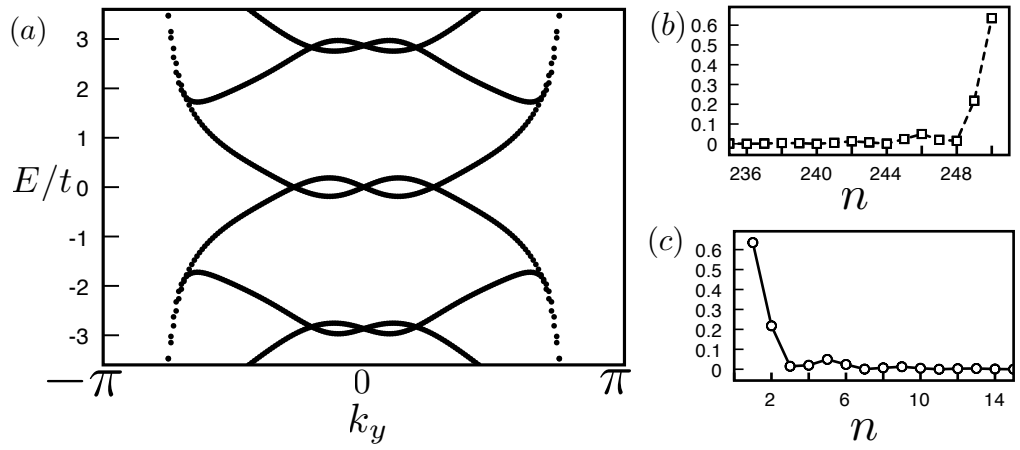

Figure 2.7: Entanglement spectrum and Majorana Modes in a d-wave superconductor. This data is for $\Delta_1 = 0.5t$,$\Delta_2 = 0.8t$, $A = 0.5t$, $\mu = -2.5t$ and $M = 2t$. (a) The entanglement spectrum; We note the three zero energy states and therefore the topological nature of the spectra. (b) and (c) The probability densities (see Eq. (2.5.2)) of the Majorana modes found through orthogonalization as a function of n, the number of lattice sites along the direction of the ring which makes up subsystem A.

where $u_i(n)$ is the n^{th} entry in the vector u_i and is itself a 2-component object (spin-up and spin-down) and the label $i = 1, 2$ denotes which state we are interested in. Note that this definition is also used in the inset of Fig. 2.6. The two combinations $|M_1\rangle$ and $|M_2\rangle$ are highly localized on the respective boundaries of subsystem A. Averaging the modulus of the difference between u_i and v_i^* of both of these states over every lattice site (and spin projection) in subsystem A gives a result which is of order 10^{-5}. Thus these two states are localized on different boundaries and (to a high numerical precision) satisfy the Majorana condition $u_i = v_i^*$.

2.6 Bulk entanglement spectrum and partition induced gap closure

Looking further into the entanglement spectrum we note that it is important to specify what kind of partition is used. For example, by partitioning a gapped system into a left and a right part, the low entanglement spectrum is similar to the excitation spectrum near a physical boundary [26, 27, 41], as seen above. In fact, states in the ES that are related to bulk degrees of freedom tend to lie very high in the spectrum of such a partition and barely contribute to the entanglement entropy.

Nonetheless, one may extract information about the bulk by defining 'extensive partitions', as defined by Hsieh and Fu in Ref. [28]. These partitions divide the system into two parts such that the boundary between the two extends throughout the whole system in every direction. Thus, the partition forms a superlattice. The periodicity of an extensive partition removes the edge modes from the ES and lead it to resemble a bulk spectrum.

An example for an extensive partition is show in Fig.(2.8) where one subsystem is a collection of square islands while the other is the remaining sea. Using these partitions we demonstrate that the ES may exhibit a topological phase transition as the partition is changed. Throughout the following discussion we fix the parameters of the model such that it represents a topological state. The only thing we change is the partition. As the result of this change a phase transition appears in the entanglement spectrum while the physical spectrum is always gapped and topological.

The tuning of partitions is done as follows. In the beginning system B consists of islands while A is the sea. In one extreme case the island size is shrunk to zero so that B is an empty set while A is the whole physical system. We then gradually enlarge the islands. At some point the islands corners touch. This is called the symmetric point.

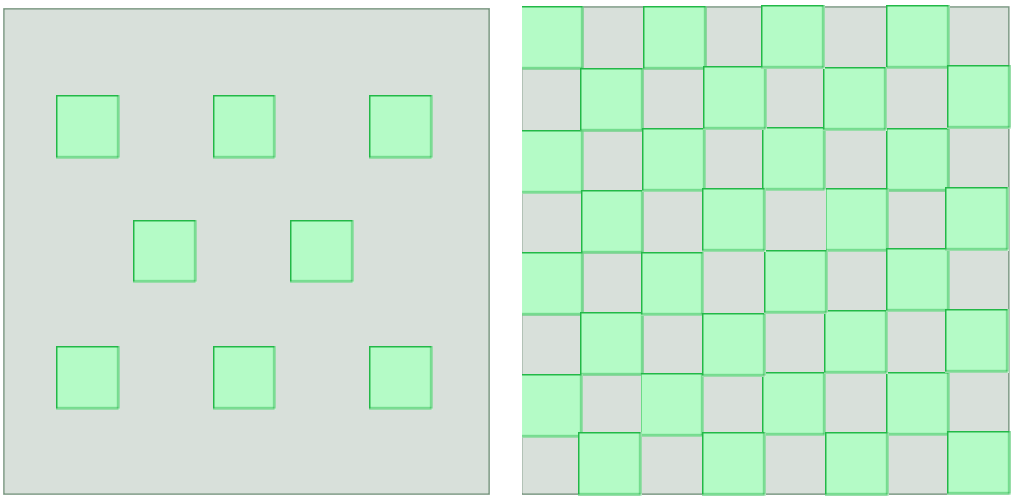

(a) (b)

Figure 2.8: (a) Schematic display of an asymmetric partition where the green squares are subsystem A and B its compliment. (b) Symmetric partition

When the islands grow further they overlap such that system B becomes the sea and system A breaks into isolated islands. In Ref. [28] Hsieh and Fu argue that in both extremes (A or B being the full system) subsystem A is gapped. However, when A includes the full system it is in a topological state (like the physical system) but when it is a collection of vanishingly small islands it is connected to the atomic limit (a trivial state). They conclude and demonstrate for a topological insulator that somewhere between these two limits the ES of subsystem A undergoes a topological phase transition which manifests itself as a gap closure.

Following Hsieh and Fu we apply the above idea to a topological superconductor. In Fig. 2.8a, we have sketched an extensive partition while the symmetric point is shown in Fig. 2.8b. In both cases, for a d-wave as well as an s-wave SC, the ES in the asymmetric cases are gapped, as can be seen for the case of a d-wave SC in Fig. 2.9 independent of the phase the system is in. Staying in a topologically non-trivial physical state, we can now induce a phase transition in the entanglement spectrum by varying the partition

across the symmetric point. As can be seen in Fig. 2.9, this indeed induces a gap closure.

Using the fact that the symmetric partition forms a superlattice, one can define k-vectors with respect to the superlattice and arrange the states in the ES with momentum. The ES can then be compared to the spectrum of an unpartitioned system, whose parameters are set to the critical point. The result can be seen in the lower part of Fig. 2.9. In Fig. 2.9(c) we can see the ES of the symmetric extensive partition qualitatively mirrors the physical spectrum of a critical, unpartitioned system (Fig. 2.9(d)). The parameters for the system in Fig. 2.9(c) where chosen to be in the topologically non-trivial phase. Thus, the symmetric partition realizes the critical system *without* changing the model parameters. The gap closes at the K-point, where the spectrum has a massless Dirac cone.

2.7 Conclusion

In this chapter we have studied several proposed signatures of topology in the entanglement entropy and spectrum of superconducting models with topological phases. Our systems of interest are spin-orbit coupled superconductors, motivated by recent progress in the search for Majorana fermions[29, 32]. We have compared our results with those obtained in previous work as well as evaluated the potential use of each of the methods for the study of more complicated (disordered/interacting) systems, where the topology is not known *a priori*[16].

We have analyzed the dependence of a bipartite partition on the circumference of the partition and found a dependence of the form $S(L) = \alpha L + \ldots$, where the first term is the celebrated area law and the dots stand for sub-leading terms. The coefficient α was found to have a sharp kink right at the phase transition such that it captures the transition very clearly. In the trivial phase, the only sub-leading term was found to be a constant

caused by corner effects. Meanwhile, the topological phase is not easily classified using a small finite system (due to finite-size effects) and we must defer to a corner-less system. In the corner-less partition the EE is given by the area law without any subleading terms. We conclude that any non-area law contributions in this finite system must be due to corners. As expected, throughout all phases the topological entanglement entropy, γ, was found to be zero. Therefore, calculating α for a corner-less partition and looking for singular behaviour may be of potential interest in more complicated systems.

Another signature of the topology of the system can be found by looking at the entanglement spectrum. Depending on the choice of partitioning one may obtain different topological properties of the entanglement Hamiltonian. A phase transition between the topological and the trivial phase can be seen as a gap closure in the entanglement spectrum. This is obtained by changing the extensive partitioning while leaving the physical parameters unchanged. This property is related to the non-trivial topology of the underlying state. Moreover, this finding implies that one has to apply special care when using the entanglement spectrum to extract information about the ground state of a physical system as it can undergo a phase transition while the physical system does not.

In addition to our goals stated in the introduction we would also like to emphasize the versatility of the approach outlined in this whole paper; it can be applied to all quadratic models with or without translational invariance where in the latter case the system sizes are limited by computational power. The use of various forms of partitions leads to a consistent picture of the different topological phases of a system, as shown for a spin-orbit coupled superconductor with $d + id$- and s-wave coupling.

2.8 Acknowledgements

We are grateful for useful discussions with R. Melko. Financial support for this work was provided by the NSERC and FQRNT (TPB, JB, SM) the Vanier Canada Graduate Scholarship and the Walter C. Sumner Memorial Fellowship (AF). The majority of the numerical calculations were performed using CLUMEQ/McGill HPC supercomputing resources.

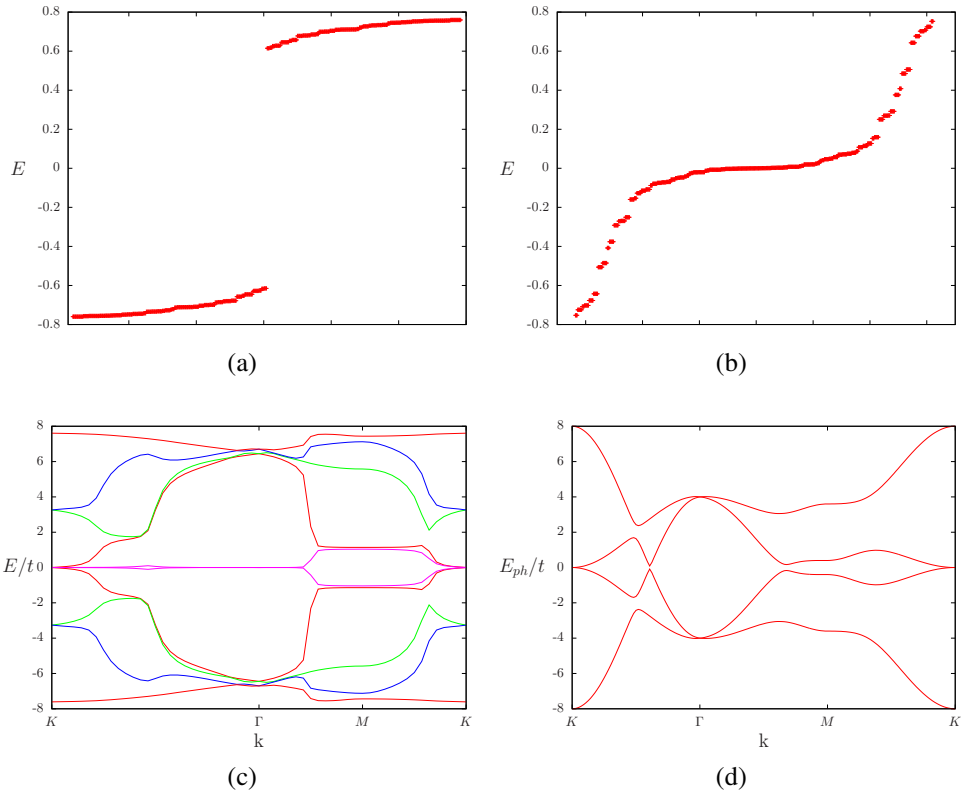

Figure 2.9: (a) Low energy part of the entanglement spectrum of the asymmetric partition in the topological phase of a d-wave superconductor with $B = 0.7t$, $M = 0.3t$, $\mu = 0$, $\Delta_1 = 0.8t$, $\Delta_2 = 0.4t$, and $A = 0.25t$. (b) Low energy part of the entanglement spectrum of the symmetric partition in the topological phase of a d-wave superconductor (with the same parameters as in (a)). (c) k-space spectrum for the symmetric partition of a 112 by 112 square lattice with the same parameters as in (a), where the k-vectors are defined with respect to the superlattice. (d) The physical spectrum of the system when its parameters are tuned to the critical point at $B = 0.5t$ and $M = 0$.

References

[1]D. J. Thouless, M. Kohmoto, M. P. Nightingale, and M. den Nijs, Phys. Rev. Lett. **49**, 405–408 (1982).

[2]C. L. Kane and E. J. Mele, Phys. Rev. Lett. **95**, 226801 (2005).

[3]C. L. Kane and E. J. Mele, Phys. Rev. Lett. **95**, 146802 (2005).

[4]D. Hsieh, D. Qian, L. Wray, Y. Xia, Y. S. Hor, R. J. Cava, and M. Z. Hasan, Nature **452**, 970–974 (2008).

[5]A. Y. Kitaev, Physics-Uspekhi **44**, 131 (2001).

[6]G. Volovik, English, Journal of Experimental and Theoretical Physics Letters **70**, 609–614 (1999).

[7]N. Read and D. Green, Phys. Rev. B **61**, 10267 (2000).

[8]A. P. Schnyder, S. Ryu, A. Furusaki, and A. W. W. Ludwig, Phys. Rev. B **78**, 195125 (2008).

[9]A. Kitaev, AIP Conf. Proc. **1134** (2009).

[10]S. Ryu, A. P. Schnyder, A. Furusaki, and A. W. W. Ludwig, New Journal of Physics **12**, 065010 (2010).

[11]G. E. Volovik and V. M. Yakovenko, Journal of Physics: Condensed Matter **1**, 5263 (1989).

[12]P. Ghosh, J. D. Sau, S. Tewari, and S. Das Sarma, Phys. Rev. B **82**, 184525 (2010).

[13]T. Oliveira, P. Ribeiro, and P. Scaramento, arXiv:1312.7782 (2013).

[14]L. Ding, N. Bray-Ali, R. Yu, and S. Haas, Physical Review Letters **100**, 215701 (2008).

[15]N. Bray-Ali, L. Ding, and S. Haas, Phys. Rev. B **80**, 180504 (2009).

[16]J. Borchmann, A. Farrell, T. Pereg-Barnea, and S. Matsuura, work in progress.

[17]A. Kitaev and J. Preskill, Phys. Rev. Lett. **96**, 110404 (2006).

[18]M. Levin and X.-G. Wen, Phys. Rev. Lett. **96**, 110405 (2006).

[19]M. A. Levin and X.-G. Wen, Phys. Rev. B **71**, 045110 (2005).

[20]S. V. Isakov, M. B. Hastings, and R. G. Melko, Nature Physics **7**, 772–775 (2011).

[21]A. M. Turner, A. Vishwanath edited by, M. Franz, and L. Molenkamp, in *Topological insulators*, Vol. 6, edited by M. Franz and L. Molenkamp (Elseveir, 2013) Chap. 11, p. 294.

[22]X. Chen, Z.-C. Gu, and X.-G. Wen, Physical Review B **82**, 155138 (2010).

[23]L. Y. Hung and S. Matsuura., work in progress.

[24]A. Belin, L.-Y. Hung, A. Maloney, S. Matsuura, R. C. Myers, et al., JHEP **1312**, 059 (2013).

[25]M. A. Metlitski and T. Grover, arXiv:1112.5166 (2011).

[26]H. Li and F. D. M. Haldane, Phys. Rev. Lett. **101**, 010504 (2008).

[27]X.-L. Qi, H. Katsura, and A. W. W. Ludwig, Phys. Rev. Lett. **108**, 196402 (2012).

[28]T. H. Hsieh and L. Fu, Phys. Rev. Lett. **113**, 106801 (2014).

[29]A. Farrell and T. Pereg-Barnea, Phys. Rev. B **87**, 214517 (2013).

[30]A. Farrell and T. Pereg-Barnea, Phys. Rev. B **89**, 035112 (2014).

[31]A. Farrell and T. Pereg-Barnea, *Unpublished* arXiv:1406.5552 (2014).

[32]J. D. Sau, R. M. Lutchyn, S. Tewari, and S. Das Sarma, Phys. Rev. Lett. **104**, 040502 (2010).

[33]J. Alicea, Phys. Rev. B **81**, 125318 (2010).

[34]S. Papanikolaou, K. S. Raman, and E. Fradkin, Physical Review B **76**, 224421 (2007).

[35]I. Peschel, J. Phys. A: Math. Gen. **36**, L205 (2003).

[36]I. Peschel and E. Viktor, J. Phys. A: Math. Theor. **42**, 504003 (2009).

[37]B. A. Bernevig, T. L. Hughes, and S. C. Zhang, Science **314**, 1757 (2006).

[38]J. Eisert, M. Cramer, and M. B. Plenio, Reviews of Modern Physics **82**, 277 (2010).

[39]M. M. Wolf, Phys. Rev. Lett. **96**, 010404 (2006).

[40]M. Sato, Y. Takahashi, and S. Fujimoto, Phys. Rev. B **82**, 134521 (2010).

[41]V. Alba, M. Haque, and A. M. Läuchli, Physical Review Letters **108**, 227201 (2012).

Preface to Chapter 3

In the previous chapter we showed numerically the fact that the entanglement entropy is able to detect the topological phase transition of a topological superconductor with either s- or d-wave coupling. Thus, it is a great tool to analyze a system when no easy way exists to calculate a topological invariant.

In order to extend and deepen the understanding of the connection between entanglement entropy and topology we now set out to get an analytical understanding of the entanglement entropy of a topological superconductor in the case of large Zeeman coupling. In this limit it is possible to project the system onto a single and effectively spinless band which is accessible to an analysis via the entanglement entropy.

3

Analytic Expression for the Entanglement Entropy of a 2D Topological Superconductor

Jan Borchmann[1] **and T. Pereg-Barnea**[1]

[1]Department of Physics and the Centre for Physics of Materials, McGill University, Montreal, Quebec, Canada H3A 2T8

This chapter has been submitted for publication in Physical Review B and is available as a preprint at arXiv:1607.07520.

Abstract

We study a model of two dimensional, topological superconductivity on a square lattice. The model contains hopping, spin orbit coupling and a time reversal symmetry breaking Zeeman term. This term, together with the chemical potential act as knobs that induce transitions between trivial and topological superconductivity. As previously found numerically, the transitions are seen in the entanglement entropy as cusps as a function of model parameters. In this work we study the entanglement entropy analytically by keeping only its most important components. Our study is based on the intuition that the number of Fermi surfaces in the system controls the topological invariant. With our approximate expression for the entanglement entropy we are able to extract the divergent entanglement entropy derivative close to the phase transition.

3.1 Introduction

Entanglement[1–3] is one of the most fascinating fundamental aspects of quantum systems that has no classical equivalent. Its most straight forward demonstration is through thought experiments on a system of few particles. Nevertheless, in recent years the degree of entanglement in large systems, measured, for example, through its entanglement entropy (EE), has become a standard tool in characterizing many body systems.[4, 5]. More specifically, the EE (or bipartite entanglement) is found by dividing the system into two parts, A and B. The reduced density matrix of subsystem A is defined as the result of tracing out the degrees of freedom associated with subsystem B in the density matrix. The logarithm of the reduced density matrix is then used to define the entanglement entropy. This, in general, leads to two categories of systems: entangled or separable. If the two subsystems are not entangled the density matrix of the full system contains two separate blocks corresponding to each of the subsystems. In this case the system is called separable and contains no entanglement. If this is not the case, the system is entangled.

The entanglement entropy has been shown to be a sensitive indicator of the topology in systems with intrinsic topological order[6] and recently it has also been studied in the context of symmetry protected topological states. It has been studied numerically in the clean limit[7–10] as well as in disordered systems[11–16], critical systems[17] and topological states[18–20]. Furthermore phase transitions in gapless states have been examined via the EE[21]. It should be noted, however, that in general the EE is not measurable except for certain, well designed situations[22–26]. It is usually used as a theoretical tool for characterizing model systems. In particular, the EE of symmetry protected topological states has been shown to exhibit a cusp as a function of model parameters when the parameters are tuned across a topological phase transition[10, 16].

This is the focus of the current manuscript.

Topological insulators and superconductors are normally characterized by topological invariants (a Chern number or Z_2-invariant, depending on the class). In non-interacting, clean systems these invariants can be easily computed using the Berry curvature while in interacting systems the calculation requires knowing the full Green's function and therefore the full spectrum. However, the full spectrum of large interacting systems is usually not accessible as most numerical methods are geared toward finding the ground state or a thermally averaged energy. In this respect the EE may prove useful as it can be defined using the ground state alone. This motivates our study of EE in symmetry protected topological systems.

There are several contributions to the entanglement entropy. For two-dimensional free-electron systems it has been shown that the entanglement entropy has the form

$$S = \alpha L - \gamma + \dots, \tag{3.1.1}$$

where L is the cross section of the partition used to calculate the entanglement entropy and $\dots$ stands for subleading terms. The fact that the entanglement entropy is proportional to the cross section of the partition instead of the volume is called the area law[27] where 'area' refers to the size of the boundary of the partition, in two dimensions this is a length. The term γ is called topological entanglement entropy. In systems with intrinsic topological order the entanglement entropy acquires this contribution, which equals the logarithm of the total quantum dimension of the system[28, 29]. This term is not applicable for symmetry protected states (SPTs) and is strictly zero in topological insulators and superconductors.

Additional terms can arise due to corners in the partition[7]. This can be understood as follows. In a finite partition, call it A, of size comparable to or smaller than the

correlation length, the entanglement entropy is enhanced due to correlations between states in the other partition, B, on different sides of the partition. In a large partition with corners, close to the corner of partition A there could be two states of subsystem B which are closer than the correlation length. The path connecting them goes through subsystem A and affects the entanglement entropy. This leads to additional terms in the entanglement entropy provide subleading corrections to the area law.

The reduced density matrix as well as the entanglement entropy are often difficult to evaluate analytically and are only accessible numerically. This is due to the fact that the calculation includes large matrices with non-generic features, making it hard to find general solutions. Additionally, partitioning the system breaks translation invariance in one or more directions, requiring a real space treatment. Moreover, the specific shape of the partition may also have contributions to the entanglement entropy. We therefore adopt a corner-less partition and avoid the effects of corners. The system is divided into left and right subsystems, A and B, respectively, and consequently preserves translation invariance in one spatial direction, this is depicted in Fig. 3.1.

The model we study is inspired by proposals for realizing two-dimensional topological superconductors in heterostructures[30–32]. In these heterostructures different layers provide the following essential ingredients needed to realize the topological superconductor. One or more layers provide non-trivial topology through spin-orbit coupling and a Zeeman field and an additional layer provides pairing through the proximity effect. The combination of these ingredients leads to chiral p-wave pairing in the valance band.

The paper is structured as follows: In section 3.2, starting out with a spin-orbit coupled s-wave superconductor, we derive the effective p-wave model in the large Zeeman limit. In section 3.3 we derive the expression for the entanglement entropy and analyze the correlation functions of the system. We conclude in section 3.4.

3.2 Model Hamiltonian

We describe our system via the Hamiltonian[31, 32]

$$H = T + H_{SC} + H_{SO}. \tag{3.2.1}$$

With the kinetic term,

$$T = -t \sum_{\langle i,j \rangle, \sigma} c^{\dagger}_{i,\sigma} c_{j,\sigma} - \mu \sum_{i} c^{\dagger}_{i,\sigma} c_{i,\sigma} \tag{3.2.2}$$

which includes nearest neighbour hopping on a square lattice as well as the chemical potential, μ. The second term introduces the pairing and reads,

$$H_{SC} = \sum_{\mathbf{k}} \left(\Delta_s c_{\mathbf{k},\uparrow} c_{-\mathbf{k},\downarrow} + \text{h.c.} \right), \tag{3.2.3}$$

where Δ_s is a superconducting s-wave order parameter. The last term includes the spin-orbit coupling and Zeeman field,

$$H_{SO} = \sum_{\mathbf{k}} \Psi^{\dagger}_{\mathbf{k}} \mathcal{H}_{\mathbf{k}} \Psi_{\mathbf{k}}, \tag{3.2.4}$$

with $\Psi_{\mathbf{k}} = (c_{\mathbf{k},\uparrow}, c_{\mathbf{k},\downarrow})^T$, $\mathcal{H}_{\mathbf{k}} = \mathbf{d}_{\mathbf{k}} \cdot \vec{\sigma}$, where the Pauli matrices $\vec{\sigma}$ act on the spin degree of freedom and $\mathbf{d}_{\mathbf{k}} = (A \sin k_x, A \sin k_y, M)$. Here A and M represent the Rashba spin-orbit coupling and Zeeman strength, respectively.

Starting from the tight binding model with Rashba spin-orbit coupling and no pairing, one finds that this coupling has the effect of aligning the spin of the electrons in the plane orthogonal to their momentum, leading to a Dirac cone at the gamma point. Introducing a finite Zeeman coupling gaps out the Dirac point. When the Zeeman mass M is larger than

the band width (determined by t and A) the two spin-orbit coupled bands do not overlap. The chemical potential then determines which band contributes to superconductivity. In this work we first focus on the regime $M > 4t + \mu$ where the Fermi level crosses only the lower band. We then discuss other possible cases.

In spin orbit coupled bands it is often convenient to work in a band basis, rather than a spin basis. We therefore introduce creation/annihilation operators for electrons in the upper and lower bands, $\Psi_\pm$ and $\Psi_\pm^\dagger$ and write

$$\Psi_{\mathbf{k}} = \phi_-(\mathbf{k})\Psi_-(\mathbf{k}) + \phi_+(\mathbf{k})\Psi_+(\mathbf{k}). \tag{3.2.5}$$

where $\phi_\pm(\mathbf{k})$ are scalar function representing the basis transformation. In the absence of pairing this transformation diagonalizes the kinetic part of the Hamiltonian, $H_0 = T + H_{SO}$ and leads to the following dispersion:

$$\epsilon_\pm = -2t(\cos k_x + \cos k_y) - \mu \pm \sqrt{A^2(\sin^2 k_x + \sin^2 k_y) + M^2}. \tag{3.2.6}$$

In this basis the pairing part of the Hamiltonian reads

$$\begin{aligned} H_{SC} = \sum_{\mathbf{k}} \Big[&\Delta_{+-}(\mathbf{k})\psi_+^\dagger(\mathbf{k})\psi_-^\dagger(-\mathbf{k}) + \Delta_{--}(\mathbf{k})\psi_-^\dagger(\mathbf{k})\psi_-^\dagger(-\mathbf{k}) \\ &+ \Delta_{++}(\mathbf{k})\psi_+^\dagger(\mathbf{k})\psi_+(-\mathbf{k}) + \text{h.c.}\Big]. \end{aligned} \tag{3.2.7}$$

Here, Δ_{+-} denotes an interband pairing function of s-wave symmetry; the other two terms are intraband pairings of p-wave symmetry. The intraband pairing is given by

$$\Delta_{--}(\mathbf{k}) = \frac{A\Delta_s(\sin k_y - i \sin k_x)}{2\sqrt{M^2 + A^2(\sin^2 k_x + \sin^2 k_y)}} = \Delta_{++}^*(\mathbf{k}) \tag{3.2.8}$$

As shown previously[10, 32, 33], this model exhibits a topological phase transition, when varying the parameters of the Hamiltonian. This can be seen by calculating the Chern number. More intuitively, one sees that a topological phase arises when there is only one spin-orbit coupled band which participates in the pairing. For fixed μ, A and Δ_s, one can show that the phase transition takes place at $M_\pm = \sqrt{\Delta_s^2 + (\pm 4 - \mu)^2}$ where the topological phase is for $M \in (M_-, M_+)$.

It can be shown that in the large Zeeman coupling regime and in the limit of small order parameter Δ_s, the interband Δ_{+-} pairing can be neglected. Thus, we can project out the upper band altogether and arrive at a chiral p-wave model:

$$H = \sum_{\mathbf{k}} \left[\epsilon_-(\mathbf{k}) \psi_-^\dagger \psi_- + \Delta_{--}(\mathbf{k}) \psi_-^\dagger(\mathbf{k}) \psi_-^\dagger(-\mathbf{k}) + \text{h.c.} \right], \tag{3.2.9}$$

where in this limit we may approximate

$$\Delta_{--}(\mathbf{k}) \approx \frac{A\Delta}{2|M|}(-i \sin k_x + \sin k_y). \tag{3.2.10}$$

We therefore drop the subscripts and arrive at an effective spinless model.

As mentioned above the system partitioning breaks translation invariance in the x-direction. We therefore introduce a mixed real- and momentum-space representation, $c_{k_x k_y} = \frac{1}{\sqrt{N}} \sum_{i_x} e^{-i r_i^x k_x} c_{i_x k_y}$. Our model can therefore be regarded as a collection of chains in the x direction with k_y controlling the chain parameters. The kinetic part of the Hamiltonian, $H_0 = T + H_{SO}$, is given by:

$$H_0 = \sum_{k_y} \left[\sum_{i_x} (-2t \cos k_y - \mu - |M|) c_{i_x k_y}^\dagger c_{i_x k_y} \; - t(c_{i_x k_y}^\dagger c_{i_x+1 k_y} + \text{h.c.}) \right], \tag{3.2.11}$$

where we have ignored the parameter A. The pairing is,

$$H_{SC} = \alpha \sum_{k_y, i_x} \left[-c^\dagger_{i_x+1,k_y} c^\dagger_{i_x,-k_y} + \sin k_y \, c^\dagger_{i_x,k_y} c^\dagger_{i_x,-k_y} + \text{h.c.} \right], \tag{3.2.12}$$

where $\alpha = \frac{A\Delta}{2M}$.

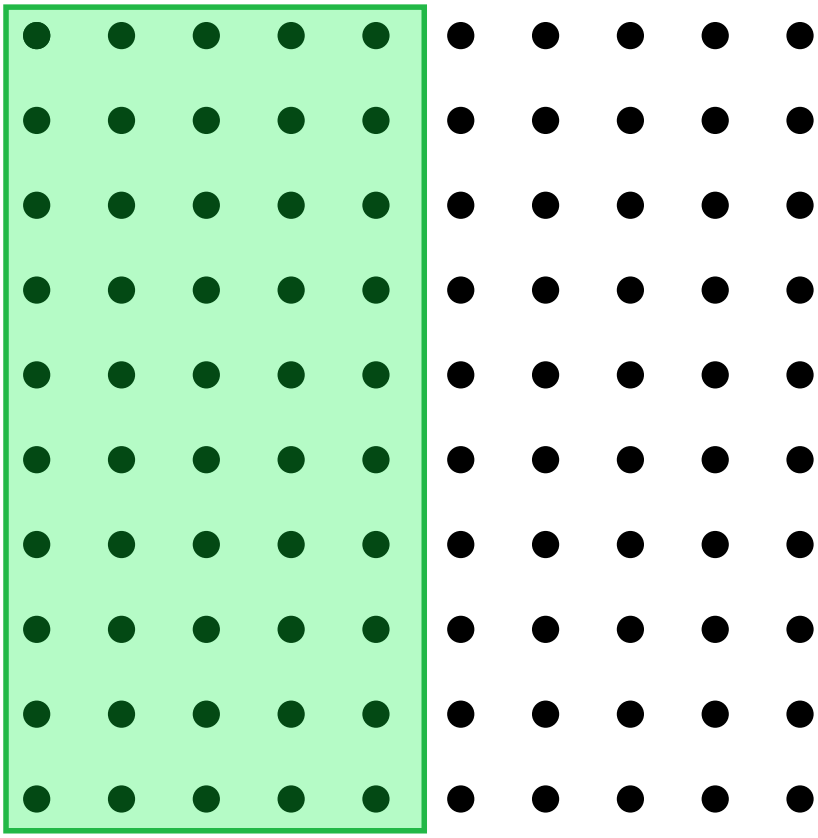

Figure 3.1: The cornerless partition with the left (right) part being subsystem A (B)

We therefore arrived at an effective spinless Hamiltonian with $M \gg \Delta, A, t$. As a consistency check, we examine the topological properties of the effective Hamiltonian compared to the full model. For the full spin-orbit coupled s-wave superconductor the large M phase transition from a topological phase to the trivial phase takes place at $M_+ = \sqrt{\Delta_s^2 + (4-\mu)^2}$. For the effective model the phase transition takes place at

$|-\mu-M|=4$. Thus, for small Δ_s our approximation will reproduce the behaviour of the full system reasonably well.

Due to translation symmetry in the y-direction it is possible to treat the Hamiltonian H as a sum of one-dimensional Hamiltonians with a parameter k_y. Thus, when partitioning the system, we can think of it as cutting each one-dimensional chain into two parts.

Another way to look at our current model is as follows. Each of the k_y-dependent chains in our system is a one dimensional Kitaev model[34]. Depending on its parameters the chain could be in the strong coupling trivial phase of the weak coupling topological phase. We find that our full system is topological as long as *some* of the chains are in the topological regime. Therefore, a phase transition from a trivial to a topological state occurs as soon as one chain becomes topological. Conversely, a phase transition from a topological to a trivial state occurs when all chains become trivial.

3.3 Calculation of the Entanglement Entropy

The first step in calculating the EE is to define the reduced density matrix ρ_a by integrating out the degrees of freedom associated with subsystem B. The reduced density matrix can then be used to define the entanglement Hamiltonian H_A via $\rho_A = \frac{e^{-H_A}}{Z_A}$, where Z_A is the partition function with respect to ρ_A. The eigenvalues of H_A are the entanglement spectrum. We denote these 'energies' by E_i, and use them to calculate the EE. Moreover, it has been shown[35, 36] that the entanglement spectrum is related to the eigenvalues of the correlation matrix G, which is defined as:

$$G = \begin{pmatrix} \langle c_i c_j^\dagger \rangle & \langle c_i c_j \rangle \\ \langle c_i^\dagger c_j^\dagger \rangle & \langle c_i^\dagger c_j \rangle \end{pmatrix}, \tag{3.3.1}$$

where each term is a matrix and the indices i and j run over the sites of subsystem A, the left part of our system of length L_x. The averages are calculated with respect to the ground state ψ. Denoting the eigenvalues of G by ζ_i, the entanglement spectrum levels are given by $E_i = \ln(\frac{\zeta_i}{1-\zeta_i})$, and therefore the EE can be written as

$$S = \sum_i \left[\zeta_i \log \zeta_i + (1-\zeta_i)\log(1-\zeta_i)\right] \tag{3.3.2}$$

The general structure of the eigenvalues of G consists of eigenvalues very close to 0 and 1 reflecting the fact that most bulk states are almost completely localized either in subsystem A or B and consequently do not contribute to the entanglement entropy. Intermediate values of ζ_i are caused by states that are entangled across the partition boundary and thus contribute the most to the EE.

Diagonalizing the matrix G was done numerically in Refs. [10, 16] and the Chern number of the same model was calculated explicitly in Ref. [33]. In these works it was seen that the Chern number changes whenever a Fermi surface appears or shrinks to a point and disappear. We therefore test this assumption by stripping the correlation matrix G of any ingredients which are unnecessary for detecting the phase transition. As we shall see shortly the crude approximations we make lead to an analytic expression for the EE which mimics the numerical one around the topological phase transition.

We begin by ignoring any off-diagonal (anomalous) terms in the correlation matrix due to $\alpha \ll 1$, and are therefore left with the usual particle-hole correlation. Of course, with the off-diagonal piece ignored, there is no need to keep the Nambu notation and one can focus on terms like $\langle c_\alpha c_\beta^\dagger \rangle$. We are therefore left with on-site and longer range correlations. For the regime we are investigating these long range correlations decay rapidly and thus it is reasonable to ignore higher order correlations. Hence, diagonalizing such a matrix is analogous to finding the eigenstates of a tight binding model in one

dimension with open boundary conditions[37]. However, we find that including only the on-site correlations and ignoring even nearest neighbour ones is easier and sufficient in our case. Of course, this is a good approximation only when the correlation length is not too long. A second assumption we make is that the system is large enough and the correlations die off quickly such that the correlation functions are position independent.

We are left with evaluating the onsite correlation for each k_y dependent chain, $\langle c_{i_x}(k_y)c_{i_x}(k_y)^\dagger\rangle$. Since we've ignored superconductivity this amounts to summing all of the occupation numbers $\langle c_k c_k^\dagger\rangle = 1 - n_k$ over the k_x momentum. At zero temperature, this amounts to the fraction of a 2π long line, along the k_x direction in the Brillouin zone, which contains (un)occupied states. In other words, if we draw the Fermi surface in the Brillouin zone and draw a line at a specific k_y, what fraction of this line is (outside)inside the Fermi surface. The answer is given by

$$\zeta_{k_y} = \langle c_{i_x}(k_y)c_{i_x}(k_y)^\dagger\rangle = \int \langle c_k c_k^\dagger\rangle dk_x = \begin{cases} \frac{1-2k_x^0(k_y)}{2\pi} & \text{particle} - \text{like Fermi surface} \\ \frac{2k_x^0(k_y)}{2\pi} & \text{hole} - \text{like Fermi surface} \end{cases} \tag{3.3.3}$$

where $k_x^0(k_y)$ is the x-component of the Fermi vector when the y-component is given by k_y. With our quadratic lattice dispersion we get:

$$k_x^0(k_y) = \arccos\left(\cos(k_y) - \frac{\mu + |M|}{2t}\right) \tag{3.3.4}$$

which is only defined for k_y values where there is a real solution (otherwise the contribution to the EE vanishes).

Putting all of the above together we are now able to write an expression for the

entanglement entropy as a sum of the EEs of each chain:

$$S = \sum_{k_y} S(k_y) \approx \frac{L_y}{2\pi} \int_0^{2\pi} dk_y \, S(k_y), \tag{3.3.5}$$

$$S(k_y) = \zeta_{k_y} \ln \zeta_{k_y} + (1 - \zeta_{k_y}) \ln(1 - \zeta_{k_y}). \tag{3.3.6}$$

The first line above clearly shows the area law as the EE explicitly depends on the length of the partition, L_y, which is the number of sites along the y direction. Together with the second line this expression is not yet a closed form but can be evaluated easily in simple cases.

Another simplification comes from the fact that transitions happen when Fermi surfaces appear and disappear. This amounts to the Fermi surface passing through the center or the corner of the Brillouin zone. We can therefore replace the sum over the k_y momentum by these points only and define $a = \frac{1}{\pi}\Re[\arccos(1 - \frac{\mu+|M|}{2t})]$ and $b = \frac{1}{\pi}\Re[\arccos(-1 - \frac{\mu+|M|}{2t})]$. This reduces the EE to:

$$\begin{aligned} S = &- L \left[(1-a) \left(a \ln a + (1-a) \ln(1-a) \right) \right. \\ &\left. + (1-b) \left(b \ln b + (1-b) \ln(1-b) \right) \right]. \end{aligned} \tag{3.3.7}$$

In this expression we have two contributions, the a-term from a possible phase transition at $k_y = \pi$ and the b-term from the Γ-point.

We can now compare the entanglement entropy calculated via Eq. (3.3.7) with the exact numerical value calculated by diagonalizing the full correlation matrix G. As can be seen in FIG. 3.2(a), the analytic formula underestimates the the entanglement entropy by a factor of $O(1)$, which is not surprising due to the way we approximated the correlation matrix. Nonetheless we can see that the formula captures very well the qualitative behaviour of the EE and in particular its behaviour near the phase transition.

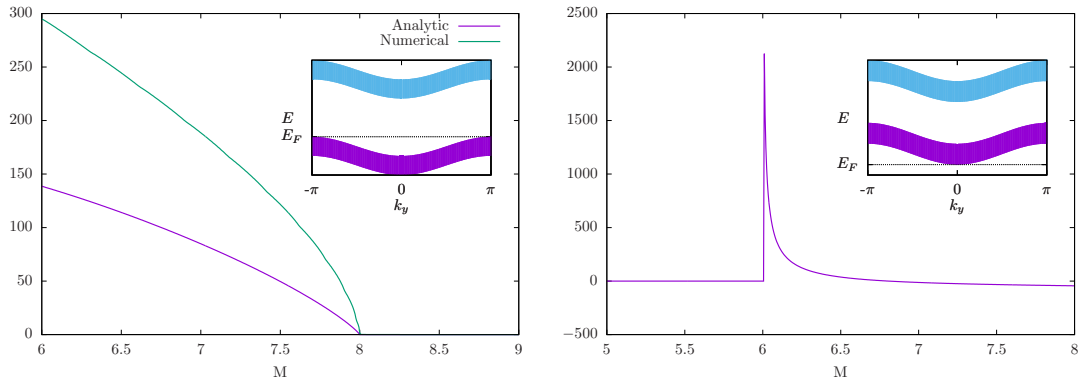

(a) (b)

Figure 3.2: (a) Entanglement entropy S for $\mu = -4t, A = 0.25t$ and $L_y = 400$ calculated numerically (green) as well as analytically (red). In the inset we show the position of the two bands with respect to the Fermi energy of the system without superconductivity. (b) Derivative of the entanglement entropy with respect to M for $\mu = -10t$. Again, the inset shows the band spectrum with respect to the Fermi energy. Note that the two panels represent different phase transitions with similar behaviour of the EE and its derivative

As we have shown previously[10, 16] the EE is indeed sensitive to the topological phase transitions. With the simple, approximate expression above we see that the topological phase transition is indeed governed by the appearance and disappearance of Fermi surfaces. At the transition the EE has a cusp and a singularity in its derivative:

$$\frac{\partial S}{\partial M} = \Re\left[\frac{L_y\left[2(1-a)\ln(1-a)+(2a-1)\ln(a)\right]}{\pi\sqrt{(|M|+\mu)(4t-|M|-\mu)}} + (a \to b)\right] \tag{3.3.8}$$

From this one can immediately see the change in behaviour at the topological phase transition, where the derivative jumps to zero as shown in FIG. 3.2(b).

With the intuition about the topological phase transitions from the approximate, single band model we can now relax our single band requirement slightly. Including the model's upper band has two consequences: (i) more Fermi surfaces and therefore more transitions may occur (ii) the singlet, inter-band pairing may not be negligible. Therefore, if we allow M to be smaller we might view more phase transitions. The

inter-band pairing is relevant when there is an over lap in energy between the two bands and in particular when the Fermi surface lies in this overlap. If we choose to ignore this inter-band pairing Δ_{+-} we may assign a 'topological' label to a trivial superconductor. However, as there is an even number of Fermi surfaces in this case, the system will have an even Chern number and an even number of Majorana branches on each edge. In this respect it is equivalent to a trivial superconductor. We therefore extend our analysis by relaxing the constraint over M while still ignoring interband pairing. The EE in this case is simply the sum of EE of the two bands $S = S_- + S_+$, while the upper band EE is given by Eq. (3.3.7) with $|M| \to -|M|$. Accordingly, the derivative receives a second term,

$$\frac{\partial S_+}{\partial M} = \Re \left[\frac{L_y \left[2(1-b)\ln(1-b) + (2b-1)\ln(b) \right]}{\pi \sqrt{(-|M|+\mu)(-4t+|M|-\mu)}} + (b \to a) \right] \tag{3.3.9}$$

Comparing the analytic and numeric evaluation of the entanglement entropy of our model we see that all phase transitions are captured as a singularity in $\partial S/\partial M$. The cusps in the EE occur in places where the Chern number of the system changes, i.e., a topological phase transition. However, there are some additional points where the EE exhibits a cusp but there is no phase transition. This happens when the parity of two time reversal invariant momentum (TRIM) points change simultaneously as a result of a lattice symmetry. If this symmetry is lifted, these points in parameter space will become phase transition points.

3.4 Conclusion

In this work we have analytically calculated the entanglement entropy for a spin-orbit coupled superconductor in the large Zeeman coupling limit. In this regime the spectrum

has a large gap, even without any pairing. Looking at the low energy part of the entanglement spectrum, one arrives at an effective p-wave superconductor. We are able to show explicitly that the entanglement entropy obeys the area law as expected. When comparing with the exact EE calculated through numerical diagonalization of the correlation matrix one finds that both indicate the same phase transitions. The derived formula is in qualitative agreement with the numerical evaluation.

The above calculation is enabled by crude approximations which relay on the pairing being small compared to the bandwidth and predominantly in the intra-band channel. The intuition behind these approximations comes from the understanding that the topology of the superconductor is inherited from the spin winding in each spin-orbit coupled bands and depends crucially on the number of Fermi surfaces.

3.5 Acknowledgments

The authors are grateful for useful discussions with A. Farrell and O. Motrunich. Financial support for this work has been provided by the Alexander McFee award (JB), NSERC and FQRNT (JB and TPB).

References

[1]A. Einstein, B. Podolsky, and N. Rosen, Phys. Rev. **47**, 777–780 (1935).

[2]E. Schrödinger, Mathematical Proceedings of the Cambridge Philosophical Society **31**, 555–563 (1935).

[3]E. Schrödinger, Mathematical Proceedings of the Cambridge Philosophical Society **32**, 446–452 (1936).

[4]L. Amico, R. Fazio, A. Osterloh, and V. Vedral, Rev. Mod. Phys. **80**, 517–576 (2008).

[5]R. Horodecki, P. Horodecki, M. Horodecki, and K. Horodecki, Rev. Mod. Phys. **81**, 865–942 (2009).

[6]J. Wildeboer, A. Seidel, and R. Melko, *unpublished* arXiv:1510.07682.

[7]T. P. Oliveira, P. Ribeiro, and P. D. Sacramento, Journal of Physics: Condensed Matter **26**, 425702 (2014).

[8]L. Ding, N. Bray-Ali, R. Yu, and S. Haas, Physical Review Letters **100**, 215701 (2008).

[9]N. Bray-Ali, L. Ding, and S. Haas, Phys. Rev. B **80**, 180504 (2009).

[10]J. Borchmann, A. Farrell, S. Matsuura, and T. Pereg-Barnea, Phys. Rev. B **90**, 235150 (2014).

[11]I. Mondragon-Shem, M. Khan, and T. L. Hughes, Phys. Rev. Lett. **110**, 046806 (2013).

[12]E. C. Andrade, M. Steudtner, and M. Vojta, Journal of Statistical Mechanics: Theory and Experiment **2014**, P07022 (2014).

[13]M. Pouranvari, K. Yang, and A. Seidel, Phys. Rev. B **91**, 075115 (2015).

[14]I. Mondragon-Shem and T. L. Hughes, Phys. Rev. B **90**, 104204 (2014).

[15]S. Vijay and L. Fu, Phys. Rev. B **91**, 220101 (2015).

[16]J. Borchmann, A. Farrell, and T. Pereg-Barnea, Phys. Rev. B **93**, 125133 (2016).

[17]T. H. Hsieh and L. Fu, Phys. Rev. Lett. **113**, 106801 (2014).

[18]E. Prodan, T. L. Hughes, and B. A. Bernevig, Phys. Rev. Lett. **105**, 115501 (2010).

[19]M. J. Gilbert, B. A. Bernevig, and T. L. Hughes, Phys. Rev. B **86**, 041401 (2012).

[20]B. J. Brown, S. D. Bartlett, A. C. Doherty, and S. D. Barrett, Phys. Rev. Lett. **111**, 220402 (2013).

[21]M. Rodney, H. F. Song, S.-S. Lee, K. Le Hur, and E. S. Sørensen, Phys. Rev. B **87**, 115132 (2013).

[22]I. Klich, G. Refael, and A. Silva, Phys. Rev. A **74**, 032306 (2006).

[23]J. Cardy, Phys. Rev. Lett. **106**, 150404 (2011).

[24]D. A. Abanin and E. Demler, Phys. Rev. Lett. **109**, 020504 (2012).

[25]T. J. Elliott, W. Kozlowski, S. F. Caballero-Benitez, and I. B. Mekhov, Phys. Rev. Lett. **114**, 113604 (2015).

[26]K. H. Thomas and C. Flindt, Phys. Rev. B **91**, 125406 (2015).

[27]J. Eisert, M. Cramer, and M. B. Plenio, Reviews of Modern Physics **82**, 277 (2010).

[28]A. Kitaev and J. Preskill, Phys. Rev. Lett. **96**, 110404 (2006).

[29]M. Levin and X.-G. Wen, Phys. Rev. Lett. **96**, 110405 (2006).

[30]L. Fu and C. L. Kane, Phys. Rev. Lett. **100**, 096407 (2008).

[31]J. D. Sau, R. M. Lutchyn, S. Tewari, and S. Das Sarma, Phys. Rev. Lett. **104**, 040502 (2010).

[32]J. Alicea, Phys. Rev. B **81**, 125318 (2010).

[33]A. Farrell and T. Pereg-Barnea, Phys. Rev. B **87**, 214517 (2013).

[34]A. Y. Kitaev, Physics-Uspekhi **44**, 131 (2001).

[35]I. Peschel, J. Phys. A: Math. Gen. **36**, L205 (2003).

[36]I. Peschel and E. Viktor, J. Phys. A: Math. Theor. **42**, 504003 (2009).

[37]R. Jullien, Canadian Journal of Physics **59**, 605–631 (1981).

Preface to Chapter 4

In the previous two chapters we established the fact that the entanglement entropy is able to detect the topological phase transition of a topological superconductor both analytically as well as numerically. Thus, it is a great tool to analyze a system when no easy way exists to calculate a topological invariant.

Building on these results, we extend our analysis of the topological superconductor from clean to disordered systems. To this end, we use the entanglement entropy and the results obtained in the previous chapter and complement the entanglement entropy treatment by analyzing the disordered system with the help of a real space Chern number as well as Gaussian disorder. Through this combination we are able to further analyze the predictive power of the entanglement entropy for disordered systems.

4

Anderson Topological Superconductor

Jan Borchmann[1], **Aaron Farrell**[1] **and T. Pereg-Barnea**[1]

[1]Department of Physics and the Centre for Physics of Materials, McGill University, Montreal, Quebec, Canada H3A 2T8

This chapter has been published in Physical Review B. Journal Reference: Physical Review B 93, 125133 (2016)

Abstract

In this paper we study the phase diagram of a disordered, spin-orbit coupled superconductor with s-wave or $d + id$-wave pairing symmetry in symmetry class D. We analyze the topological phase transitions by applying three different methods which include a disorder averaged entanglement entropy, a disorder averaged real-space Chern number, and an evaluation of the momentum space Chern number in a disorder averaged effective model. We find evidence for a disorder-induced topological state. While in the clean limit there is a single phase transition from a trivial phase with a Chern number $C = 4$ to a topological phase with $C = 1$, in the disordered system there is an intermediate phase with $C = 3$. The phase transition from the trivial $C = 4$ phase into the intermediate phase with $C = 3$ is seen in the real-space calculation of the Chern number. In spite of this, this phase transition is not detectable in the entanglement entropy. A second phase transition from the disorder induced $C = 3$ into the $C = 1$ phase is seen in all three quantities.

4.1 Introduction

Symmetry protected topological[1, 2] (SPT) systems include the quantum spin Hall state, topological insulators in two and three dimensions as well as topological superconductors. These systems, which are generally described by models with multiple phases, share the property that they experience distinct phases which cannot be smoothly transformed into each other while preserving a certain symmetry. In the topological phases, unique properties such as anomalous magneto-resistance and edge/surface states are the result of the topology. This topology is characterized by topological invariants which are the discrete expectation values of non-local operators. When parameters change across a phase transition the bulk gap closes, allowing the topological invariants to change their values. In particular, in a clean, non-interacting lattice system one can define the Berry curvature in momentum space and integrate it over a relevant area, such as the Brillouin zone. This integral yields the Chern number in broken time reversal symmetry states or a $\mathbb{Z}_2$-invariant in time reversal symmetric states.

While surface states are protected against weak perturbation by the topology, a strongly disordered system can be classified differently than its clean counterpart. It is therefore interesting to study SPT systems in the presence of disorder. An example for such a change in classification can be found in two dimensional[3–5] and three dimensional[6] Anderson topological insulators. In these systems the disorder can be thought of as renormalizing the parameters of the clean system and thus driving the system across topological phase boundaries. Moreover, while in the clean system the gap in the spectrum is crucial for preventing surface states from scattering into the bulk, in a disordered system, it is the mobility gap which plays this role.

From the point of view of identifying a topological phase transition, disorder poses a challenge. The introduction of disorder breaks translation invariance and consequently

the usual method of computing a topological invariant is invalid as it relies on the existence of a Brillouin zone. Alternative approaches, which do not rely on translation invariance, involve integrals over twisted boundary conditions[7, 8]. These integrals involve a large number of real-space Hamiltonian diagonalizations and consequently are very numerically costly. Efficient alternatives use the same principle and define the Chern numbers via traces[9] or commutators[10] of the coordinate and the projection operator. A particularly efficient method of calculating the Chern number has been proposed via the calculation of so-called coupling matrices[11].

Another method by which transitions between trivial and topological SPT states can be seen is through calculating the entanglement entropy[12–15] (EE). In a previous work we have shown that the EE of a clean system exhibits a cusp as a function of some model parameters at the point of a topological phase transition[16]. It should be made clear, however, that in SPTs the EE obeys the area law and it is this area-linear EE term which exhibits the cusp. This should be contrasted with the case of systems with intrinsic topology where a term referred to as 'topological entanglement entropy', γ, appears[17, 18]. This term does not appear in SPTs.

In this chapter we address the problem of disorder in a two dimensional topological superconductor (TSC). Our TSC is a fully gapped, spin orbit coupled, superconductor in which time reversal symmetry is broken by a Zeeman field. It is therefore in class D. We have studied this model previously in the clean limit and found topological phase transitions, which are evident from changes in the Chern number as well as the entanglement entropy cusps.

We introduce disorder and search for topological phase transitions. This is done in three ways (i) by evaluating the Chern number in real space, (ii) by calculating the entanglement entropy and looking for a cusp when varying parameters and (iii) by calculating a disorder averaged self energy and using it to define an effective clean

Hamiltonian for which the Chern number is easily found. While topological phase transitions are found in all three ways, there are significant differences. In particular, in the case of a d-wave superconductor with multiple gapped Fermi surfaces the real-space Chern number reveals a disorder induced topological phase. This phase appears in the real-space Chern number calculation as an intermediate phase where a single phase transition in the clean limit splits in to two transitions. When using the self-consistent Born approximation to account for the renormalization of parameters one sees a hint of this intermediate phase, although its extent in parameter space is considerably smaller. Surprisingly, the split into two phase transitions is not seen as a cusp in the entanglement entropy.

Our model is a two dimensional spin-orbit coupled topological superconductor on a square lattice with either $d + id$- or s-wave pairing symmetry. We look at these two pairing symmetries due to their fundamentally different response to nonmagnetic impurities. While in general, an s-wave[19] superconductor is robust against non-magnetic impurities, a d-wave superconductor is sensitive to this kind of scattering since its pairing amplitude depends on the momentum which is not conserved in the scattering process[20, 21]. This often leads to sub-gap states which, for a large number of impurities, can combine to form impurity bands. These sub-gap states can have a significant effect on the topology of the system[22] when such a band crosses the Fermi surface and thus creates zero energy states. It has been shown that this can lead to gapless topological phases[23] in disordered semiconducting nanowires.

It should be noted that although the pairing term is of even angular momentum, when projected on to the spin-orbit coupled bands it acquires an additional phase winding. This leads to effective p or f-wave pairing in the bands[24, 25]. The question of whether the (clean) system is topological is therefore related to the number of spin-orbit coupled bands present. If there is an odd number of bands this will lead to an odd Chern number.

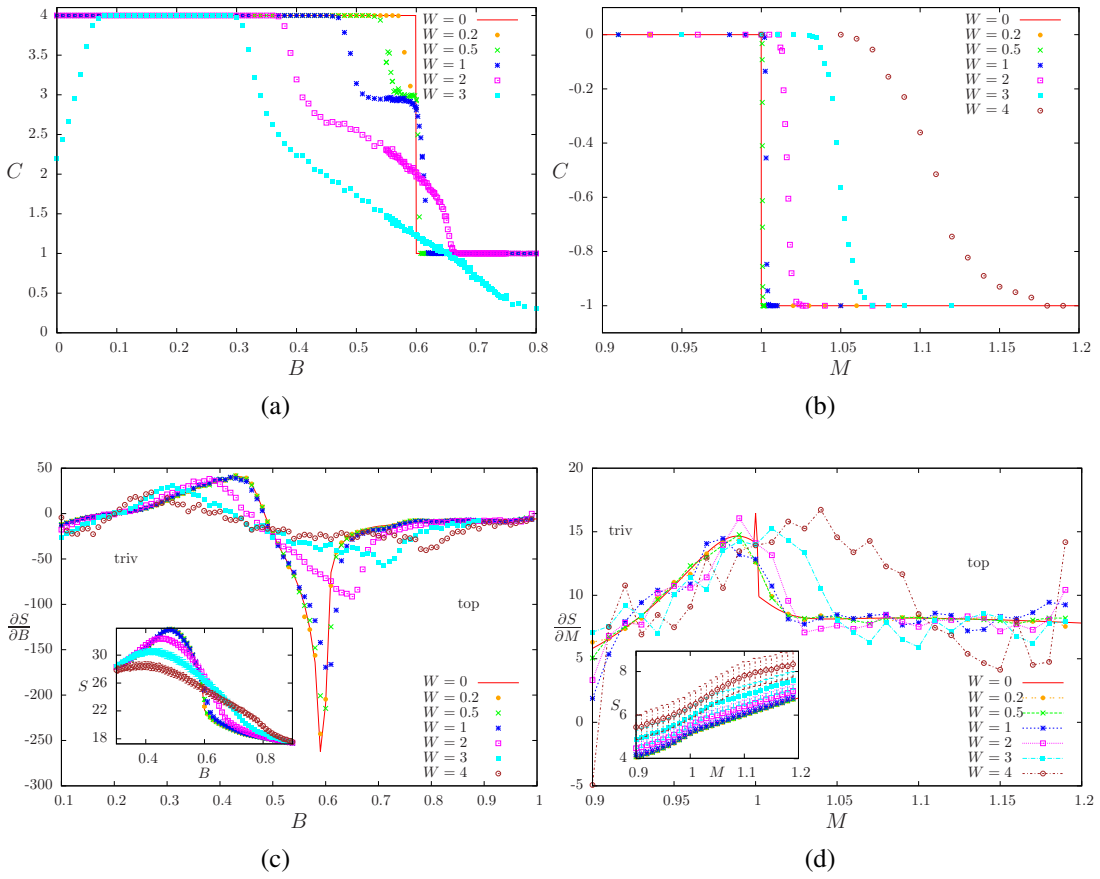

Figure 4.1: (a) Chern number C for $d + id$-wave coupling $\Delta_1 = 0.8t, \Delta_2 = 0.4t, M = 0.8t, \mu = 0$ and $A = 0.25t$, (b) Chern number C for s-wave coupling $\Delta_s = 1t, B = 0, \mu = -4t$ and $A = 0.25t$. Derivative of the Entanglement entropy for (c) $d + id$-wave coupling , (d) s-wave coupling. The insets show the entanglement entropy.

4.2 Model

We use the Hamiltonian[26] $H = H_K + H_{SO} + H_{SC} + H_D$, where the kinetic energy part is given by nearest neighbour hopping,

$$H_K = -t \sum_{\langle i,j \rangle, \sigma} \left(c^\dagger_{i\sigma} c_{j\sigma} + c^\dagger_{j\sigma} c_{i\sigma} \right). \tag{4.2.1}$$

The spin-orbit part is given by,

$$H_{SO} = \sum_{\mathbf{k}} \psi_{\mathbf{k}}^{\dagger} \left(\sigma \cdot \mathbf{d}_{\mathbf{k}}\right) \psi_{\mathbf{k}}, \tag{4.2.2}$$

with $\psi_{\mathbf{k}} = (c_{\mathbf{k}\uparrow}, c_{\mathbf{k}\downarrow})^T$, $\sigma = (\sigma_x, \sigma_y, \sigma_z)$ and,

$$\mathbf{d}_{\mathbf{k}} = \left(A \sin k_x, A \sin k_y, 2B(\cos k_x + \cos k_y - 2) + M\right). \tag{4.2.3}$$

Here, A, B denote the strength of the Rashba and Dresselhaus spin-orbit coupling[24], respectively, and M is the strength of the Zeeman term. The superconducting part is

$$H_{SC} = \sum_{\mathbf{k}} \left(\Delta_{\mathbf{k}} c_{\mathbf{k},\uparrow} c_{-\mathbf{k},\downarrow} + \text{h.c.}\right), \tag{4.2.4}$$

where we look at two different pairing functions. For the fully gapped $d + id$-wave we have $\Delta_{\mathbf{k}} = \Delta_1(\cos(k_x) - \cos(k_y)) + i\Delta_2 \sin(k_x)\sin(k_y)$ and for the s-wave pairing $\Delta_{\mathbf{k}} = \Delta_s$.

We include the effects of disorder by adding an on site, random potential term[27],

$$H_D = -\sum_i w_i c_i^{\dagger} c_i, \tag{4.2.5}$$

where $w_i \in [-\frac{W}{2}, \frac{W}{2}]$ is a random number with a uniform distribution in the interval. W is the overall disorder strength and a specific realization of the disorder is given by the set $\{w_i\}$. When choosing and characterizing the size of the disorder strength, we are guided by the typical energy scales of the system, the gap and the bandwidth. Comparing with the gap, c.f. Fig. 1c in Ref. [16], one can see that $W = 1$ is larger than the gap. $W = 3$ is of the order of the bandwidth. We compute disorder averaged quantities, namely, the Chern number and EE, by calculating the quantity for a specific realization

of the disorder and then averaging over a large number (≥ 400) of realizations $\{w_i\}$. The number of disorder realizations is taken such that the average quantities and standard deviations have saturated and do not change upon including more disorder realizations. We find that for low disorder strength 400 realizations are sufficient while for higher disorder we need larger samples.

4.3 Real Space Chern number

In order to analyze the behaviour of the system in the presence of disorder, one can calculate the topological invariant of the ground state by using a real space formula[10, 11]. This formula is derived by writing the wavefunctions on the torus and constructing their Fourier components with twisted boundary conditions in both directions. The Chern number can then be evaluated as the response to the twists. By using the twisted boundary conditions, the ground states induces the structure of a $U(1)$-fibre bundle over the torus of phase twists, whose Chern number gives the topological invariant.

In order to make a connection with our previous work[16], we look at the phase transition in the d-wave system which, in the clean limit, takes place at the value $B_c = 0.6t$ (and the other parameters are set to $M = 0.8t, \mu = 0$ and $A = 0.25t$). In the clean system, for $B < B_c$ the superconductor is trivial[1] with $C = 4$ and for $B > B_c$ it is a topological superconductor with a Chern number of $C = 1$.

In Fig. 4.1(a) we show the result of the Chern number calculation in real space for the clean system and for various disorder strengths in the d-wave system. Looking at the graph, the first striking feature is that compared with the clean system, the disordered system has an additional phase. While in the clean limit one finds a single, sharp

[1] We call this phase trivial due to the fact that the even number of edge modes will hybridize due to the broken time reversal symmetry.

transition between a trivial $C = 4$ phase on the left to a $C = 1$ phase on the right, for disorder strength of $W = 0.5t$ to $1t$ the transition splits to two and an intermediate phase with $C = 3$ appears. The transition from $C = 4$ to $C = 3$ appears before (for lower B) the clean limit transition and does not cause a cusp in the entanglement entropy. The second transition from $C = 3$ to $C = 1$ occurs after the clean limit transition and shows as a cusp in the EE. At the $C = 3$ plateau a large majority of the disordered systems, ranging from 65% up to 95 %, have a Chern number of 3, while a small fraction have $C = 4$ or $C = 2$ moving the average slightly away from 3. At the two other phases, with $C = 4, 1$ all of the systems in the average have exactly the same Chern number.

For $W = 3t$ the disorder averaged Chern number does not saturate to 1 anymore. This is caused by the fact that the system becomes gapless[23] and the Chern number is no longer well defined. Specifically, this behaviour implies the vanishing of the mobility gap as localized states do not influence the Chern number. Consequently, the real space Chern number is not a good indicator of the topology of the system in this regime. Furthermore, for low B the Chern number starts deviating from its clean value due to the fact that it is sensitive to another phase transition taking place at $B = -0.4t$.

One can speculate on the origin of the new disorder-induced topological phase. First, a Chern number of 4 is an indication that multiple Fermi surfaces contribute to the topological invariant. Therefore it is possible that the change in Chern number does not occur simultaneously in all Fermi surfaces. Moreover, one can imagine that localized states may reduce the life time of the bands and change the overall topological nature. Indeed, a disordered induced topological phase is not seen in the s-wave superconductor where potential disorder is not expected to cause localization. We should also note that a similar effect of localization was encountered in the case of symmetry class DIII[22].

The disorder averaged Chern number in the s-wave system is shown in Fig. 4.1(b). In general, for this pairing symmetry, the system only exhibits phase transitions with

$\Delta C = \pm 1$. We choose to focus on one of these transitions, which is controlled by the model parameter M. Note that due to the momentum independence of the s-wave order parameter, no pair breaking is induced by the disorder and no sub-gap states appear. We therefore expect the effect of disorder in this superconductor to be different from that of the $d + id$ case.

4.4 Disorder Averaged Entanglement Entropy

Several authors have studied the entanglement properties of disordered systems[28–32]. In particular, the relation between the level spacing in the entanglement spectrum and the topology was explored in Refs. [10, 33]. In the current work we focus on the entanglement entropy of disordered SPTs and investigate whether a topological phase transition is seen as a kink in the EE as was seen in the clean limit[16]. We follow the above kink as the strength of the disorder is increased.

The disorder averaged entanglement entropy can be defined as the disorder averaged von Neumann entropy of the reduced density matrix, $\overline{S_A} = -\overline{\mathrm{Tr}\,(\rho_A \ln \rho_A)}$, where A is a partition of the original system. For our calculations we define A as a 12x12 square in a 40x40 lattice with periodic boundary conditions, where the remaining degrees of freedom of the original system were traced out. We calculate the reduced density matrix via the two-point correlation function[34]. The size of the system is limited by the fact that these calculations are done in real space as well as the need for statistical averaging.

In Fig. 4.1(c) we show the entanglement entropy of the d-wave model (inset) and the derivative of the entropy with respect to the parameter B. While the EE exhibits a cusp at the phase transition, it is easier to recognize the transition in the derivative. The figure shows that the clean system's sharp transition at B_c is shifting to higher values of B when the disorder is increased and becomes less sharp at the same time. For strong

disorder the transition is completely washed out. One can see that the derivative of the EE displays only a single kink, coinciding with the position of the phase transition from $C = 3$ to $C = 1$, while any signature of the first phase transition is completely absent.

In Fig. 4.1(d) the EE for the s-wave system is presented as a function of the parameter M. We note that in this system the transition is not as pronounced as in the d-wave case even in the clean limit. When following the transition we see that once the disorder is applied the transition moves to higher values of M and its position coincides well with the one obtained via the real space Chern number. It also becomes less sharp and washes out completely for strong disorder.

4.5 Disorder Averaged Self Energy

Another approach that is often used to deal with disordered systems is using the Gaussian disorder properties to define an averaged Green's function and restore the translation symmetry. In other words, the disorder induces a self energy which renormalizes the model parameters. In the case of an Anderson topological insulator it was shown that a Gaussian disorder leads to a change in the Zeeman field parameter (M in our model) which in turn leads to a change in topology[3]. We therefore apply the same method here.

To this end, we use the variance of the random potential above and write, $\overline{V(q)V(q')} = \frac{W^2}{12\mathcal{V}}\delta_{q+q',0}$, where $\mathcal{V} = L^2$ is the volume of our ($L \times L$ lattice) system. With this, the self energy in the self-consistent Born approximation (SCBA) reads

$$\Sigma(\omega) = \frac{W^2}{12\mathcal{V}} \sum_q (\sigma_0 \otimes \tau_z) \cdot (\omega - H(q) - \Sigma(\omega) + i\eta)^{-1} \cdot (\sigma_0 \otimes \tau_z) \tag{4.5.1}$$

where τ_i are Pauli matrices acting on the particle and hole degree of freedom and σ_i denote

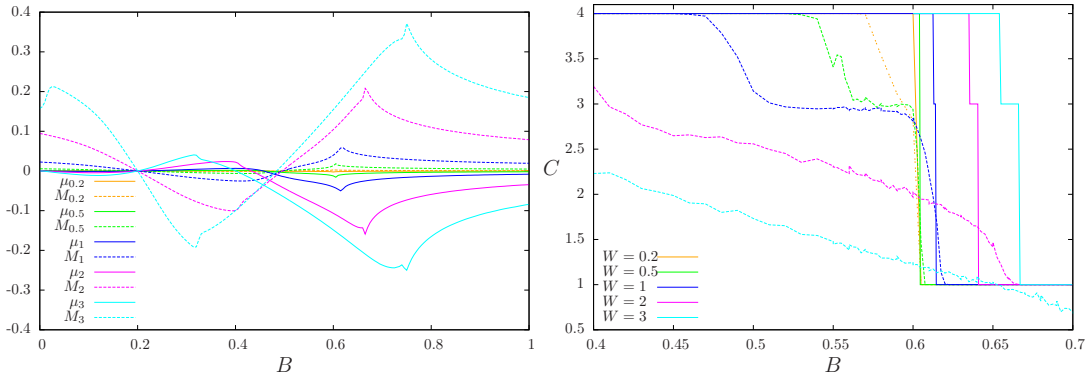

(a) (b)

Figure 4.2: (a) Renormalization of the chemical potential (solid line) and Zeeman coupling (dashed line) for varying disorder strengths for $d + id$-wave and (b) Chern number C_{ren} (solid line) calculated from the renormalized parameters and through a real space formula C_{RS} (dashed line).

the spin. The self consistent summation includes all non-crossing diagrams. Focusing on the static limit we can think of $\Sigma = \mathrm{Re}\left(\Sigma(\omega = 0)\right)$ as renormalizing the parameters of the Hamiltonian. Consequently we can define the effective Hamiltonian[35, 36] $H_\Sigma = H + \Sigma$ in which one can easily calculate the relevant Chern number in momentum space.[37, 38] Due to the parameter renormalization the topological phase transition moves in parameter space with respect to the clean system. The fact that Σ is independent of momentum, limits the possible quantities that can be renormalized to M, μ as well as Δ_s in the s-wave pairing case. Thus, most generally this can be written as[20, 21]

$$\Sigma = -\mu_R \left(\sigma_0 \otimes \tau_z\right) + M_R \left(\sigma_z \otimes \tau_z\right) - i\Delta_{sR} \left(\sigma_y \otimes \tau_x\right), \tag{4.5.2}$$

where the renormalized parameters are $M_R = M + M_\Sigma$, $\mu_R = \mu + \mu_\Sigma$ and $\Delta_{sR} = \Delta_s + \Delta_\Sigma$. Looking at the results in Fig. 4.2 we see that there is good agreement between this method and the real-space Chern number calculation as well as the EE cusp with respect to the transition between the $C = 3$ and the $C = 1$ phases. On the other hand,

the first transition, from $C = 4$ to $C = 3$ which appears in the real-space Chern number, appears in the self energy at a higher B value and is completely absent from the EE. Overall, the intermediate $C = 3$ phase appears in the self-energy calculation but its range is smaller by about an order of magnitude than its range in the real-space Chern number calculation. We note that the chemical potential renormalization is the most important one when it comes to creating the $C = 3$ phase. We speculate that the SCBA, which neglects cross diagrams, might not be sufficient when estimating the $C = 3$ phase range.

4.6 Conclusion

In this work we have presented evidence for a disorder induced topological phase for certain ranges of disorder strength. The calculation of the real space Chern number as well a disorder averaged self-energy predict the appearance of a new, $C = 3$-phase between the $C = 4$ and the $C = 1$ phase which exist in the clean system. However, the range of parameters over which the disorder induced phase occurs is much smaller in the self-energy method compared with the real-space Chern number. This is perhaps a result of the self-consistent Born approximation which neglects cross diagrams. In addition, we find that the disorder averaged entanglement entropy is a useful indicator in some topological phase transitions but not others. In particular, in the d-wave case, it has a cusp in the transition between the new, disorder induced topological phase and the $C = 1$ phase but does not have a cusp at the transition between the $C = 4$ and $C = 3$ phase.

4.7 Acknowledgements

The authors are grateful for useful discussions with M. Franz, L. Fu and B. Seradjeh. Financial support for this work was provided by the NSERC and FQRNT (TPB, JB) and

the Vanier Canada Graduate Scholarship (AF). The majority of the numerical calculations were performed using CLUMEQ/McGill HPC supercomputing resources.

References

[1]Z.-C. Gu and X.-G. Wen, Phys. Rev. B **80**, 155131 (2009).

[2]F. Pollmann, E. Berg, A. M. Turner, and M. Oshikawa, Phys. Rev. B **85**, 075125 (2012).

[3]C. W. Groth, M. Wimmer, A. R. Akhmerov, J. Tworzydło, and C. W. J. Beenakker, Phys. Rev. Lett. **103**, 196805 (2009).

[4]H. Jiang, L. Wang, Q.-f. Sun, and X. C. Xie, Phys. Rev. B **80**, 165316 (2009).

[5]J. Li, R.-L. Chu, J. K. Jain, and S.-Q. Shen, Phys. Rev. Lett. **102**, 136806 (2009).

[6]H.-M. Guo, G. Rosenberg, G. Refael, and M. Franz, Phys. Rev. Lett. **105**, 216601 (2010).

[7]Q. Niu, D. J. Thouless, and Y.-S. Wu, Phys. Rev. B **31**, 3372–3377 (1985).

[8]K. Yang and R. N. Bhatt, Phys. Rev. Lett. **76**, 1316–1319 (1996).

[9]A. Kitaev, Annals of Physics **321**, 2–111 (2006).

[10]E. Prodan, T. L. Hughes, and B. A. Bernevig, Phys. Rev. Lett. **105**, 115501 (2010).

[11]Y.-F. Zhang *et. al.*, Chin. Phys. B **22**, 117312 (2013).

[12]W. Li, A. Weichselbaum, and J. v. Delft, Phys. Rev. B **88**, 245121 (2013).

[13]T. J. Osborne and M. A. Nielsen, Phys. Rev. A **66**, 032110 (2002).

[14]J. C. Xavier and F. C. Alcaraz, Phys. Rev. B **84**, 094410 (2011).

[15]E. Canovi, E. Ercolessi, P. Naldesi, L. Taddia, and D. Vodola, Phys. Rev. B **89**, 104303 (2014).

[16]J. Borchmann, A. Farrell, S. Matsuura, and T. Pereg-Barnea, Phys. Rev. B **90**, 235150 (2014).

[17]A. Kitaev and J. Preskill, Phys. Rev. Lett. **96**, 110404 (2006).

[18]M. Levin and X.-G. Wen, Phys. Rev. Lett. **96**, 110405 (2006).

[19]P. Anderson, J. Phys. Chem. Solids **11**, 26–30 (1959).

[20]H. Alloul, J. Bobroff, M. Gabay, and P. J. Hirschfeld, Rev. Mod. Phys. **81**, 45–108 (2009).

[21]A. V. Balatsky, I. Vekhter, and J.-X. Zhu, Rev. Mod. Phys. **78**, 373–433 (2006).

[22]L. Kimme, T. Hyart, and B. Rosenow, Phys. Rev. B **91**, 220501 (2015).

[23]J. D. Sau and S. Das Sarma, Phys. Rev. B **88**, 064506 (2013).

[24]J. D. Sau, R. M. Lutchyn, S. Tewari, and S. Das Sarma, Phys. Rev. Lett. **104**, 040502 (2010).

[25]J. Alicea, Phys. Rev. B **81**, 125318 (2010).

[26]A. Farrell and T. Pereg-Barnea, Phys. Rev. B **87**, 214517 (2013).

[27]P. W. Anderson, Phys. Rev. **109**, 1492–1505 (1958).

[28]I. Mondragon-Shem, M. Khan, and T. L. Hughes, Phys. Rev. Lett. **110**, 046806 (2013).

[29]E. C. Andrade, M. Steudtner, and M. Vojta, Journal of Statistical Mechanics: Theory and Experiment **2014**, P07022 (2014).

[30]M. Pouranvari, K. Yang, and A. Seidel, Phys. Rev. B **91**, 075115 (2015).

[31]I. Mondragon-Shem and T. L. Hughes, Phys. Rev. B **90**, 104204 (2014).

[32]S. Vijay and L. Fu, Phys. Rev. B **91**, 220101 (2015).

[33]M. J. Gilbert, B. A. Bernevig, and T. L. Hughes, Phys. Rev. B **86**, 041401 (2012).

[34]I. Peschel, J. Phys. A: Math. Gen. **36**, L205 (2003).

[35]Z. Wang and B. Yan, Journal of Physics: Condensed Matter **25**, 155601 (2013).

[36]W. Witczak-Krempa, M. Knap, and D. Abanin, Phys. Rev. Lett. **113**, 136402 (2014).

[37]P. Ghosh, J. D. Sau, S. Tewari, and S. Das Sarma, Phys. Rev. B **82**, 184525 (2010).

[38]A. Farrell and T. Pereg-Barnea, Phys. Rev. B **89**, 035112 (2014).

Preface to Chapter 5

In the last chapter we have investigated the effect of disorder on the topological properties of a topological superconductor with various pairing symmetries. We have seen how the random disorder potential has a small effect on the topology of the ground state to a surprisingly large disorder strength when compared to the hopping amplitude in the model. However, this is only one example of a perturbation that can affect a physical system. In this chapter we will investigate the effect of an applied magnetic field on a gapless topological state, a Weyl semimetal. We will analyze the topological properties when exposed to the external field and investigate specifically the topological surface states via an effective surface theory.

5

Quantum oscillations in Weyl semimetals via an effective surface theory

Jan Borchmann[1] **and T. Pereg-Barnea**[1]

[1]Department of Physics and the Centre for Physics of Materials, McGill University, Montreal, Quebec, Canada H3A 2T8

This chapter will be submitted for publication in Physical Review B.

Abstract

In this work we construct an effective surface theory for a Weyl semimetal in a slab geometry. We apply this theory to the problem of Fermi-arc-induced quantum oscillations. Through this approach we are able to probe the system beyond the semiclassical limit and investigate the effect of small arc lengths on the phase offset of the quantum oscillations. In addition we find no contribution from the Berry curvature to the phase offset. Our findings are confirmed numerically via an exact diagonalization of a full lattice model for a Weyl semimetal slab. These serve as verification and extension of the semiclassical theory.

5.1 Introduction

Topological semimetals[1, 2] have recently attracted a lot of attention and have become the focus of intense research. In general, these materials are characterized by band crossings between the conduction and valence band which cannot be removed by perturbations preserving certain symmetries such as translational invariance. In this work we specifically deal with Weyl semimetals[3–7] (WSM), a class of materials which possesses an even number of Weyl nodes separated in momentum space. This requires either inversion or time-reversal symmetry breaking in order for the bands to be non-degenerate. Generically, these kinds of band touching points require three dimensions without the presence of special symmetries such as lattice symmetries. Around the nodes, the Bloch states acquire a topological character which in turn stabilizes this phase against perturbations. Recently, evidence for the discovery of WSMs has been presented in TaAs[8–13] as well as TaNb[14], NbP[15] and TaP[16] and another kind of WSM, called type-II has been predicted in WTe_2[17] as well as $MoTe_2$[18, 19]. Additionally, there several theoretical predictions of Weyl semimetals have been made including in $SrSi_2$[20], $HgCr_2Se_4$[21], $TaIrTe_4$[22] and $Mo_xW_{1-x}Te_2$[23].

Since the low energy states are found around the Weyl nodes, we may expand our Hamiltonian in their vicinity. We then arrive at the Weyl Hamiltonian in three dimensions,

$$H_W = \hbar \mathbf{v} \cdot \mathbf{k}\, \sigma_0 + \sum_{i,j=x,y,z} \hbar h_{ij} k_i \sigma_j, \tag{5.1.1}$$

where i, j run over spatial directions and σ_n are Pauli matrices. The second term in the Hamiltonian is the usual Weyl Hamiltonian in which the matrix h determines the spinor direction. The first term is unique to condensed matter systems, as it breaks Lorentz invariance, and unlike the second it is proportional to the unit matrix. Therefore it does

not influence the spin direction but has an effect on the spectrum. It tilts the Weyl cone in the energy-momentum space and we therefore refer to it as 'tilt'. The importance of the tilt relative to the Weyl term provides a distinction between two Weyl point types. In type I Weyl points the tilt is not dominant when compared to the Weyl part of the Hamiltonian. In type II Weyl points the tilt is dominant such that there is non-zero density of states at zero energy. The two types differ in their thermodynamic responses[17].

Each of the Weyl nodes acts as a monopole of the Berry curvature and its charge is $\chi 2\pi$, where chirality, $\chi = \det(h_{ij})$ at each node. As a consequence, WSMs experience a chiral anomaly[24–26] which leads to a variety of transport effects[27] such as negative magnetoresistance[24], the anomalous quantum Hall effect[4, 21, 28–32], the chiral magnetic effect[32–34] as well as coupling between magnons and plasmons[15].

When introducing a surface in the otherwise infinite system, one can still define the momenta in directions parallel to the surface while using real space coordinates along the direction perpendicular to it. The surface momenta define the surface Brillouin zone (SBZ). The zero energy surface states form Fermi arcs[3] in the SBZ. The arcs begin and end at the projections of the Weyl nodes on the SBZ. Recently, the Fermi arcs have been observed[35] through photoemission measurement in TaAs. It has been proposed[36, 37] that the Fermi arcs in the surface Brillouin zone can give rise to quantum oscillations in a WSM with a slab geometry when a magnetic field B is applied perpendicular to the surface of the slab. Semi-classically, one can imagine that the two Fermi arcs on each surface connect though the bulk by the chiral bulk Landau level. This way a closed magnetic orbit is formed and quantum oscillations appear. The equation for the Landau levels reads

$$\epsilon_n = \frac{\pi v}{\frac{k_a}{eB} + N_y} \left(n + \gamma\right), \tag{5.1.2}$$

where γ is a phase offset determined by the quantum details of the theory. Here, k_a is the length of the Fermi arc in the SBZ, N_y is the thickness of the slab and v is the Fermi velocity. One can identify two contributions to the period of the oscillations. The first is given by the propagation of the electrons along the arc. The second contribution is due to the fact that the electrons have to tunnel through the bulk to reach the arc on the other side of the slab. This specific dependence of the quantum oscillations on the geometry of the sample can lead to interference effects and experimental evidence for this kind of quantum oscillations has been presented[38] by using triangular samples of the Dirac semimetal Cd_3As_2.

This rest of this paper is structured as follows: In part 5.2 we introduce the generic model we are using and develop the effective surface theory. In section 5.3 we apply a magnetic field to the system and use the effective surface theory to investigate the surface quantum oscillations and investigate the short arc length regime. In part 5.4 we compare our findings to a full numerical treatment of the WSM slab. Our conclusions are summarized in 5.5.

5.2 Effective Surface Theory

5.2.1 The model

In order to study the surface theory of a WSM, we start with a spinless, two-orbital tight binding model[39],

$$H_{3D} = t_s \left(\sin k_x \sigma_x + \sin k_y \sigma_y + \sin k_z \sigma_z\right) + \left(m + t'(2 - \cos k_x - \cos k_y)\right) \sigma_z, \tag{5.2.1}$$

where time-reversal symmetry $H(\mathbf{k}) = \sigma_y H^*(-\mathbf{k})\sigma_y$ is broken by the second term. The choice to break time reversal symmetry is not limiting as one could devise a similar, time reversal invariant Hamiltonian. Our choice here is made in order to work with smaller matrices of dimension two. The energy eigenvalues are,

$$E_\pm = \pm \left[t_s^2 \left(\sin^2 k_x + \sin^2 k_y \right) + \left(t_s \sin k_z + m + t'(2 - \cos k_x - \cos k_y) \right)^2 \right]^{\frac{1}{2}} . \tag{5.2.2}$$

Throughout the remainder of the paper, we will set $t' = 1$ and measure the other quantities with respect to t'. From Eq. (5.2.2), one can see that the model has different phases depending on the parameters m and t_s. When keeping t_s fixed and varying m, one finds the following phases:

- For $t_s < m$ the model is gapped and trivial.
- At $m = t_s$ a gap closure appears at $\mathbf{k} = (0, 0, -\pi/2)$ and for $-t_s < m < t_s$ the gap closure splits into two Weyl nodes which recombine for $m = -t_s$ at $\mathbf{k} = (0, 0, \pi/2)$.
- For $-3t_s < m < -t_s$ there are two pairs of Weyl nodes which appear for $m = -t_s$ at $\mathbf{k} = (\pi, 0, -\pi/2)$ and $\mathbf{k} = (0, \pi, -\pi/2)$. The Weyl points recombine again at $m = -3t_s$ at $\mathbf{k} = (\pi, 0, \pi/2)$ and $\mathbf{k} = (0, \pi, \pi/2)$.
- For $-5t_s < m < -3t_s$ there are Weyl nodes which start at $\mathbf{k} = (\pi, \pi, -\pi/2)$ and recombine at $\mathbf{k} = (\pi, \pi, \pi/2)$.
- For $m < -5t_s$ the model is again gapped and trivial.

We choose to work in one of the Weyl semimetal regimes above, where $|m| < t_s$. The analysis can be extended easily to other regimes.

In order to look for the surface states, we will introduce a slab geometry with (010) surfaces such that k_x and k_z remain good quantum numbers. This amounts to performing a Fourier transform from $c_{\mathbf{k}}$-operators to $c_{i_y,\vec{k}}$-operators, where $\vec{k} = (k_x, k_z)$. Here, the variable y is a discrete layer index ranging between 1 and N_y, where N_y is the number of layers. In this new basis, the matrix element of the interlayer terms can be written as,

$$R = \begin{pmatrix} -\frac{1}{2} & -\frac{t_s}{2} \\ \frac{t_s}{2} & \frac{1}{2} \end{pmatrix}. \tag{5.2.3}$$

For further reference we define the layer Hamiltonian (the remaining diagonal term with respect to the y-layers) as,

$$\begin{aligned} H_0 &= t_s \sin k_x \sigma_x + (m + 2 - \cos k_x + t_s \sin k_z)\, \sigma_z \\ &\equiv g_1(\vec{k})\sigma_x + g_3(\vec{k})\sigma_z. \end{aligned} \tag{5.2.4}$$

Due to the broken time reversal symmetry, this model exhibits multiple phases with pairs of Weyl points. When placed in a slab geometry, the surface Brillouin zone includes Fermi arc states between the projections of the Weyl points onto the surface Brillouin zone. In our lattice model and in the regime we choose to work in, the arc connecting the two Weyl nodes is a straight line along the k_z-axis of length $k_a = 2\arccos(\frac{m}{t_s})$.

5.2.2 Effective surface propagator

In order to derive an exact effective surface theory, we treat the surface degrees of freedom independently from the bulk degrees of freedom. Note that the two surfaces in layer 1 and layer N_y are treated as one subsystem while all other layers are the bulk subsystem. In this non-interacting model it is possible to integrate out the bulk degrees of freedom and arrive at an effective theory for the surface field. Following Marchand

and Franz[40], we derive an expression for the surface Green's function,

$$G_{\text{eff}}(i\omega_n) = \left[G_s^{-1}(i\omega_n) - T^\dagger G_b(i\omega_n) T\right]^{-1}, \tag{5.2.5}$$

where $G_{b,s}(i\omega_n) = -(i\omega_n - H_{b,s})^{-1}$ are the bulk and surface Greens functions, respectively. The matrix T is the coupling between the surface and the bulk. The propagator in Eq. 5.2.5 is not directly related to an effective Hamiltonian since it contains a finite lifetime due the decay of surface states into the bulk.

5.2.3 Numeric evaluation of the effective Green's function in a slab geometry

For the slab geometry the Hamiltonian can be written as a N_y-by-N_y block matrix,

$$H_{3D} = \begin{pmatrix} H_0 & R & 0 & 0 & \dots & 0 & 0 \\ R^\dagger & H_0 & R & 0 & \dots & 0 & 0 \\ 0 & R^\dagger & H_0 & R & \dots & 0 & 0 \\ \vdots & \vdots & \vdots & \vdots & \ddots & \vdots & \vdots \\ 0 & 0 & 0 & 0 & \dots & R^\dagger & H_0 \end{pmatrix}, \tag{5.2.6}$$

where H_0 and R were defined above. Dividing the three dimensional Hamiltonian matrix into block one can read the parts of Eq. (5.2.5),

$$H_b = \begin{pmatrix} H_0 & R & 0 & 0 & \dots & 0 & 0 \\ R^\dagger & H_0 & R & 0 & \dots & 0 & 0 \\ 0 & R^\dagger & H_0 & R & \dots & 0 & 0 \\ \vdots & \vdots & \vdots & \vdots & \ddots & \vdots & \vdots \\ 0 & 0 & 0 & 0 & \dots & R^\dagger & H_0 \end{pmatrix}, \tag{5.2.7}$$

$$T = \begin{pmatrix} R^\dagger & 0 \\ 0 & 0 \\ \vdots & \vdots \\ 0 & 0 \\ 0 & R \end{pmatrix}, \tag{5.2.8}$$

and $H_s = \text{diag}(H_0, H_0)$. For realistic system sizes, the matrices involved are very large and the solution to Eq. (5.2.5) is only accessible numerically. In Fig. 5.1 we show the spectral function $A = -\frac{1}{\pi}\Im[\text{Tr}(G_{\text{eff}})]$ for various values of m as well as for different cuts in the surface Brillouin zone. In Fig 5.1 (a) one can see the spectral function for the combined top and bottom surfaces for fixed k_z. One can see the top and bottom surface Fermi arcs, respectively, with opposite chiralities. Further, we show the spectral function for fixed k_x for different values of m, where one can clearly see the structure of the Fermi arcs in the surface Brillouin zone.

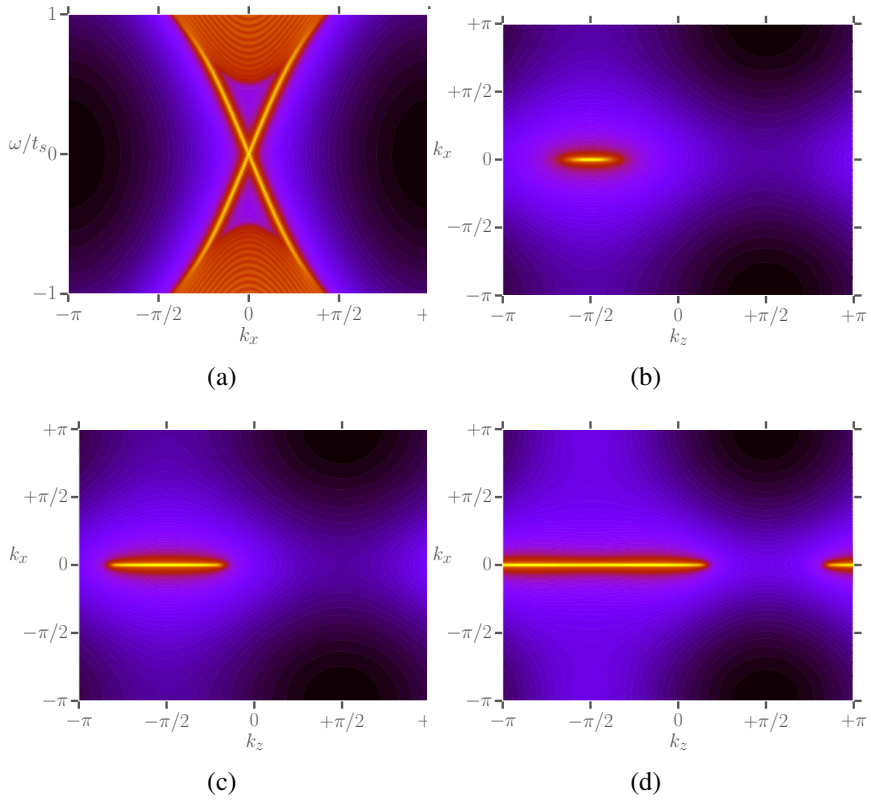

Figure 5.1: (a) Surface spectral function as a function of energy ω and momentum k_x for fixed momentum $k_z = -\frac{\pi}{2}$ and $\eta = 0.01$ in the middle of the Fermi surface arc. (b) Surface spectral function as a function of momentum at energy $\omega = 0$ and $\eta = 0.01$ for varying arc lengths $m = 0.9$, (c) $m = 0.5$, (d) $m = -0.5$

5.2.4 Analytic Green's function at low energy, semi-infinite sample

In order to advance analytically, we change the geometry of the system to a semi-infinite slab in y-direction by taking $N_y \to \infty$. Thus, we set $H_s = H_0$ and T is changed accordingly. Looking at a semi-infinite slab has the advantage that the system with one layer removed is identical to the system before removing the layer. We therefore envision that we're looking for the effective Green's function for the nth layer when the effective Green's function for the $(n+1)$th is known. Since the system is unchanged by removing a single layer, the two Green's functions above are identical. This leads to the following

recursive equation:

$$G_{\text{eff}} = \left[G_0^{-1}(i\omega_n) - T^\dagger G_{\text{eff}} T\right]^{-1}, \tag{5.2.9}$$

where we have defined $G_0 = (i\omega_n - H_0)^{-1}$. The equation for G_{eff} is now simply an equation for a 2-by-2 matrix and can be solved analytically. Nonetheless, for general parameter values, the solution is still quite complicated and not insightful. It is therefore useful to simplify it by transforming the system via the unitary transformation $U = \exp\left(-i\frac{\pi}{4}\sigma_y\right)$, which corresponds to a rotation around the y-axis in orbital space. In addition, we set $t_s = t'$ in order to simplify the result. This leads to,

$$\begin{aligned} \tilde{R} \to R &= \begin{pmatrix} 0 & 0 \\ t_s & 0 \end{pmatrix}, \\ \tilde{H}_0 \to H_0 &= g_1(\mathbf{k})\sigma_z - g_3(\mathbf{k})\sigma_x. \end{aligned} \tag{5.2.10}$$

The solution for the Green's function reads,

$$G(i\omega_n, k) = \begin{pmatrix} G_{\text{eff}}^{(2)} & G_{\text{eff}}^{(3)} \\ G_{\text{eff}}^{(3)} & G_{\text{eff}}^{(1)} \end{pmatrix}, \tag{5.2.11}$$

where

$$\begin{aligned} G_{\text{eff}}^{(1)} &= \frac{1}{2t_s^2(i\omega + g_1)}\left(t_s^2 + (i\omega)^2 - g_1^2 - g_3^2 \pm \sqrt{p}\right), \\ G_{\text{eff}}^{(2)} &= \frac{i\omega + g_1}{2t_s^2 g_3^2}\left(-t_s^2 + (i\omega)^2 - g_1^2 - g_3^2 \pm \sqrt{p}\right), \\ G_{\text{eff}}^{(3)} &= \frac{1}{2t_s^2 g_3}\left(t_s^2 - (i\omega)^2 + g_1^2 + g_3^2 \mp \sqrt{p}\right). \end{aligned} \tag{5.2.12}$$

and

$$p = -4t_s^2(i\omega - g_1)(i\omega + g_1) + (-t_s^2 - (i\omega)^2 + g_1^2 + g_3^2)^2. \tag{5.2.13}$$

Analytic continuation then yields the retarded/advanced Green's functions. The low energy part of the spectrum is governed by the poles of G_1 at $\omega = -g_1(\mathbf{k})$.

As mentioned in the introduction, one of the most prominent aspects of Weyl semimetals are the surface Fermi arcs. In order to see that the effective surface theory correctly predicts their existence, we can approximate the retarded Green's function $G^{(1)}_{\text{eff}}$ for low energies around the poles as

$$G^{(1)}_{\text{eff,ret}} = \frac{t_s^2 - g_3^2 + |t_s^2 - g_3^2|}{2t_s^2\left(\omega + \sin k_x + i\eta\right)}, \tag{5.2.14}$$

which leads to the spectral function

$$A^{(1)}_{\text{eff}} = \begin{cases} (1 - \frac{g_3^2}{t_s^2})\delta(\omega + \sin k_x) & \text{for } \frac{g_3^2}{t_s^2} < 1 \\ 0 & \text{else} \end{cases} \tag{5.2.15}$$

At low energy the weight of the spectral function is concentrated in a limited part of the Brillouin zone. The zero energy states are obtained from the Green's function by setting $\omega = 0$ and therefore $k_x = 0$. For $t_s = 1$, this gives the condition:

$$|m + 1 + \sin k_z| < 1 \quad \Rightarrow \quad m + \sin k_z < 0. \tag{5.2.16}$$

The left hand side of the above expression is zero right at the Weyl nodes and is negative between them. Therefore the zero energy states reside on a straight line between the two Weyl point projections on the surface momentum space.

5.3 Application of a magnetic field

In a varying magnetic field metals produce quantum oscillations. In two dimensions these are the consequence of changing the Landau level spacing such that the Fermi level traverses the Landau levels. In three dimensions the Landau levels are broadened by the dispersion along the dimension parallel to the field. Alternatively in a semiclassical picture electrons form closed orbits in the plane perpendicular to the field. In momentum space these orbits trace the cross section of the Fermi surface perpendicular to the field.

In a Weyl semimetal one can expect both three dimensional bulk quantum oscillations as well as surface quantum oscillations. The bulk quantum oscillations are most apparent at high magnetic fields. The surface quantum oscillations appear due to semiclassical orbits along a path composed of Fermi arcs on the top and bottom surfaces as well as the bulk chiral Landau level. Therefore, the spectrum of a slab of a WSM in a magnetic field contains a low energy fine quantization of levels, in the place of the single chiral mode as well as Landau levels of index $n > 1$ with bulk degeneracy.

5.3.1 Bulk Landau levels of a WSM

The bulk Landau levels can be obtained by considering the low energy Weyl Hamiltonian (5.1.1) in the case of our effective model. Here, $\mathbf{v} = 0$ and only the diagonal elements of h_{ij} are finite,

$$H = t_s k_x \sigma_x + t_s k_y \sigma_y + \chi v_z k_z \sigma_z, \tag{5.3.1}$$

where we defined $v_z = \sqrt{t_s^2 - m^2}$ and χ is the chirality of the node. We apply a magnetic in the y-direction via substituting the canonical momentum $\pi = \mathbf{k} + \mathbf{A}$ and choosing the

Landau gauge, $\mathbf{A} = -Bxe_z$. Defining harmonic oscillator operators this gives:

$$v_z\pi_z = -\frac{i\sqrt{v_z}}{\sqrt{2}\ell_B}(a^\dagger - a), \quad \pi_x = \frac{\sqrt{v_z}}{\sqrt{2}\ell_B}(a^\dagger + a). \tag{5.3.2}$$

The spectrum is found by squaring the Hamiltonian:

$$H^2 = \left(\frac{2v_z}{\ell_B^2}(a^\dagger a + \frac{1}{2}) + k_y^2\right)\sigma_0 - \chi\frac{v_z}{\ell_B^2}\sigma_y, \tag{5.3.3}$$

where the second term comes from the commutation relation. Clearly the eigenstates of H are eigenstates of σ_y. With the ansatz $\psi_0 = (|0\rangle, i\chi|0\rangle)^T$, the zeroth Landau level is easily found to have energy $E_0 = \chi k_y$. Thus, we end up with a single chiral Landau level, independent of the magnetic field. Higher Landau levels are given by

$$E_n = \pm\sqrt{\frac{2v_z}{\ell_B^2}n + k_y^2}. \tag{5.3.4}$$

Note that each Weyl node exhibits only one zeroth Landau level. As explained by the Nielsen-Ninomiya theorem[41, 42], Weyl nodes always come in pairs with opposite chiralities and in the full lattice model the chiral Landau levels are connected at high energy.

5.3.2 Surface quantum oscillations

Now we are in a place to analyze the Fermi arc induced quantum oscillations through the effective surface theory. Semi-classically, when applying a magnetic field perpendicular to the surface of a slab, the field will induce movement of the electrons along the Fermi arc perpendicular to the Fermi velocity and the magnetic field. Moving along the arc the electron ultimately reaches the Weyl node. Once reaching the node, the only accessible

state is the bulk chiral Landau. Using this level the electron tunnels to the opposite surface where it can again move on the arc. This motion leads to the other Weyl node and eventually the cycle is closed.

The above surface-bulk cycle leads to fine quantization of energy which is given in Eq. (5.1.2). This semiclassical approach assumes that the Weyl node separation is large compared to the inverse magnetic length, $\Delta k\, \ell_B \gg 1$, so that the Weyl nodes decouple.

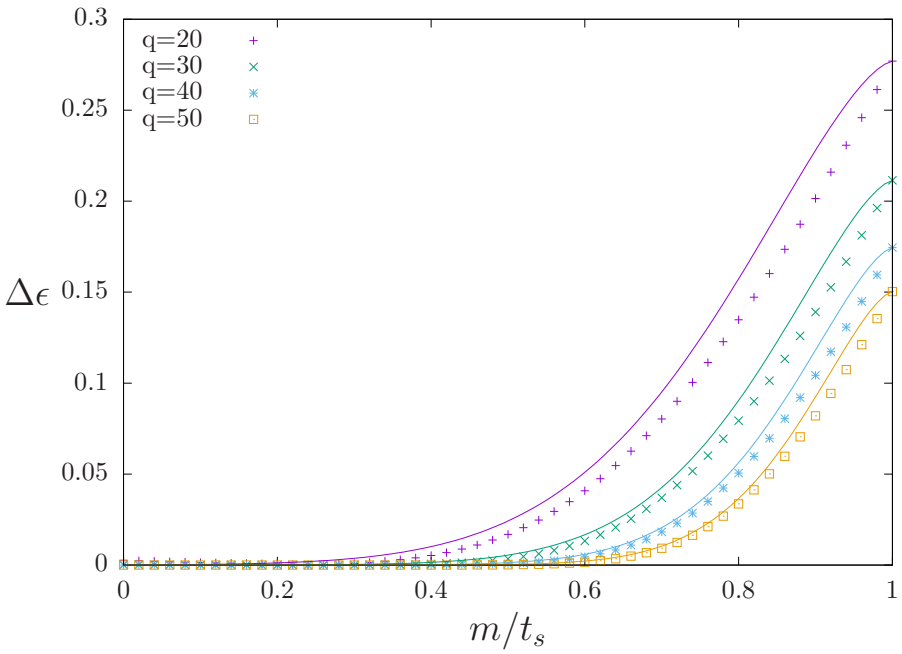

Figure 5.2: Zeroth bulk Landau level for varying m from numerics (data points) and WKB approximation (lines) for varying magnetic fields $B = \frac{2\pi}{q}$.

The effective surface theory enables us to go beyond this limit and analyze the system when the Weyl node distance is comparable to the inverse magnetic length, i.e., either small arc lengths or large magnetic fields. In this regime, one has to take into account the fact that there will be a non-zero probability for a state from one node to tunnel to the other and vice versa, leading to a finite energy for the lowest Landau level even at the

node. In the appendix we show that the energy offset is given by,

$$\Delta\epsilon = \sqrt{2}C(m^* v_F^2 \omega_c^2)^{\frac{1}{3}} \exp\left(-\frac{2}{3}\frac{\Delta k^3 m^* v_F^2}{\omega_c}\right), \tag{5.3.5}$$

where

$$C = \frac{1}{\sqrt{2}}\left(2\sqrt{\frac{\pi}{2}}\frac{\Gamma(\frac{7}{4})}{\Gamma(\frac{1}{4})}\right)^{\frac{2}{3}}. \tag{5.3.6}$$

The Fermi velocity v_F, the effective mass m^* for our model are defined in the appendix and ω_c is the cyclotron frequency. This offset fully derives from the bulk model and in Fig. 5.2 we compare the gap in Eq. (5.3.6) to the value of the zeroth Landau level at $k_y = 0$ for the full bulk lattice model. One can see that the construction overestimates the energy gap by a small amount. This is due to the fact that the WKB approximation used in the derivation works better for higher Landau levels and the fact that we ignored the linear term in the potential. Nonetheless, the approximation captures the behaviour of the full system well.

In Fig. 5.3 (a) we show the surface density of states (DOS) calculated using the effective Greens function Eq. (5.2.5) for varying arc lengths in the long arc length regime for a fixed magnetic field and fixed slab thickness. We repeat this analysis in Fig. 5.3b for varying slab thickness, given that the slab thickness is large enough such that the surface states cannot tunnel from one side to another, except in the vicinity of the nodes. In these cases we find that the observed oscillations the effective surface theory coincide well with the semiclassical theory in Eq. (5.1.2). In addition, one can read off the phase offset $\gamma = \frac{1}{2}$, which indicates that the Berry phase contributions of the two Weyl nodes cancel each other. This is consistent with the fact that the chiral Landau levels from both Weyl nodes (with opposite chiralities) are involved in forming the magnetic orbit.

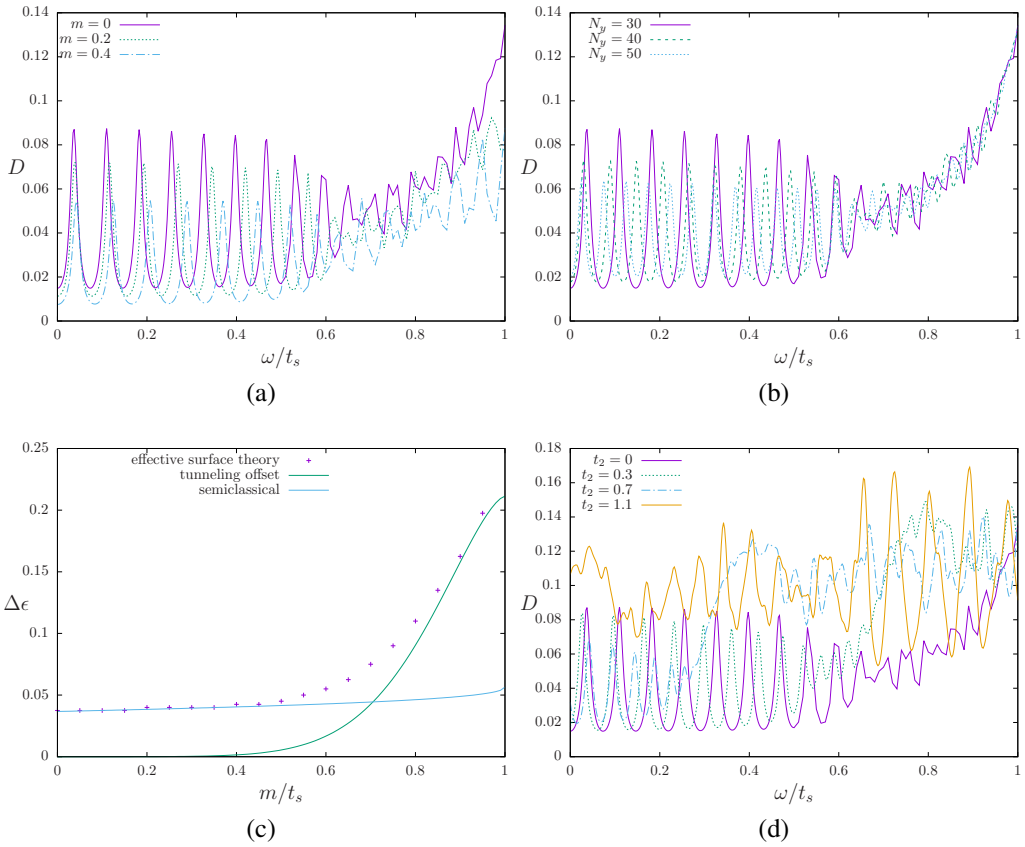

Figure 5.3: Surface density of states for (a) varying arc length at magnetic field with $q = 30$ and thickness $N_y = 30$, (b) varying slab thickness with $q = 30$ and $m = 0$. (c) Energy offset of the zeroth Landau level for varying arc lengths. (d) Surface density of states for $q = 30$, $N_y = 30$ and $m = 0$ for varying parameter t_2.

When moving from long arc lengths towards the small arc length regime, one would imagine a regime shift in the contributions to the phase offset. Indeed, when analyzing the energy offset in Fig. 5.3c one can see that for short arc lengths, the bulk energy gap from the approaching Weyl nodes is dominating and the contribution from the quantum oscillations is vanishing when approaching the point where the two Weyl nodes fuse at $m = t_s$.

Additionally, this phase offset is a direct signature of the fact that the Fermi arcs hybridize with the chiral bulk Landau levels to form magnetic orbitals. As was shown above,

the offset is acquired by the bulk Landau level due to the finite tunnelling probability and carries over directly to the surface quantum oscillations.

Another interesting regime is a type II Weyl semimetal. In this regime, due to the tilt term there is no chiral Landau level[17] while other bulk Landau levels are present. As suggested by the semiclassical analysis, the existence of surface Landau levels depend crucially on the bulk chiral Landau level. In its absence we do not expect to see surface level quantization.

To test whether the surface states are quantized in Landau levels in a type II WSM we add a term to the Hamiltonian:

$$H_2 = t_2 \sin(k_z), \tag{5.3.7}$$

which will turn the Weyl nodes into type-II Weyl nodes for $t_2 > t_s$. As mentioned above, in this regime the chiral Landau level is absent. This absence can be understood when analyzing the large t_2-limit. In this regime H_2 completely dominates and applying a magnetic field in a direction perpendicular to z will lead to a gapped spectrum. In Fig. 5.3 (d) we show the results for various values of t_2, where one can see that when increasing t_2 the low energy regime which is dominated by the Fermi arc quantum oscillations shrinks until it completely vanishes for $t_2 > t_s$. Our results therefore support the claim that the chiral Landau level is necessary for the formation of surface Landau levels.

5.4 Numerical Analysis

In order to test the predictions of our effective surface theory, we use exact numerical diagonalization of a lattice model with an applied magnetic field via Peierls substitution. As in previous sections, the magnetic field B is oriented in the y-direction and in Landau

gauge, the vector potential reads $\mathbf{A} = -Bx\mathbf{e_z}$. In this gauge the hopping along z acquires an x-dependent phase which breaks the translation invariance in the x-direction. We therefore define a magnetic unit cell, elongated along the x-direction. Choosing a cell of length q lattice constants through which a flux quantum Φ_0 is threaded amounts to a magnetic field $B = \Phi_0/qa^2$ where a is the lattice constant. We vary q to control the field strength. With this gauge the hopping along z acquires a phase of $\exp\left(-i\frac{2\pi n_x}{q}\right)$, where n_x is the index of the nth lattice site inside the magnetic unit cell. This increases the sizes of the matrices H_0 and R to $2q$-by-$2q$ and the y-layer Hamiltonian reads

$$\begin{aligned} H_0 = \sum_{k_x,k_z} \Bigg[& \sum_n (m + 2 + \sin(kz - 2\pi/q \cdot n))\sigma_z c_n^\dagger c_n + \sum_{\langle n,m\rangle} (\frac{i\sigma_x - \sigma_z}{2}) c_n^\dagger c_m \\ & -\frac{1}{2} e^{-ik_x} \sigma_z c_1^\dagger c_p + \frac{1}{2i} e^{-ik_x} \sigma_x c_1^\dagger c_p + \text{h.c.} \Bigg], \end{aligned} \tag{5.4.1}$$

where the indices n, m run from 1 to q and we have suppressed the k-indices. The coupling between different y-layers is given by

$$R = \left(-\frac{1}{2}\sigma_z + \frac{1}{2i}\sigma_y\right) \otimes 1_q, \tag{5.4.2}$$

where 1_q is a q-by-q unit matrix in the magnetic unit cell basis. The full $2qN_y$-by-$2qN_y$-Hamiltonian can be easily constructed. When diagonalizing the full system, we expect the low energy spectrum to be dominated by the Fermi arc quantum oscillations and bulk contributions at higher energies.

In Fig. 5.4 (a) we show the low energy spectrum (with respect to the parameter t_s) of a WSM slab in a magnetic field. At low energy (below $0.6t_s$ in our model) one can see the Fermi-arc Landau level structure. For higher energies, one can observe bulk Landau levels mixed with the surface Landau levels. This is shown explicitly by varying the slab thickness. The frequency of the Fermi arc induced quantum oscillations varies with slab

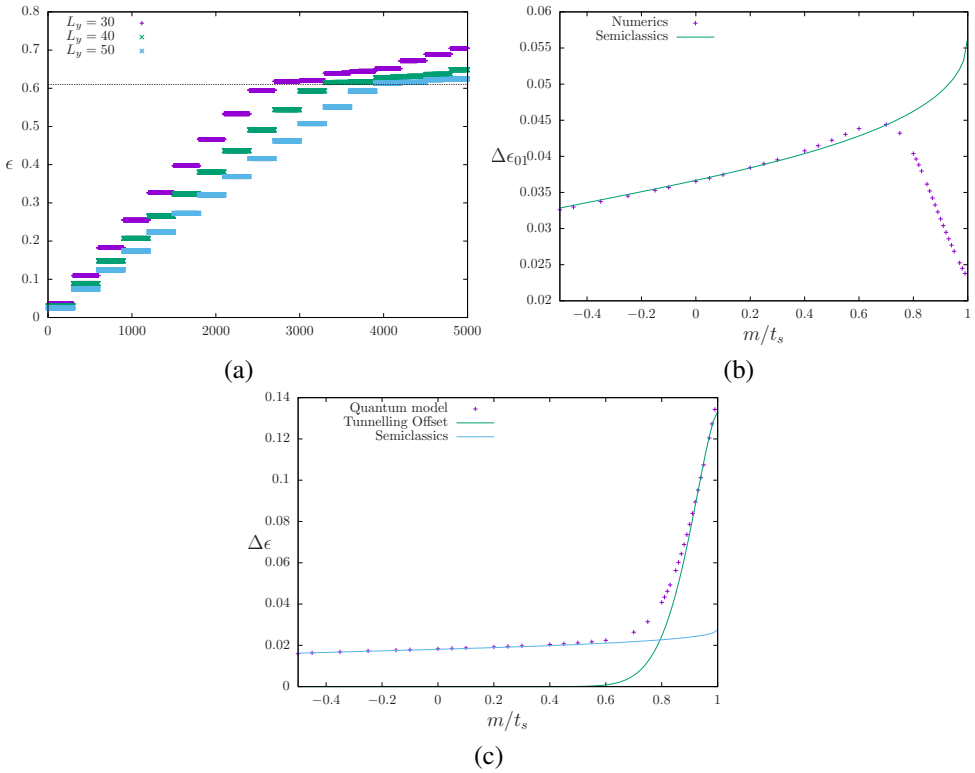

Figure 5.4: (a) Bulk spectrum for a slab with model parameters $q = 80$, $N_y = 40$ and $m = 0$. (b) Energy difference of the first and zeroth Landau level for $q = 60$ and $N_y = 60$. (c) Energy offset as a function of arc length for the same parameter values as in (b).

thickness, but the bulk Landau level spacing is almost constant.

Analyzing the frequency of the the Landau levels in energy space enables us to test the predictions of the semiclassical theory and in addition further investigate the behaviour of the slab in regimes not accessible by the semiclassical theory. This is done in Fig. 5.4(b) where we confirm that the semiclassical approach accurately describes the frequency of the quantum oscillations when varying the slab width. Further, in Fig. 5.4(c) we vary the arc length k_a of the Fermi arcs in the surface Brillouin zone and compare the energy difference of the first and zeroth Landau level with the semiclassical theory Eq. (5.1.2). One can see that only for long arc lengths does the semiclassical theory describe the full quantum model well. This was done by taking into account the diabatic correction[36] to the arc length $\propto \ell_b^{-1}$ which is due to the fact that an electron on the arc can tunnel through the bulk even before reaching a Weyl point. For small arc lengths the behaviour significantly diverges from the semiclassical theory and converges towards the behaviour for the merged Weyl points derived in appendix 5.A.

Further, we can analyze the phase offset through the full bulk system and compare it to the findings from using the effective surface theory. In Fig. 5.4c we show a comparison of the energy offset in the full bulk system with the semiclassical expectation with $\gamma = \frac{1}{2}$ as well as the tunnelling gap. One can see the expected crossover behaviour from the offset governed by the surface contribution to the bulk behaviour for $m \to t_s$.

5.5 Conclusion

In this work we have analyzed the explicit surface character of quantum oscillations in Weyl semimetals involving the surface Fermi arcs. We found clear signatures of the quantum oscillations in the surface density of states and have analyzed contributions to the phase offset. We identified an additional contribution to the phase offset due to the

proximity of the two Weyl nodes and showed that there is no contribution from the Berry curvature. In addition, we have presented direct evidence that the semiclassical picture is accurate when the Weyl nodes are well separated.

5.6 Acknowledgements

Financial support for this work has been provided by the Alexander McFee award (JB), NSERC and FQRNT (JB and TPB).

5.A Bulk Landau levels for overlapping Weyl nodes

For large Weyl node separations, one can model each Weyl node separately and arrive at the usual Weyl Landau levels. However, when the two Weyl nodes approach each other, they can not be treated separately. As a result chiral Landau level becomes massive (gapped).

In order to address this we consider a bulk model with an applied magnetic field in y-direction, $\vec{B} = B\vec{e}_y$ and vector potential $\vec{A} = Bz\vec{e}_x$. As discussed in the first section, the system experiences a gap closure at $m = t_s$. Lowering m further, the gap closure splits into two Weyl nodes which traverse the Brillouin zone and recombine for $m = -t_s$. The point of the gap closure for $m = t_s$ is $\vec{k}_0 = (0, 0, -\pi/2)^T$. Around this point one can expand the Hamiltonian as

$$H = v_F k_x \sigma_x + v_F k_y \sigma_y + (\gamma + \frac{k_z^2}{2m^*})\sigma_z, \tag{5.A.1}$$

where $\gamma = m - t_s$ and we have omitted the quadratic terms in k_x and k_y. We defined the Fermi velocity $v_F = ta$ and $m^* = \frac{1}{a^2 t_s}$, where we explicitly wrote out the lattice constant

a. Adding the magnetic field to the system, we arrive at

$$H = Bv_F\tilde{z}\sigma_x + v_F k_y \sigma_y + (\gamma + \frac{k_z^2}{2m^*})\sigma_z, \tag{5.A.2}$$

where we have defined $\tilde{z} = z + k_x/B$. Normally one arrives at a zeroth Landau level which depends on the momentum along the field direction, in this case k_y, and is gapless for $k_y = 0$. Here, however, the zeroth Landau level acquires a mass which is estimated below.

Defining the new variables $Z = \frac{\tilde{z}}{\alpha}$ and $K = \alpha k_z$ with $\alpha = (v_F m^* B)^{-\frac{1}{3}}$, we arrive at

$$H = (m^* v_F^2 \omega_c^2)^{\frac{1}{3}} \left(Z\sigma_x + (\Gamma + \frac{K^2}{2})\sigma_z \right), \tag{5.A.3}$$

with the now dimensionless $\Gamma = \frac{\gamma}{(m^* v_F^2 \omega_c^2)^{\frac{1}{3}}}$ and the cyclotron frequency $\omega_c = \frac{B}{m^*}$. Squaring the Hamiltonian leads to

$$\begin{aligned} H^2 =& (m^* v_F^2 \omega_c^2)^{\frac{2}{3}} \begin{pmatrix} Z^2 + (\Gamma + \frac{K^2}{2})^2 & -\frac{1}{2}[Z, K^2] \\ \frac{1}{2}[Z, K^2] & Z^2 + (\Gamma + \frac{K^2}{2})^2 \end{pmatrix} \\ =& (m^* v_F^2 \omega_c^2)^{\frac{2}{3}} \left[\left(Z^2 + (\Gamma + \frac{K^2}{2})^2 \right) \sigma_0 + K\sigma_y \right], \end{aligned} \tag{5.A.4}$$

where we have used $[Z, K^2] = 2iK$. Ignoring the prefactor for now, one gets the eigenvalue equation,

$$\begin{aligned} \left(Z^2 + (\Gamma + \frac{K^2}{2})^2 \right) c_1 - iKc_2 &= E^2 c_1, \\ iKc_1 + \left(Z^2 + (\Gamma + \frac{K^2}{2})^2 \right) c_2 &= E^2 c_2. \end{aligned} \tag{5.A.5}$$

Using the ansatz $c_2 = ic_1$, we get

$$\left(Z^2 + (\Gamma + \frac{K^2}{2})^2 + K\right) c_{1,2} = E^2 c_{1,2}. \tag{5.A.6}$$

This has the general structure of the differential equation for an anharmonic oscillator when the operators are written in the *momentum space* basis as opposed to the real space basis. Using this analogy, we can solve this by defining the 'potential' in momentum space, $V \equiv V(K) = (\Gamma + \frac{K^2}{2})^2 + K$. In order to analyze the equation, we approximate it by ignoring the linear term. We want to investigate the $m = t_s$ limit, i.e., $\Gamma = 0$. In this case the two Weyl nodes are combined to one single gap closure and one can solve the problem via the WKB approximation. The quantization condition reads,

$$\int_{x_-}^{x_+} \sqrt{E^2 - V} = \left(n + \frac{1}{2}\right)\pi, \tag{5.A.7}$$

where $x_\pm = \pm\sqrt{2}E^{\frac{1}{2}}$ are the turning points. The left hand side can be transformed,

$$E\int_{x_-}^{x_+} dK \sqrt{1 - \left(\frac{K}{x}\right)^4} = \frac{\sqrt{2}E^{\frac{3}{2}}}{2}\int_0^1 \frac{dt}{t^{\frac{3}{4}}}\sqrt{1-t}, \tag{5.A.8}$$

with $t = \left(\frac{K}{x}\right)^4$. The integral is defined as the Euler beta function,

$$\mathcal{B}(x,y) = \int_0^1 dt\; t^{x-1}\,(1-t)^{y-1}\,, \tag{5.A.9}$$

at $x = \frac{1}{4}$ and $y = \frac{3}{2}$ and therefore,

$$\pi\left(n + \frac{1}{2}\right) = \frac{\sqrt{2}E^{\frac{3}{2}}}{2}\mathcal{B}\left(\frac{1}{4}, \frac{3}{2}\right). \tag{5.A.10}$$

With $\mathcal{B}\left(\frac{1}{4},\frac{3}{2}\right) = \frac{\sqrt{\pi}\Gamma(\frac{1}{4})}{2\Gamma(\frac{7}{4})}$ we get

$$E_n = \left(4\sqrt{\frac{\pi}{2}}\frac{\Gamma(\frac{7}{4})}{\Gamma(\frac{1}{4})}(n+\frac{1}{2})\right)^{\frac{2}{3}}, \tag{5.A.11}$$

and reinstating the prefactor leads to

$$E_n = (m^* v_F^2 \omega_c^2)^{\frac{1}{3}} \left(4\sqrt{\frac{\pi}{2}}\frac{\Gamma(\frac{7}{4})}{\Gamma(\frac{1}{4})}(n+\frac{1}{2})\right)^{\frac{2}{3}}. \tag{5.A.12}$$

As usual, the WKB approximation works better for higher Landau levels and we have ignored the linear term. When comparing to the numerically calculated Landau levels of the full system, only the first couple of Landau levels acquire a correction $\zeta(n)$. We find numerically that the zeroth Landau level gets a factor of $\zeta(0) \approx 0.811$ and already for $n \geq 1$ we find $\zeta(n) \approx 1$, which is very close to what the authors in [43] have found.

5.B Chiral Landau level for small Weyl node separation

In order to estimate the energy shift of the chiral Landau level as a function of the Weyl node separation, we will start from equation (5.A.4), from which one can read off the potential in momentum space as $V(K) = (\Gamma + \frac{K^2}{2})^2 + K$. This is the potential of an anharmonic oscillator in momentum space and for $\Gamma < 0$ we have two distinct minima. Ignoring the linear term, we have a symmetric double well problem[44], where $\Gamma = \frac{m - t_s}{(m^* v_F^2 \omega_c^2)^{\frac{1}{3}}}$ controls the separation of the two wells. We approach the problem by restricting our Hilbert space to that spanned by two wavefunctions, ψ_r and ψ_l. These are the ground states of the left and right wells located at $\pm\sqrt{2\Gamma}$, when they are completely separated form each other. When the two wells approach each other, the two

wavefunctions hybridize due to the finite tunnelling probability. The new eigenstates are the symmetric and anti-symmetric combinations,

$$\psi_{\pm}(K) = \frac{1}{\sqrt{2}} \left(\psi_r(K) \pm \psi_r(-K) \right). \tag{5.B.1}$$

The wavefunctions obey the Schrödinger equations,

$$\begin{aligned} \psi_r^{''} + (V - E_r)\psi_r = 0, \\ \psi_{\pm}^{''} + (V - E_{\pm})\psi_{\pm} = 0 \end{aligned} \tag{5.B.2}$$

where the first equation is valid due to the fact that the double well potential equals the single well potential in the regime of ψ_r. In addition, the amplitude of ψ_r in the left well is vanishingly small. Without loss of generality, we pick ψ_+. Multiplying the first equation by ψ_+ and the second one by ψ_r, subtracting the first equation from the second and subsequently integrating from 0 to ∞ and using integration by parts, one arrives at,

$$\Delta E = 2\psi_r(0)\psi_r^{'}(0). \tag{5.B.3}$$

Restoring the prefactor from (5.A.4) and taking into account that we squared the Hamiltonian in order to derive Eq. (5.A.4), via $\Delta\epsilon = (m^* v_s^2 \omega_c^2)^{\frac{1}{3}} \sqrt{\Delta E}$ we arrive at,

$$\Delta\epsilon = \sqrt{2}(m^* v_F^2 \omega_c^2)^{\frac{1}{3}} \left(\psi_r(0)\psi_r^{'}(0) \right)^{\frac{1}{2}}. \tag{5.B.4}$$

In order to evaluate this expression, we use the WKB approximation and we have,

$$\psi_r(0) = \frac{C}{V^{\frac{1}{4}}} \exp\left(- \int_0^{\sqrt{2\Gamma}} |\sqrt{V}| \right), \quad \psi_r^{'}(0) = \sqrt{V}\psi_r(0) \tag{5.B.5}$$

Evaluating the integral we arrive at,

$$\Delta\epsilon = \sqrt{2}(m^* v_F^2 \omega_c^2)^{\frac{1}{3}} C \exp\left(-|\Gamma|^{\frac{3}{2}}\left(\sqrt{2} + \frac{2^{\frac{3}{2}}}{6}\right)\right) \tag{5.B.6}$$

The distance of the Weyl node from the middle point around which we have expanded the Hamiltonian, is given by $\Delta k = \arccos(m/t_s) \approx \sqrt{2\frac{(t_s-m)}{t_s}}$, where we have expanded around $m = 1$. With this, we arrive at the final result,

$$\Delta\epsilon = \sqrt{2}(m^* v_F^2 \omega_c^2)^{\frac{1}{3}} C \exp\left(-\frac{2}{3}\frac{\Delta k^3 m^* v_F^2}{\omega_c}\right). \tag{5.B.7}$$

The constant C can be inferred from the lowest Landau level at $m = t_s$ (see Appendix 5.A) and we get

$$C = \frac{1}{\sqrt{2}}\left(2\sqrt{\frac{\pi}{2}}\frac{\Gamma(\frac{7}{4})}{\Gamma(\frac{1}{4})}\right)^{\frac{2}{3}}. \tag{5.B.8}$$

References

[1]S. Murakami, New Journal of Physics **9**, 356 (2007).

[2]A. A. Burkov, M. D. Hook, and L. Balents, Phys. Rev. B **84**, 235126 (2011).

[3]X. Wan, A. M. Turner, A. Vishwanath, and S. Y. Savrasov, Phys. Rev. B **83**, 205101 (2011).

[4]A. A. Burkov and L. Balents, Phys. Rev. Lett. **107**, 127205 (2011).

[5]W. Witczak-Krempa and Y. B. Kim, Phys. Rev. B **85**, 045124 (2012).

[6]G. Chen and M. Hermele, Phys. Rev. B **86**, 235129 (2012).

[7]T. T. Heikkilä, N. B. Kopnin, and G. E. Volovik, JETP Letters **94**, 233–239 (2011).

[8]H. Weng, C. Fang, Z. Fang, B. A. Bernevig, and X. Dai, Phys. Rev. X **5**, 011029 (2015).

[9]S.-M. Huang, S.-Y. Xu, I. Belopolski, C.-C. Lee, G. Chang, B. Wang, N. Alidoust, G. Bian, M. Neupane, C. Zhang, S. Jia, A. Bansil, H. Lin, and M. Z. Hasan, Nat Commun **6** (2015).

[10]B. Q. Lv, H. M. Weng, B. B. Fu, X. P. Wang, H. Miao, J. Ma, P. Richard, X. C. Huang, L. X. Zhao, G. F. Chen, Z. Fang, X. Dai, T. Qian, and H. Ding, Phys. Rev. X **5**, 031013 (2015).

[11]B. Q. Lv, N. Xu, H. M. Weng, J. Z. Ma, P. Richard, X. C. Huang, L. X. Zhao, G. F. Chen, C. E. Matt, F. Bisti, V. N. Strocov, J. Mesot, Z. Fang, X. Dai, T. Qian, M. Shi, and H. Ding, Nat Phys **11**, 724–727 (2015).

[12]L. X. Yang, Z. K. Liu, Y. Sun, H. Peng, H. F. Yang, T. Zhang, B. Zhou, Y. Zhang, Y. F. Guo, M. Rahn, D. Prabhakaran, Z. Hussain, S. .-.-K. Mo, C. Felser, B. Yan, and Y. L. Chen, Nat Phys **11**, 728–732 (2015).

[13]I. Belopolski, S.-Y. Xu, D. S. Sanchez, G. Chang, C. Guo, M. Neupane, H. Zheng, C.-C. Lee, S.-M. Huang, G. Bian, N. Alidoust, T.-R. Chang, B. Wang, X. Zhang, A. Bansil, H.-T. Jeng, H. Lin, S. Jia, and M. Z. Hasan, Phys. Rev. Lett. **116**, 066802 (2016).

[14]S.-Y. Xu, N. Alidoust, I. Belopolski, Z. Yuan, G. Bian, T.-R. Chang, H. Zheng, V. N. Strocov, D. S. Sanchez, G. Chang, C. Zhang, D. Mou, Y. Wu, L. Huang, C.-C. Lee, S.-M. Huang, B. Wang, A. Bansil, H.-T. Jeng, T. Neupert, A. Kaminski, H. Lin, S. Jia, and M. Zahid Hasan, Nat Phys **11**, 748–754 (2015).

[15]C.-X. Liu, P. Ye, and X.-L. Qi, Phys. Rev. B **87**, 235306 (2013).

[16]S.-Y. Xu, I. Belopolski, D. S. Sanchez, C. Zhang, G. Chang, C. Guo, G. Bian, Z. Yuan, H. Lu, T.-R. Chang, P. P. Shibayev, M. L. Prokopovych, N. Alidoust, H. Zheng, C.-C. Lee, S.-M. Huang, R. Sankar, F. Chou, C.-H. Hsu, H.-T. Jeng, A. Bansil, T. Neupert, V. N. Strocov, H. Lin, S. Jia, and M. Z. Hasan, Science Advances **1** (2015) 10.1126/sciadv.1501092.

[17]A. A. Soluyanov, D. Gresch, Z. Wang, Q. Wu, M. Troyer, X. Dai, and B. A. Bernevig, Nature **527**, 495–498 (2015).

[18]Y. Sun, S.-C. Wu, M. N. Ali, C. Felser, and B. Yan, Phys. Rev. B **92**, 161107 (2015).

[19]Z. Wang, D. Gresch, A. A. Soluyanov, W. Xie, S. Kushwaha, X. Dai, M. Troyer, R. J. Cava, and B. A. Bernevig, 2015.

[20]S.-M. Huang, S.-Y. Xu, I. Belopolski, C.-C. Lee, G. Chang, T.-R. Chang, B. Wang, N. Alidoust, G. Bian, M. Neupane, D. Sanchez, H. Zheng, H.-T. Jeng, A. Bansil, T. Neupert, H. Lin, and M. Z. Hasan, Proceedings of the National Academy of Sciences **113**, 1180–1185 (2016).

[21]G. Xu, H. Weng, Z. Wang, X. Dai, and Z. Fang, Phys. Rev. Lett. **107**, 186806 (2011).

[22]K. Koepernik, D. Kasinathan, D. Efremov, S. Khim, S. Borisenko, B. Büchner, and J. van den Brink, 2016.

[23]T.-R. Chang, S.-Y. Xu, G. Chang, C.-C. Lee, S.-M. Huang, B. Wang, G. Bian, H. Zheng, D. S. Sanchez, I. Belopolski, N. Alidoust, M. Neupane, A. Bansil, H.-T. Jeng, H. Lin, and M. Zahid Hasan, Nat Commun **7** (2016).

[24]H. Nielsen and M. Ninomiya, Physics Letters B **130**, 389–396 (1983).

[25]S. L. Adler, Phys. Rev. **177**, 2426–2438 (1969).

[26]J. S. Bell and R. Jackiw, Il Nuovo Cimento A (1971-1996) **60**, 47–61 (1969).

[27]P. Hosur and X. Qi, Comptes Rendus Physique **14**, Topological insulators / Isolants topologiquesTopological insulators / Isolants topologiques, 857–870 (2013).

[28]K.-Y. Yang, Y.-M. Lu, and Y. Ran, Phys. Rev. B **84**, 075129 (2011).

[29]A. A. Zyuzin and A. A. Burkov, Phys. Rev. B **86**, 115133 (2012).

[30]O. Vafek and A. Vishwanath, Annual Review of Condensed Matter Physics **5**, 83–112 (2014).

[31]P. Goswami and S. Tewari, Phys. Rev. B **88**, 245107 (2013).

[32]Y. Chen, S. Wu, and A. A. Burkov, Phys. Rev. B **88**, 125105 (2013).

[33]Z. Jian-Hui, J. Hua, N. Qian, and S. Jun-Ren, Chinese Physics Letters **30**, 027101 (2013).

[34]M. M. Vazifeh and M. Franz, Phys. Rev. Lett. **111**, 027201 (2013).

[35]S.-Y. Xu, I. Belopolski, N. Alidoust, M. Neupane, G. Bian, C. Zhang, R. Sankar, G. Chang, Z. Yuan, C.-C. Lee, S.-M. Huang, H. Zheng, J. Ma, D. S. Sanchez, B. Wang, A. Bansil, F. Chou, P. P. Shibayev, H. Lin, S. Jia, and M. Z. Hasan, Science **349**, 613–617 (2015).

[36]A. C. Potter, I. Kimchi, and A. Vishwanath, Nat Commun **5** (2014).

[37]Y. Zhang, D. Bulmash, P. Hosur, A. C. Potter, and A. Vishwanath, Dec. 2015.

[38]P. J. Moll, N. L. Nair, T. Helm, A. C. Potter, I. Kimchi, A. Vishwanath, and J. G. Analytis, May 2015.

[39]M.-C. Chang and M.-F. Yang, Phys. Rev. B **91**, 115203 (2015).

[40]D. J. J. Marchand and M. Franz, Phys. Rev. B **86**, 155146 (2012).

[41]H. Nielsen and M. Ninomiya, Physics Letters B **105**, 219–223 (1981).

[42]D. Friedan, Communications in Mathematical Physics **85**, 481–490 (1982).

[43]P. Dietl, F. Piéchon, and G. Montambaux, Phys. Rev. Lett. **100**, 236405 (2008).

[44]L. Landau and L. Lifshitz (Butterworth-Heinemann, 1965).

6

Conclusions

6.1 Summary of the thesis

This thesis has dealt with the topological properties of gapped as well as gapless topological states. It was investigated how entanglement and topology interact in symmetry protected topological states and how perturbations influence the topological state. To this end, we looked at disorder in topological superconductors as well as an external magnetic field in a Weyl semimetal.

We started out in the second chapter and analyzed numerically the entanglement entropy of a spin-orbit coupled superconductor with either s-wave or d-wave pairing. In symmetry protected topological states the topological entanglement entropy is zero, but nonetheless there remains a signature of the topological phase transition in the entanglement entropy. We analyzed some of the different possible partitions of the system and found that the subleading contributions are mainly governed by corner contributions. In addition, the analysis showed the fact that the topological entanglement entropy is in fact zero.

In the third chapter we complemented the numerical analysis with an analytical

calculation of the topological superconductor with s-wave pairing in the large Zeeman coupling limit. We explicitly review the derivation of the projection to a single band, spinless superconductor with effective $p_x + ip_y$-wave pairing and use the simpler structure of the system to derive an analytic expression of the entanglement entropy. We were able to explicitly show that the entanglement entropy obeys the area law and shows a signature of the topological phase transition.

Based on these results, in chapter four, we were subsequently able to investigate the topological superconductor when subjected to a random disorder potential. Using a real space Chern number construction we were able to investigate the topological phase transition for varying disorder strengths and to detect a new topological phase that was not present in the clean system. This result was then confirmed by using a Gaussian disorder potential in connection with perturbation theory. In addition, we were able to investigate the disorder-averaged entanglement entropy and compare its behaviour to the other two methods.

In the last chapter we subsequently moved on to gapless topological phases and subjected a Weyl semimetal to an external magnetic field. In this system we then specifically investigated the surface of the Weyl semimetal in a slab geometry via an effective surface theory. When exposed to a magnetic field we found that the surface density of states experiences a clear Landau level structure stemming from magnetic orbits formed by the surface Fermi arcs, special to Weyl semimetals. These orbits inherit a characteristic dependency of the thickness of the slab that we were able to confirm using the effective surface propagator.

6.2 Future Directions

There are several possible extensions of the work contained in this thesis and we want to discuss some of them in this section.

A straight forward generalization of the work on the entanglement entropy would be to extend it to different symmetry protected topological states in different symmetry classes and dimensions in order to further investigate its behaviour around topological phase transitions. Further, it might be interesting to investigate the critical properties of the entanglement entropy in the vicinity of the phase transition point. However, this already involves considerable computational effort even without considering self consistency.

In addition, the analysis of the disordered topological superconductor from chapter four could be extended as well. Specifically, the perturbation approach using a Gaussian disorder potential could be extended to include crossed diagrams. These diagrams should lead to contributions to the renormalization of the parameters of the Hamiltonian that could explain the observed discrepancy between the real space Chern number approach and the perturbation theory.